Doctoral Dissertation (Censored)

博士論文（要約）

Mineralogical and geochemical study of quenched angrite meteorites: Implication for crystallization process and shock history of ancient igneous rocks in the solar system
（急冷したアングライト隕石の鉱物学的・宇宙化学的研究：太陽系最初期の火成岩の結晶化過程及び衝撃進化の解明）

A Dissertation Submitted for the Degree of Doctor of Philosophy
December 2021

令和 3 年 12 月博士（理学）申請

Department of Earth and Planetary Science, Graduate School of Science,
The University of Tokyo

東京大学大学院理学系研究科地球惑星科学専攻

Hideyuki Hayashi

林　秀幸

Abstract

Angrites are basaltic achondrites that are depleted in volatile elements and enriched in refractory elements. Most angrites show either quenched or slowly-cooled textures, with quenched angrites having older crystallization ages compared with the slowly-cooled angrites. Quenched angrites often contain Mg-rich olivine xenocrysts with homogeneous cores with variety of Fo#, Ca and Cr contents. However, the origin of olivine xenocrysts is still unclear as well as the formation process of igneous body of quenched angrites. In this study, I performed mineralogical and geochemical study of quenched angrites in order to clarify the crystallization process and shock history of the angrite parent body (APB).

Northwest Africa (NWA) 7203 is a quenched angrite, showing mineralogical features typically not present in other quenched angrites. NWA 7203 exhibits textures whose grain size varies from <10 μm to ~3 mm, while other quenched angrites show only single textures. Mg-rich olivines (~Fo_{64}) were found only in fine-grained lithologies. I propose that crystallization of NWA 7203 started in the fine-grained lithologies with Mg-rich olivine grains acting as seeds for crystallization. Coarse-grained lithologies were subsequently formed under conditions of slower cooling.

Quenched angrites except a possible cumulate sample (NWA 8535) exhibit three kinds of textures: dendritic, relatively coarse-grained, and anorthite spinifex. Dendritic samples are NWA 1296 and NWA 7203, and they contain dendrites consisting of olivine and anorthite. Relatively coarse-grained samples are Sahara 99555, D'Orbigny and Asuka-881371. Anorthite spinifex samples are NWA 1670, Lewis Cliff (LEW) 87051 and NWA 12774, and they contain extremely elongated anorthites. These textural varieties are considered to be caused by the difference of cooling rates. I estimated cooling rates from atomic diffusion recorded in olivine xenocryst (or early phenocryst) with chemically homogeneous core. The cooling rates are estimated as >300 ^{o}C/hr for fine-grained lithology of NWA 7203, 100 ^{o}C/hr for D'Orbigny, 50 ^{o}C/hr for Asuka-881371, 3 ^{o}C/hr for NWA

1670 and 3.5 ^{o}C/hr for NWA 12774, respectively, corresponding to textural varieties.

Bulk chemical compositions of quenched angrites show strong correlations for some elements as pointed out by Mikouchi et al. (2004), and the trends can be explained by incorporation of variable amounts of Mg-rich olivine xenocrysts into the common parent melt of quenched angrites. The incorporated degrees of olivine xenocrysts are estimated as about 0 % for NWA 1296, Sahara 99555, NWA 7203 and D'Orbigny (considered as 'pristine angrite magma'), 20 % for Asuka-881371 and NWA 1670, and 40 % for LEW 87051 and NWA 12774. REE patterns of quenched angrites also support mixing of 'pristine angrite magma' and olivine xenocrysts.

Modal abundances of olivine xenocrysts are estimated 0% for Sahara 99555 and NWA 7203, ~0% for D'Orbigny, 14% for Asuka-881371, ~11% for NWA 1670 and 13% for NWA 12774. From EPMA analyses, Fo# of the most Mg-rich olivine phenocrysts are Fo_{64} for NWA 1296, NWA 7203 and D'Orbigny, Fo_{65} for Sahara 99555, Fo_{72} for Asuka-881371, Fo_{80} for LEW 87051, Fo_{84} for NWA 12774, and Fo_{85} for NWA 1670, respectively. From the bulk chemical compositions, modal abundance of olivine xenocrysts and the most Mg-rich olivine phenocrysts of quenched angrites, I conclude that olivine xenocrysts are dissolved into 'pristine angrite magma', which made the melt composition more Mg-rich, but some of olivine xenocrysts remain unmelted.

To clarify the origin of olivine xenocrysts, I measured both oxygen isotopic ratios of olivine xenocrysts and phenocrysts in NWA 12774. The oxygen isotopic ratios of olivine xenocrysts and phenocrysts in NWA 12774 are identical to AFL, meaning that the olivine xenocrysts in NWA 12774 crystallized in APB, not in other asteroidal sources.

I suggest that quenched angrites came from a single igneous body where bulk chemical compositions and cooling rates change depending on burial depth because textures, cooling rates and bulk chemical compositions of quenched angrites are correlated with each other. I propose the formation process of the igneous body of quenched angrites as follows. (a) The parent melt was

produced by the partial melting of the quenched angrite source mantle and trapped mantle olivine grains as xenocrysts during its ascent. (b) The magma flow containing the Mg-rich olivine xenocrysts was erupted onto the surface of APB. (c) Rapid cooling of the lava flow and sinking and melting of the olivine xenocrysts started. (d) Subsequent lava flow came and overlay on NWA 7203 during crystallization. (e) Cooling rates were faster near the surface and slower at a lower part, producing the angrite textural varieties.

The stratigraphy of the igneous body of quenched angrites suggested in this study is similar to that of terrestrial komatiites. When I compared the uppermost layer of each igneous body (chilled margins), QA1 and A1, the finest grain size in each igneous body and fastest cooling rates are similar. The second shallowest layers, QA2 and A2, are similar in terms of the random mineral orientation and cooling rates. The third shallowest layers, QA3 and A3, contain oriented minerals and show similar cooling rates. On the other hand, mineral sizes of spinifex textures are different. The bottom layers, QB and B, are peridotite with a cumulate texture. Although bulk chemical compositions, mineral combinations and several characteristics are different between quenched angrites and komatiites, textural variations, and cooling rates of quenched angrites are comparable to komatiites.

Geological settings of komatiites are considered as continuous eruption from fissure (Hill et al., 1995). The formation process of quenched angrites might be similar to that of komatiites, and if so, a similar eruption event might have occurred at the surface of APB. Taking NWA 7203 into consideration, quenched angrites known until now might originate from an igneous body far from the eruption site because of its textural difference produced by cooling rate change when a subsequent lava flow overlay the earlier surface.

Index

1. Introduction

1.1. Evolutional history and differentiation of planetesimals in the early solar system

In the early solar system, condensation of gas and dust occurred in the protoplanetary disk. Small particles grew through sticky collisions during the accretion process in the first few million years of the solar system (e.g., Goldreich and Ward, 1973). When a body reaches a sufficient mass, it attracted other bodies due to gravity, and grew into a planetesimal. It is thought that planetesimals grew into protoplanets through repeated collisions. Petit and Morbidelli (2001) considered from *N*-body integrations that due to gravitational perturbations from Jupiter and planetesimals, most of the asteroids are ejected from the system in ~1 Myr, but a few asteroids survive, mostly in the region 2.8–3.3 AU, corresponding to the main asteroidal belt between the orbits of Mars and Jupiter. Therefore, it is believed that planetesimals that have not been fully developed into planets are left in the main belt, and the asteroids in the main belt retain information about the early solar system.

Planetesimal which had experienced igneous activity underwent core-mantle segregation and subsequent crust formation. Kruijer et al. (2014) discussed that core formation occurred over an interval of ~1 Myr considering from the ^{182}Hf-^{182}W chronometry for iron meteorites. The decay of radioactive ^{26}Al is the main energy source promoting asteroidal melting and differentiation for planetesimals in the early solar system (Larsen et al., 2016).

Crustal evolution of planetesimals is supported from Fe/Mg ratios of meteorites. Fe/Mg ratios for meteorites including differentiated bodies range from less than 0.08 to greater than 25 (Nittler et al. 2004), where carbonaceous chondrites are 1.92 ± 0.08 (Palme and Jones, 2003) and the solar photosphere is 1.87 ± 0.4 (Lodders, 2003). One of the reasons for these compositional scattering of meteorites is considered to be caused by collisional erosion of differentiated crust (O'Neill and Palme, 2008). This is supported by *N*-body simulations of terrestrial planet formation under the Grand Tack model (Walsh et al., 2011) reported by Carter et al. (2015).

As above, although there are many aspects to consider formation history of planetesimals, important processes in the protoplanet evolution of the early solar system are collisional evolution and internal differentiation. Therefore, analyzing differentiated meteorites is the best tool in order to understand these differentiation processes and shock history occurred on planetesimals in the early solar system. In the next paragraph, I will briefly introduce differentiated meteorites known until now.

1.2. Differentiated meteorites

Differentiated meteorites which retain information about crystallization process and shock history in the early solar system are mostly derived from the main belt asteroids between the orbits of Mars and Jupiter (e.g., Wetherill and Williams, 1979). Shock history is recorded as shock textures, and crystallization process is recorded as igneous textures of the meteorites. Crystallization ages, proportion of shocked samples and the estimated size of parent body of major achondrite groups derived from crust or mantle of planetesimals, are summarized in Table 1. Mars and the Moon are also included for comparison. Isotopic ages have a wide range because of difference of the timing of crystallization, or shock metamorphic disturbance. Here I chose the oldest crystallization ages to discuss the formation timing of differentiated crusts. Crystallization ages of angrites are older in quenched angrites (~4564 Ma) relative to slowly-cooled angrites (~4558 Ma), and the oldest Pb-Pb age was obtained from D'Orbigny (4564.64 ± 0.27 Ma, Amelin, 2008a). Aubrite, ureilite and HED meteorites often show shock metamorphic textures, and I chose crystallization ages of non shock metamorphic meteorites of these groups although such samples are rare. The crystallization age of aubrite is 4562.3 ± 0.4 Ma for Shallowater (I-Xe age anchored by several meteorites, Gilmour et al., 2009), which is the only aubrite without shock metamorphism. The crystallization age of ureilite is 4563 ± 21 Ma for Meteorite Hills (MET) 78008 (Pb-Pb age, Torigoye-Kita et al., 1995). The Hf-W ages of eucrite is 4563.8 ± 3.8 Ma for Asuka-881388 zircon (considered to indicate the crystallization age, Srinivasan et al., 2007). Samples from Mars and the Moon have wide ranges of crystallization ages because of prolonged igneous activity. The oldest Martian curst is found in Northwest Africa (NWA) 7034 Martian brecciated meteorite whose crystallization age is 4439 ± 17 Ma (U-Pb age of zircon, Yin et al., 2014). The crystallization timing of lunar magma ocean (LMO) is considered as 4417 ± 6 Ma from zircon in Apollo 17 clast-rich impact melt breccia 72215 (Nemchin et al., 2009).

Parent asteroids of angrite, aubrite, ureilite, and other differentiated meteorites are not well identified, but there are several studies discussing the sizes of these parent bodies from various approaches from information recorded in each meteorite group. Weiss et al. (2008) studied magnetic properties of angrites from remanent magnetization, and they considered that the angrite parent body (APB) was larger than 150 km in diameter if the remnant magnetization was achieved by the core dynamo of APB (see below for detailed discussion). Wilson and Keil (1991) considered that the aubrite parent body lost basaltic complements during explosive volcanic process. This is caused by expansion of even very small amounts of volatiles present in a melt and considering from the solubility of volatiles in basaltic melts, the aubrite parent body needs to be smaller than 200 km in diameter. The size of ureilite parent body (UPB) is roughly estimated by Michel et al. (2015) that reaccumulation of fragments took place after a collision with a smaller projectile in ~500 km body whose internal structure is like ureilite by numerical simulation. Warren (2012) considered UPB should have larger than 690 km in order to yield internal pressures prohibitive to smelting in even the shallowest and most ferroan portion of its anatectic mantle.

Among major achondrites in Table 1, angrite shows the oldest crystallization age and they retain information on the crust formation in the very early solar system. Most of the achondrites have a large proportion of shock metamorphic samples. Angrite, on the other hand, is the only achondrite group with a very small proportion of shock metamorphosed samples. This means that angrites retain early crystallization history and crystallization ages without disturbance of shock metamorphism. Its relatively small size of the parent body is another characteristic of planetesimals in the early solar system. Thus, angrites can provide important clues in order to clarify crystallization process and shock history of planetesimals in the very early solar system. In the next paragraph, I will present the important mineralogical and geochemical characteristics of angrites.

Table 1. Crystallization ages, proportion of shocked samples and the size of parent body of major achondrites.

	Crystallization ages				Proportion of shocked samples	Size of parent body (diameter)	
Angrite	4564.64	±	0.27	Ma [a]	Small	>140	km [g]
Aubrite	4562.3	±	0.4	Ma [b]	Large	<200	km [h]
Ureilite	4563	±	21	Ma [c]	Large	~500, >690	km [i,j]
HED	4563.8	±	3.8	Ma [d]	Large	525	Km [k]
Mars	4439	±	17	Ma [e]	Large	6779	Km [l]
Moon	4417	±	6	Ma [f]	Large	3475	Km [m]

[a] Amelin (2008); [b] Gilmour et al. (2009); [c] Torigoye-Kita et al. (1995); [d] Srinivasan et al. (2007), [e] Yin et al. (2014); [f] Nemchin et al. (2009); [g] Weiss et al. (2008); [h] Wilson and Keil (1991); [i] Michel et al. (2015); [j] Warren (2012); [k] Russell et al. (2012); [l,m] Seidelmann et al. (2007).

Proportion of shocked samples are judged from Meteoritical Bulletin Database.

1.3. Angrites

Angrites are igneous rocks whose crystallization ages range from 3 to 10 million years (Ma) after the formation of Calcium-Aluminum-rich Inclusions (CAIs) (e.g., Amelin, 2008a; Kleine et al., 2012; Schiller et al., 2015). Angrites are basaltic achondrites, and they are depleted in volatile elements (e.g., Na, K) and enriched in refractory elements (e.g., Ca, Al, Ti). The APB is considered to be accreted in the inner solar system from isotope compositions (e.g., Warren, 2011).

Most angrites show either quenched (Fig. 1) or slowly-cooled (Fig. 2) textures. When taking paired samples into consideration, twenty-one angrites are known considered from texture as of December 2021 (Meteoritical Bulletin Database). Among them, the quenched angrites are Asuka-881371 and its pair Asuka 12209, D'Orbigny, Lewis Cliff (LEW) 87051, NWA 1296, NWA 1670, NWA 7203, NWA 7812, NWA 12004, NWA 12320, NWA 12774, NWA 12879, NWA 12934, NWA 13363 and Sahara 99555. Quenched angrites have older crystallization ages compared with the slowly-cooled angrites. The Pb-Pb ages of quenched angrites are 4562.4 ± 1.6 Ma for Asuka-881371, 4563.49 ± 0.20 Ma for D'Orbigny, and 4564.86 ± 0.38 Ma for Sahara 99555, respectively (Zartman et al., 2006; Amelin, 2008b; Tissot and Dauphas, 2012) and those of slowly-cooled angrites are 4556.44 ± 0.30 Ma for Angra dos Reis and 4558.55 ± 0.15 Ma for LEW 86010, respectively (Amelin, 2008a; Tissot and Dauphas, 2012).

Quenched angrites usually show diabasic textures, and sometimes include dendritic intergrowths consisting of olivine and anorthite. These quenched angrites often contain Mg-rich olivine xenocrysts. On the other hand, slowly-cooled angrites show relatively granular textures. Due to the slow cooling rate, Ca-rich olivine and Ca-poor olivine sometimes form exsolution lamellae (e.g., LEW 86010). Sanborn and Wadhwa (2021) consider from REE patterns of angrites that angrite has two sources and parent melt of quenched angrites came from partial melting of one of the sources and crystallized near surface of APB. On the other hand, parent melt of slowly-cooled angrites came

from the same sources with quenched angrites' or the other sources, and slowly-cooled angrites crystallized in plutonic environment of APB (Fig. 3).

The size and the formation process of the APB are discussed in several previous studies. Core formation of APB is studied by Weiss et al. (2008), that Angra dos Reis (slowly-cooled angrite), D'Orbigny (quenched angrite) and Asuka-881371 (quenched angrite) whose ages are 4564-4558 Ma record ~10 μT of magnetic fields by an early dynamo in a rapidly formed metallic core. According to this result, Weiss et al. (2008) propose that APB was larger than 150 km in diameter. Busemann et al. (2006) analyzed the isotopic compositions of noble gases captured in D'Orbigny and found that $(^{20}Ne/^{22}Ne)_{tr}$ is 11.9 ± 0.3, which is similar to the solar composition. Although it is not clear whether the origin of noble gases is endogenic or exogenic to the APB, noble gases were trapped in the glass of quenched magma. In order to retain a nebular atmosphere, they inferred the size of APB might have been 100-200 km in diameter. On the other hand, Suzuki et al. (2014) estimated the upper limit of the diameter of APB to be 1400 ± 200 km by focusing on the spherical voids in D'Orbigny whose shape depends on the gravity scale (which depends on the diameter of APB). Spherical shape of the largest void enables to estimate the upper limit of the diameter of APB. Therefore, the current size estimate of the APB is 100-1600 km in diameter.

The origin of angritic magma is considered from partial melting experiments of carbonaceous chondrites such as CV and CM (e.g., Jurewicz et al., 1993; Mikouchi et al., 2008). Jurewicz et al. (1993) found that partial melt compositions of CV (Allende) and CM (Murchison) chondrites are similar to bulk composition of angrites when the melting was at high oxygen fugacity (fO_2) (log fO_2: two log units below the iron-wüstite buffer (IW+2)) while partial melt compositions are rather similar to eucritic bulk compositions at low fO_2 (log fO_2=IW-1). However, stable isotopic compositions of carbonaceous chondrites and angrites (e.g., $\Delta^{17}O$, ^{54}Cr, ^{50}Ti) are different (e.g., Warren, 2011).

After the core formation of APB, highly siderophile element (HSE) abundances of the mantle on APB are chondritic-relative proportions, suggesting that materials with chondritic abundance of HSE were accreted to APB (Riches et al., 2012). In addition, since N and H isotopic compositions of angrite are CM-like, it is considered that influx of volatile-rich materials from the outer solar system existed within the ~4 Myr after the formation of CAIs (Deligny et al., 2021).

Angrites almost universally lack shock metamorphism (e.g., Keil, 2012), which makes quenched angrites good time anchors (McKeegan and Davis, 2003; Brennecka and Wadhwa, 2012). Scott and Bottke (2011) inferred that the original APB was at least 100 km in diameter and probably closer to Vesta in size (Busemann et al., 2006; Weiss et al., 2008). However, the absence of shock metamorphism in angrites led them to suggest that angrites are derived from asteroids that were small, i.e., less than 10 km in diameter, and therefore survived the period of late heavy bombardment (LHB) without significant impact disruption. They proposed that a major impact on the APB occurred at ~4.5 Gyr ago, producing angritic asteroids.

However, there are two exceptional samples that show clear shock metamorphism, NWA 1670 and NWA 7203 quenched angrites. Mikouchi et al. (2003) found ~30 μm shock veins in NWA 1670. Jambon et al. (2008) suggested that olivine xenocrysts are remnants of shock melting because most olivine xenocrysts in NWA 1670 are fractured and show mosaicism while some are characterized by faint undulatory extinction. Therefore, those olivine xenocrysts may also be evidence for shock metamorphism. My preliminary report also revealed that the NWA 7203 quenched angrite showed remarkable shock metamorphism (Hayashi et al., 2018). Thick shock veins exist in NWA 7203, and some minerals show undulose extinction under polarizing microscope. The discovery of these two shocked quenched angrite samples among the total of thirteen quenched angrites casts a doubt about that the APB was broken into small asteroids during the timing of the LHB, as suggested by Scott and Bottke (2011).

Thus, quenched angrites are important samples in that they retain information about the early solar system crystallization processes and shock history. However, there are still some unresolved problems for angrites. First, quenched angrites often contain Mg-rich olivine xenocrysts, and their origin is unclear (see 4.6.). Jambon et al. (2008) implied that olivine xenocrysts might be remnant of mantle materials or crystallized from impact melts. Keil (2012) suggested a possibility that olivine xenocrysts came from impactors because they show variable Mg contents. However, no consensus has been reached.

Sanborn and Wadhwa (2021) recognized that quenched angrites crystallized near the surface, and slowly-cooled angrites crystallized in plutonic environment. The burial depth of LEW 87051 quenched angrite is estimated ~ 2 m from the surface (Mikouchi et al., 1995), and thus quenched textures are consistent with this shallow formation. However, the burial depth of LEW 86010 slowly-cooled angrite is estimated 68-75 m from the surface (McKay et al., 1998), which is too shallow to call them "plutonic". These burial depths are derived from the cooling rates of >1273 ^{o}C/yr for LEW 87051 and ~275 ^{o}C/yr for LEW 86010, respectively, estimated from atomic diffusion profiles of olivine (LEW 87051: olivine xenocryst, LEW 86010: kirschsteinite lamellae). Amelin et al. (2011) calculated the cooling rate of NWA 4590 slowly-cooled angrite from the differences of isotopic age and closure temperature of pyroxene and silico-apatite, and they concluded as 540 ± 290 ^{o}C/Ma. This cooling rate of NWA 4590 is much slower than that estimated from atomic diffusion profiles. I consider this may be due to errors of age determination and uncertainty of closure temperature. Also, the difference of temperature range between these two estimations (olivine atomic diffusion method: >>1000 ^{o}C *vs*. closure temperature method: <1000 ^{o}C) further provides large gaps. However, the important point here is that modeling the crystallization sequence of minerals will shed light on the formation history of quenched angrites in spite of the large discrepancies of estimated cooling rates.

In order to better understand the crystallization process and shock history of the APB and evolution of planetesimals in the early solar system, it is important to perform detailed mineralogy and petrology of quenched angrites. Thus, in this thesis, I report on the petrology, mineralogy, and oxygen isotope systematics of several quenched angrites and discuss crystallization process and shock history on the APB. The study of the crystallization process and shock history of APB may further clarify the evolutional history of planetesimals in the early solar system, and can assess the reasonability of quenched angrites as a time anchor for cosmochronology.

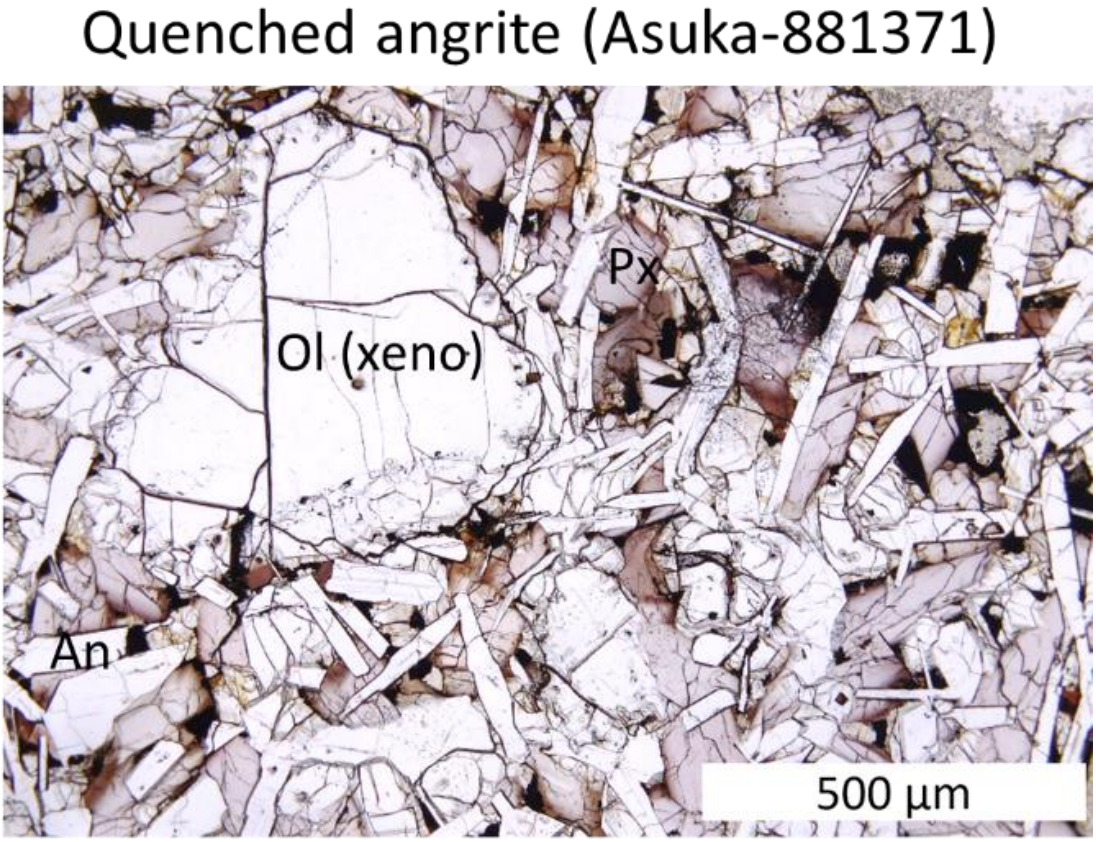

Fig. 1. Optical photomicrograph of a quenched angrite (Asuka-881371). Open nicol.

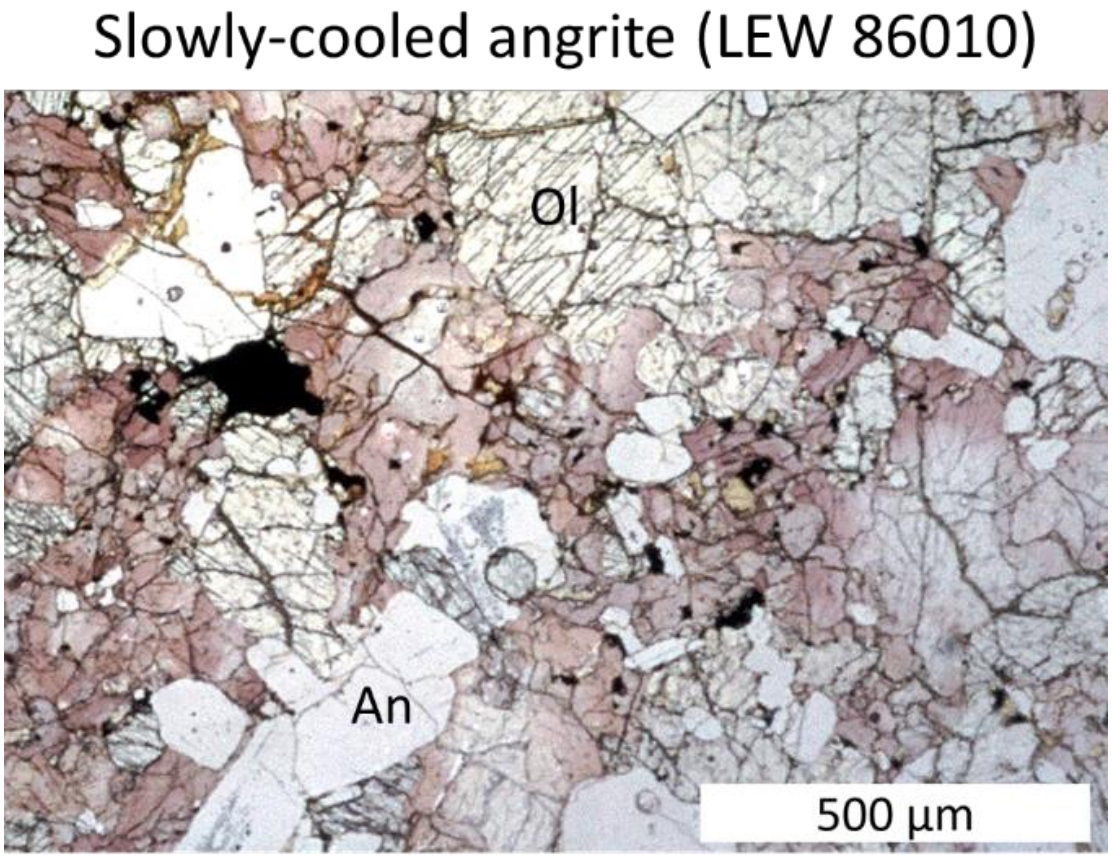

Fig. 2. Optical photomicrograph of a slowly-cooled angrite (LEW 86010). Open nicol.

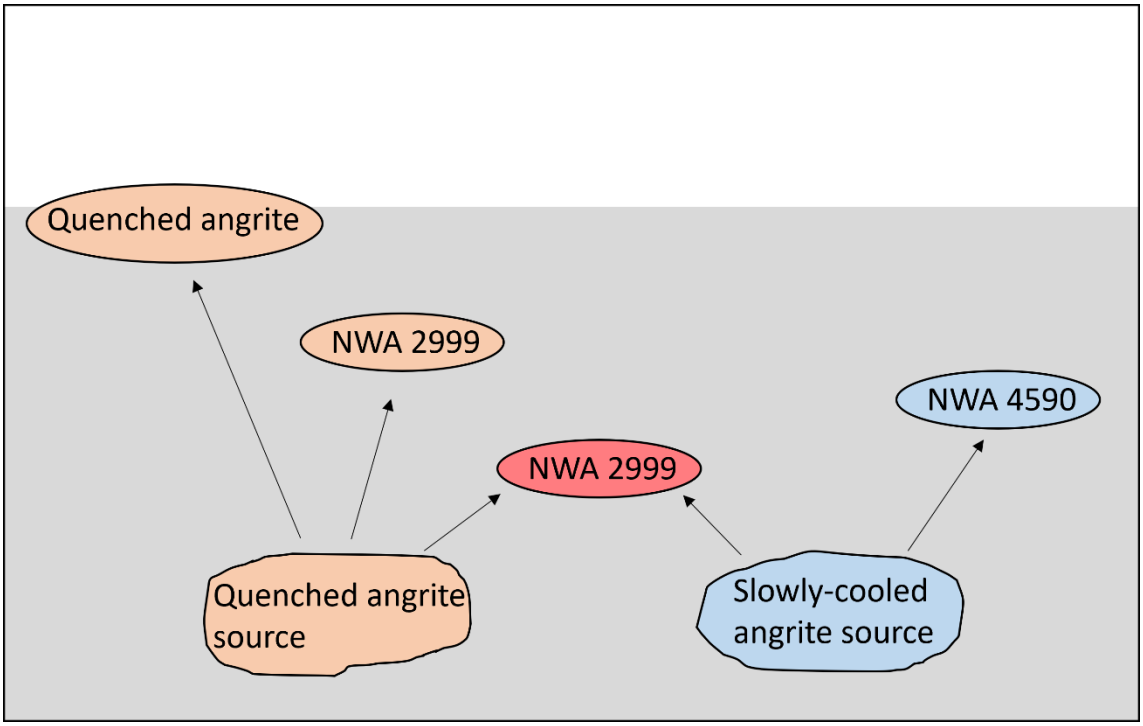

Fig. 3. Schematic illustration of source and crystallization locations of quenched and slowly-cooled angrites (after Sanborn and Wadhwa, 2021). Angrite has two sources and parent melt of quenched angrites came from partial melting of one of the sources and crystallized near surface of APB. Slowly-cooled angrites came from the same sources with quenched angrites' or the other sources, and slowly-cooled angrites crystallized in plutonic environment of APB.

2. Samples and methods

2.1. Samples

I mainly studied thin sections of D'Orbigny, Asuka-881371, Sahara 99555, NWA 1670, NWA 7203 and NWA 12774. All of them are quenched angrites. I made thin sections for NWA 7203 and NWA 12774 from their fragments that were purchased from meteorite dealers. The sample of NWA 7203 was provided from Dr. Martin Bizzarro at University of Copenhagen. The thin sections of D'Orbigny, Sahara 99555 and NWA 1670 are from the meteorite collection at the University Museum. The thin section of Asuka-881371 was loaned from National Institute of Polar Research, Japan (NIPR). The modal abundances of quenched angrites shown in previous studies are compiled in Table 2.

2.1.1. D'Orbigny

D'Orbigny was found in Argentina in 1979 and the total mass is 16.55 kg (Meteoritical Bulletin Database). Detailed petrology and mineralogy are found in Mittlefehldt et al. (2002). The modal composition of D'Orbigny is 39.4 anorthite, 27.7 Al-Ti-bearing diopside, 19.4 Mg-rich olivine, 11.9 Ca-Fe-rich olivine, 0.6 spinel, 0.5 troilite, and 0.5 calcium silico-phosphate (in vol.%) (Mikouchi and McKay, 2001). This meteorite contains rounded voids (McCoy et al., 2003). Mg-rich olivine xenocryst was also reported by Mikouchi and McKay (2001).

2.1.2. Asuka-881371

Asuka-881371 was collected in Antarctica in the 1988-1989 field season. The total mass is 11.3 g (Meteoritical Bulletin Database). Yanai (1994) and Mikouchi et al. (1996) reported detailed petrology and mineralogy. The modal composition of Asuka-881371 is 36 anorthite, 20

Al-Ti-bearing diopside, 29 olivine, 15 Ca-Fe-rich olivine, and <1 spinel, ilmenite and apatite (in vol.%) (Yanai, 1994). Abundant large Mg-rich olivine xenocryst grains occur in this meteorite (Mikouchi et al., 1996).

2.1.3. Sahara 99555

Sahara 99555 was found in the Sahara in 1999 and the total mass is 2.71 kg (Meteoritical Bulletin Database). Its detailed petrology and mineralogy are found in Mittlefehldt et al. (2002) and Mikouchi et al. (2000a). The modal composition of Sahara 99555 is 37.1 anorthite, 31.6 hedenbergite, 15.5 olivine, 13.8 kirsteinite, 1.2 troilite, 0.7 titanomagnetite and traces of phosphate and Fe-Ni metal (in vol.%) (Bischoff et al., 2000). This meteorite also contains voids as those in D'Orbigny. Olivine xenocryst is not known in Sahara 99555.

2.1.4. NWA 1670

NWA 1670 was found in Northwest Africa in 2003 and the total mass is 29 g (Meteoritical Bulletin Database). Jambon et al. (2008) reported its detailed petrology and mineralogy. The modal composition of NWA 1670 is 45 olivine, 24 diopside, 23 anorthite, 7 kirsteinite and 1 others (in vol.%) (Mikouchi et al., 2003). This meteorite contains abundant large Mg-rich olivine xenocrysts. The size of Mg-rich olivine xenocryst is up to 5 mm, and the Mg# is 0.92 to 0.85 (Keil, 2012). Mikouchi et al. (2003) reported Mg-rich olivine xenocrysts reaching Fo_{96}. This meteorite shows evidence of shock metamorphism (Mikouchi et al., 2003; Jambon et al., 2008).

2.1.5. NWA 7203

NWA 7203 was found in Morocco in 2011 and the total mass is 107 g (Meteoritical Bulletin Database). Only preliminary mineralogical study was reported by Mikouchi and Bizzarro (2012),

and thus this thesis reports the first detailed mineralogical study.

2.1.6. NWA 12774

NWA 12774 was found in Northwest Africa in 2019 and the total mass is 454 g (Meteoritical Bulletin Database). Preliminary mineralogical study is found only in Irving et al. (2020), and thus its detailed mineralogical study is first reported in this thesis.

Table 2. Modal abundances (vol%) of quenched angrites shown in previous studied.

	Fo	Fa	Kir	Px	An	Troi	Sp	Ap
D'Orbigny [1]	19.4	11.9		27.7	39.4	0.5	0.6	0.5
Asuka-881371 [2]	29		15	20	36	<1		
Sahara 99555 [3]	15.5		13.8	31.6	37.1	1.2	0.7	Tr
NWA 1670 4	45		7	24	23	1		

[1] Mikouchi and McKay (2001); [2] Yanai (1994); [3] Bischoff et al. (2000); [4] Mikouchi et al. (2003)

Fo=forsterite, Fa=fayalite, Kir=kirschsteinite, Px=pyroxne, An=anorthite, Troi=troilite, Sp=spinel, and Ap=silico-apatite.

2.2. Analytical methods

2.2.1. Optical microscope

When I made thin sections of quenched angrites, I first used ISOMET (Low Speed Precision Cutter, BUEHLER) in order to cut samples after they were embedded in New Petropoxy 154 (Maruto) resin. Because 0.15 mm thin diamond blade can be employed for ISOMET, it can minimize the sample loss by cutting. Petropoxy was also used to paste the sliced samples to glass slides. Aluminum oxide powder (#1000, #2000, #4000 and #6000) and diamond paste (1 μm) were employed in order to polish the surface. Glass slide is in a rounded shape, and its diameter is 25 mm.

I first carefully observed thin sections by optical microscope under open nicol and crossed nicols. Optical microscopy allows basic knowledge on major constituent mineral phases in thin sections and also the information about grain sizes. The shock metamorphic textures were also observed.

2.2.2. SEM

Further detailed observation was carried out using Field emission gun scanning electron microscope (FE-SEM). I used FE-SEM (JEOL JSM-7200F, Fig. 4) at Korea Polar Research Institute (KOPRI) for SEM observation mainly using back scattered electron (BSE) images. Accelerating voltage was 15 kV.

Fig. 4. FE-SEM (JEOL JSM-7200F) @KOPRI

2.2.3. EPMA

Mineral composition and elemental map were acquired using Electron Probe Micro Analyzer (EPMA). I used three EPMA instruments: FE-EPMA (JEOL JXA-8530F) at Department of Earth and Planetary Science, Graduate School of Science, The University of Tokyo and at KOPRI (Fig. 5) and EPMA (JEOL JXA-8200) at NIPR (Fig. 6). Analytical conditions for FE-EPMA were 15 kV, 12 nA with a 1 μm beam, and measurement time at the peaks and the background were 30 seconds and 15 seconds, respectively. In order to obtain accurate concentrations of minor elements in olivine, the analysis was conducted at 25 kV, 20 nA with 1 μm beam size, and measurement time at the peaks and the backgrounds for Cr and Ca were 60 seconds and 30 seconds, respectively, and those for other elements were 30 seconds and 15 seconds, respectively. Elemental map analysis was conducted at 15 kV, 60 nA. I used wollastonite for Ca and Si, Al_2O_3 for Al, TiO_2 for Ti, Fe_2O_3 for Fe, Mn olivine for Mn, MgO for Mg, albite for Na, adularia for K, Cr_2O_3 for Cr, and $KTiO(PO_4)$ for P as the standards. Quantitative analysis at 25 kV, 20 nA and 15 kV, 12 nA was calibrated by analyzing these standards each time.

FE-EPMA grid analyses were performed for NWA 7203 and NWA 12774 in order to obtain the bulk chemical compositions. Square areas were chosen, and quantitative analysis was done at even intervals. Mean values of the grid analyses are interpreted to reflect the bulk composition of measurement areas.

To obtain modal abundance, I processed the X-ray elemental maps using ImageJ software. Pixel counting was automated by ImageJ. Threshold values were chosen to correspond to each phase.

Fig. 5. FE-EPMA (JEOL JXA-8530F) @KOPRI

Fig. 6. EPMA (JEOL JXA-8200) @NIPR

2.2.4. Raman spectroscopy

I obtained Raman spectra of minerals and glasses using a micro Raman spectrometer consisting of a 50 cm single polychromator (500is Imaging Spectrograph, Chromex) and a Si-based charge coupled device camera (DU-401A-BR-DD) at Geochemical Research Center, Graduate School of Science, the University of Tokyo and JASCO NRS-1000 Raman microscope at NIPR. The excitation laser wavelength was 514.5 nm (500is Imaging Spectrograph) and 531.9 nm (JASCO NRS-1000), respectively. The laser power was 5 mW for 500is Imaging Spectrograph and 25 mW for JASCO NRS-1000. Wave number calibration was performed using naphthalene (513.6 cm^{-1}, 763.5 cm^{-1}, 1021.3 cm^{-1}, 1147.3 cm^{-1}, 1382.3 cm^{-1}, 1464.3 cm^{-1}, 1576.3 cm^{-1}) for 500is Imaging Spectrograph and silicon (520.5 cm^{-1}) for JASCO NRS-1000, respectively.

2.2.5. IRMS

Oxygen isotope ratios of NWA 12774 and NWA 7203 were measured using isotope ratio mass spectrometry (IRMS, MAT 253 plus, Thermo Fisher Scientific, Fig. 7) at KOPRI. An overview of the instrument is detailed in Kim et al. (2019). The instrument mainly consists of a reaction chamber, a purification line, and an IRMS. Approximately 2 mg of sample is placed in the reaction chamber, which is then filled with BrF_5. Fluorination is assisted by irradiation with a 25 W CO_2 laser with a wavelength of 10.6 μm by gradually increasing the laser power. Isotopic ratio of purified oxygen was measured using the IRMS. Each measurement consisted of 10 cycles with an integration time of 26 seconds. Data reproducibility was confirmed by measuring laboratory standard obsidians before and after sample measurements.

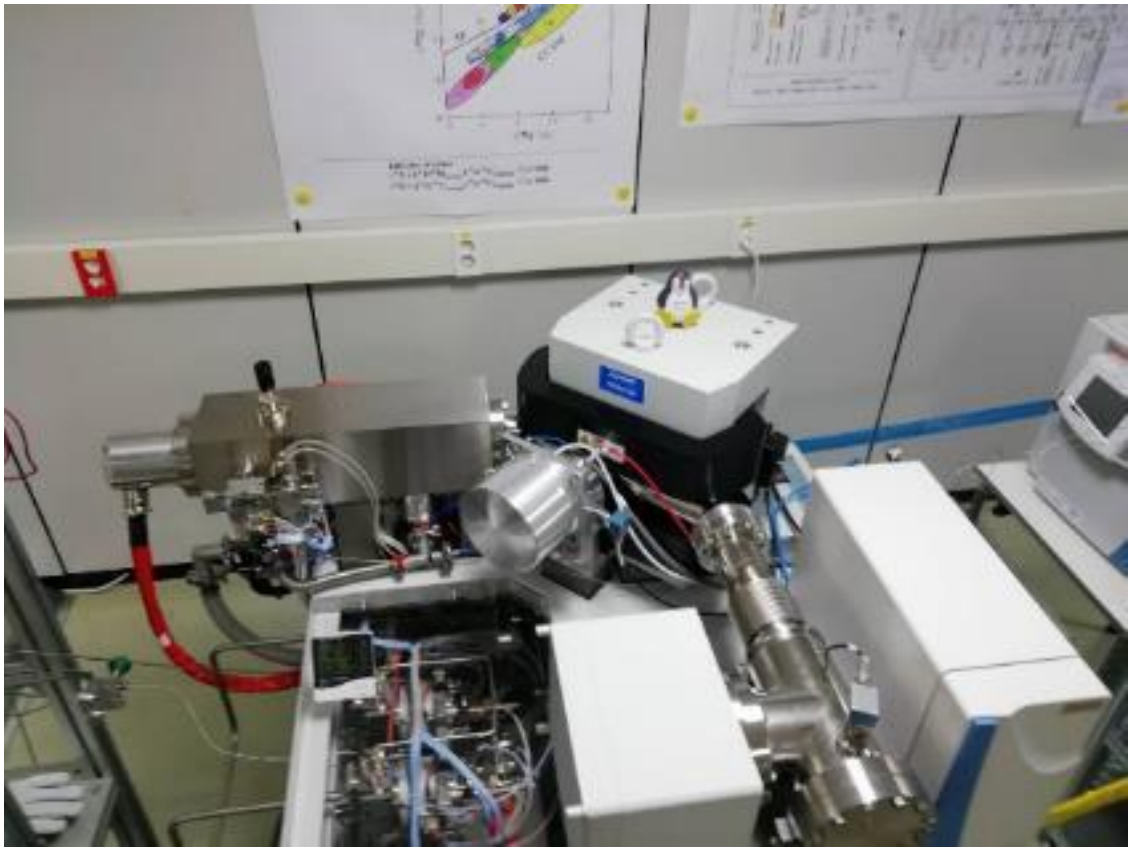

Fig. 7. IRMS (MAT 253 plus, Thermo Fisher Scientific) @KOPRI

2.2.6. Fe-XANES

In order to estimate iron valences (Fe^{2+} and Fe^{3+}) of pyroxenes in shock melted samples, I employed Fe K edge X-ray Absorption Near Edge structure (XANES) at BL-4A, Photon Factory, High Energy Accelerator Research Organization (KEK-PF) in Tsukuba city, Ibaraki prefecture (Fig. 8). Because the pre-edge peak position of Fe K-edge shifts to higher energy position with increasing Fe^{3+} ratio of the samples, this method allows micro area analysis when the X-ray beam was focused using K-B mirror (beam size at the sample position is about 5 μm) (e.g., Satake et al. 2014). Spectral crystal used at BL-4A is Si (1 1 1), with d = 3.13551(Å). 36000 pulse corresponds to 1°. The absorption energy is shown as $E = \frac{hc}{2d\sin(\sin^{-1}\left(\frac{hc}{2d*E_i}\right)+\frac{P-P_i}{36000})}\ [keV]$, where pulse number of inflection point is Pi. I estimated the ratio of Fe^{2+} and Fe^{3+} by calculating the area of both peaks by gaussian fitting. I found the area-weighted average position of the centroid peak and estimated the ratio of Fe^{2+} and Fe^{3+}. I used kaersutite from Iki island, Nagasaki Prefecture ("iki", contains 93% of Fe^{3+}) and kaersutite from kaersut, Greenland ("kst", contains 1% of Fe^{3+}) as standards.

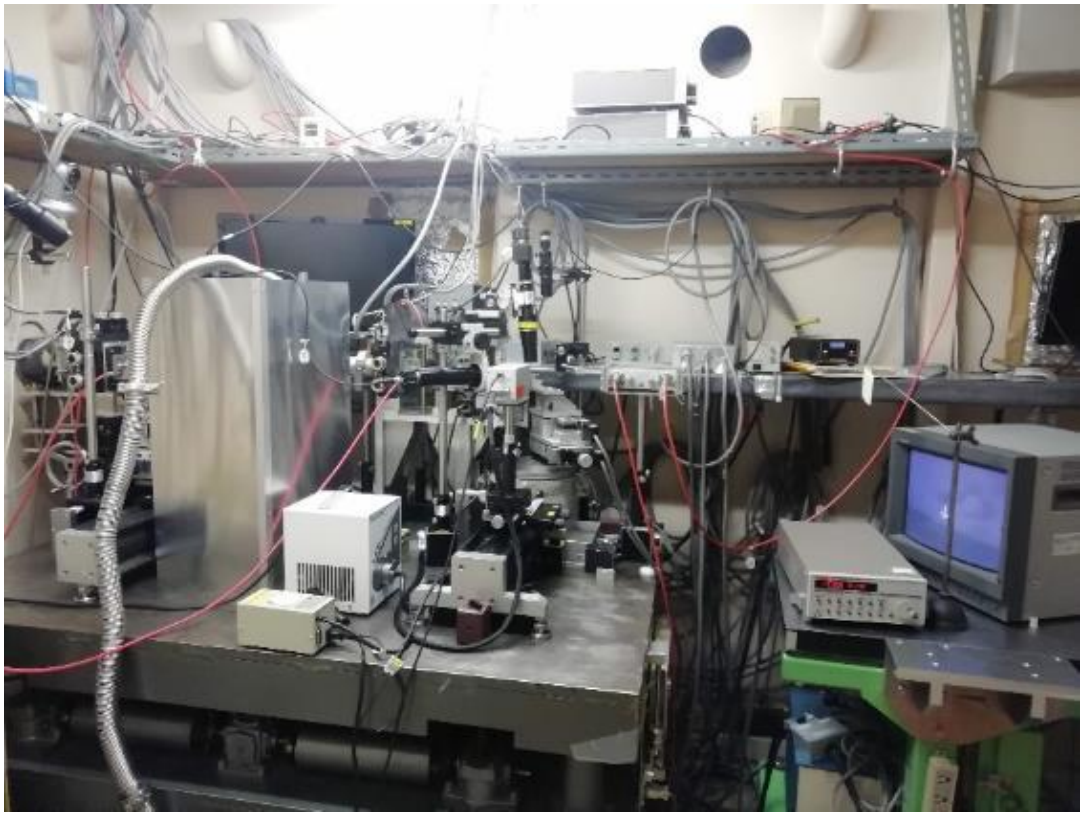

Fig. 8. BL-4A @KEK-PF

3. Results

3.1. Mineralogical and petrological description for each sample

Mineralogical and petrological studies for D'Orbigny, Asuka-881371, Sahara 99555 and NWA 1670 have been already published (e.g., Mittlefehldt et al., 2002; Mikouchi et al., 1996; Mikouchi et al., 2000a; Jambon et al., 2008). Thus, I mainly describe results from NWA 7203 and NWA 12774.

3.1.1. D'Orbigny

D'Orbigny shows a relatively coarse-grained variolitic texture (Fig. 9). D'Orbigny contains voids (Fig. 10) and also contains rare olivine xenocrysts. Fig. 11 shows one of the xenocrysts whose chemical composition is Fo_{88} (I define Fo# as mole percent of Mg/[Mg + Fe + Ca], Fa# as mole percent of Fe/[Mg + Fe + Ca], and La# as mole percent of Ca/[Mg + Fe + Ca], respectively for olivine). The Fo_{88} olivine is considered to be a xenocryst because its Fo content is clearly out of equilibrium with the bulk chemical composition of D'Orbigny (Mittlefehldt et al, 2002, see 3.3.). These olivine xenocrysts are maximum 150 μm in size in the sample studied, and these are smaller compared with those of other quenched angrites (Fig. 11). Mikouchi and McKay (2001) reported a large olivine xenocryst in D'Orbigny reaching several millimeters, but such large olivine grains were not found in my sample. D'Orbigny mainly consists of olivine, clinopyroxene and anorthite. Fig. 12 shows the Mg X-ray map of D'Orbigny. Warm color indicates high Mg content. In this figure, Mg-rich grains shown in red color are olivine xenocrysts, while olivine phenocrysts are shown in green color. Olivine phenocrysts have almost the same Fo# in the core. Clinopyroxenes are shown in blue color, and anorthites are shown in dark color. There are two types of olivine phenocrysts, small olivine phenocrysts and large olivine phenocrysts. Small olivine phenocrysts are around 100 μm, and large olivine phenocrysts are from several hundreds μm to 1 mm. The size of anorthite shows the

same tendency as olivine, and there are small anorthites and large anorthites. Small anorthites are around 100 μm, and large anorthites are from several hundred μm to 1 mm. Small olivines and small anorthites are co-existing as intergrowth. Clinopyroxenes are several hundreds μm in size.

I estimated cooling rates of D'Orbigny from atomic diffusion profiles recorded in olivine xenocryst. Because it is obvious that the originally homogeneous olivine crystals (xenocrysts) were interacted with the surrounding magma as the case for megacrystic olivine xenocrysts (e.g., Asuka-881371, see the following chapters), resulting in partial resorption and overgrowth of iron-enriched rims. The compositional gradients at these rims were produced by atomic diffusion, and thus these zoning profiles could be used to estimate cooling rates of xenocryst-bearing samples assuming a reasonable condition. To do this, I obtained EPMA line profiles of olivine xenocrysts (Fig. 13, red arrow part of Fig. 11). Line profiles of Fo, Fa and La contents are shown in Fig. 13. The chemical compositions of olivine xenocrysts in D'Orbigny display Fo-rich homogeneous core and clear overgrowth. The core part shows a flat compositional pattern and chemical composition gradually changes Fe-rich towards the rim at the overgrowth area. Between core and overgrowth, chemical composition suddenly changes, which marks the front where atomic diffusion reached. Because diffusion coefficients of calcium and chromium in olivine are smaller than that of magnesium and iron (e.g., Chakraborty, 2010), the compositional gradients are steeper at the La profile, which further supports the idea that the compositional change was caused by atomic diffusion. I choose the boundary of olivine xenocryst and overgrowth to estimate the cooling rates by the La profile (red solid line shown in Fig. 13), because the La profile is considered to best retain an original chemical compositional trend compared from other elements with larger diffusion coefficients. I choose the other end of the area to estimate the cooling rates by the Fa profile, where chemical composition is homogeneous (red dotted line shown in Fig. 13). I estimate the cooling rates by calculating diffusion profiles from 1400 ^{o}C to 900 ^{o}C at logfO_2=IW+2 (Jurewicz et al. 1993) at

the enclosed area with red solid line (boundary of olivine xenocryst and overgrowth) and red dotted line (homogeneous core of the olivine xenocryst) shown in Fig. 13. Mikouchi et al. (1994) conducted crystallization experiments and found that bulk chemical compositions of quenched angrite (LEW 87051) magma melted completely at 1430 ºC and it crystallized olivine at 1400 ºC. Based on this experimental works, I adopted a starting temperature of 1400 ºC for calculation. I employed a diffusion coefficient of Fe-Mg in olivine from Misener (1974) as this coefficient provided a good match between the experimentally produced and the calculated profiles as demonstrated by Miyamoto et al. (2002). Linear cooling is assumed in this calculation. The diffusion equation is given as below.

$$\frac{\partial C}{\partial t} = \frac{\partial}{\partial x}\left(D\frac{\partial C}{\partial x}\right)$$

where *C*, *x* and *t* are the Fa component, position, and time, respectively.

The boundary conditions are $\frac{\partial C(0,t)}{\partial x} = 0$ and $C(X,t) = Cs$, where position *X* and *Cs* are at the interface between olivine and the adjacent matrix and the concentration at the grain boundary with matrix. Initial condition is $C(x,0) = C_I$, where C_I is an initial concentration profile. Accordingly, the obtained cooling rate of D'Orbigny is 100 ºC/hr (Fig. 14).

Cooling rates could be affected by cut angle of olivine crystals, and thus the best estimation for cooling rates could be obtained by calculating cooling rates for several olivine xenocrysts and choosing the fastest cooling rates (considered to be the olivine grain cut at the most vertical angle). Thus, in the line profile of Fig. 13, I choose the right side (steeper profile compared from the left side) to estimate the cooling rate. Note that cooling rates can be easily affected not only by cut angle, but also starting temperature and diffusion coefficient, and thus the obtained cooling rate could contain several tens % error. However, it is enough useful to make a relative comparison of cooling rates of each sample and discuss their relative burial depths.

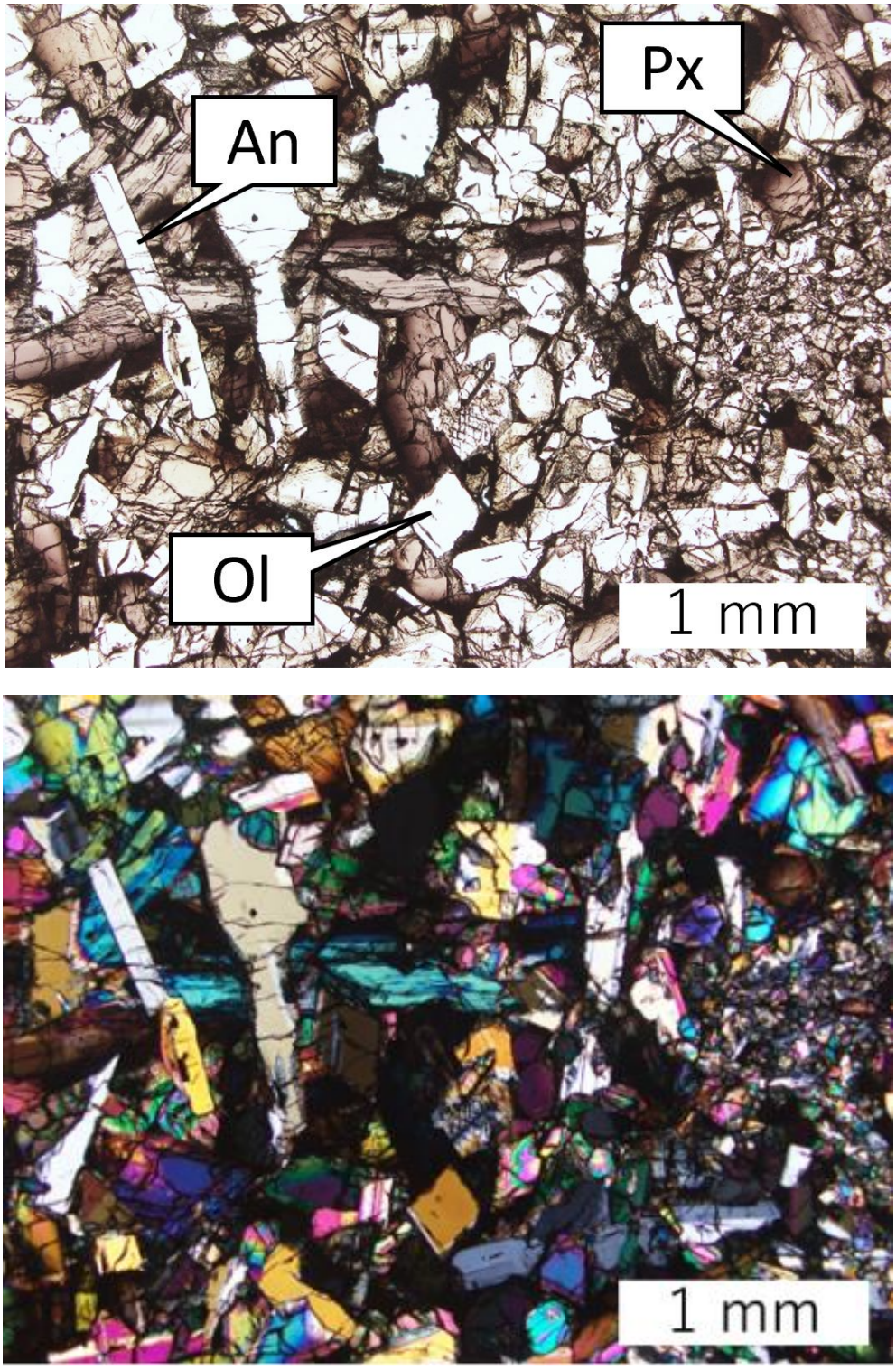

Fig. 9. Open nicol (upper) and crossed nicols (lower) optical photomicrographs of D'Orbigny.

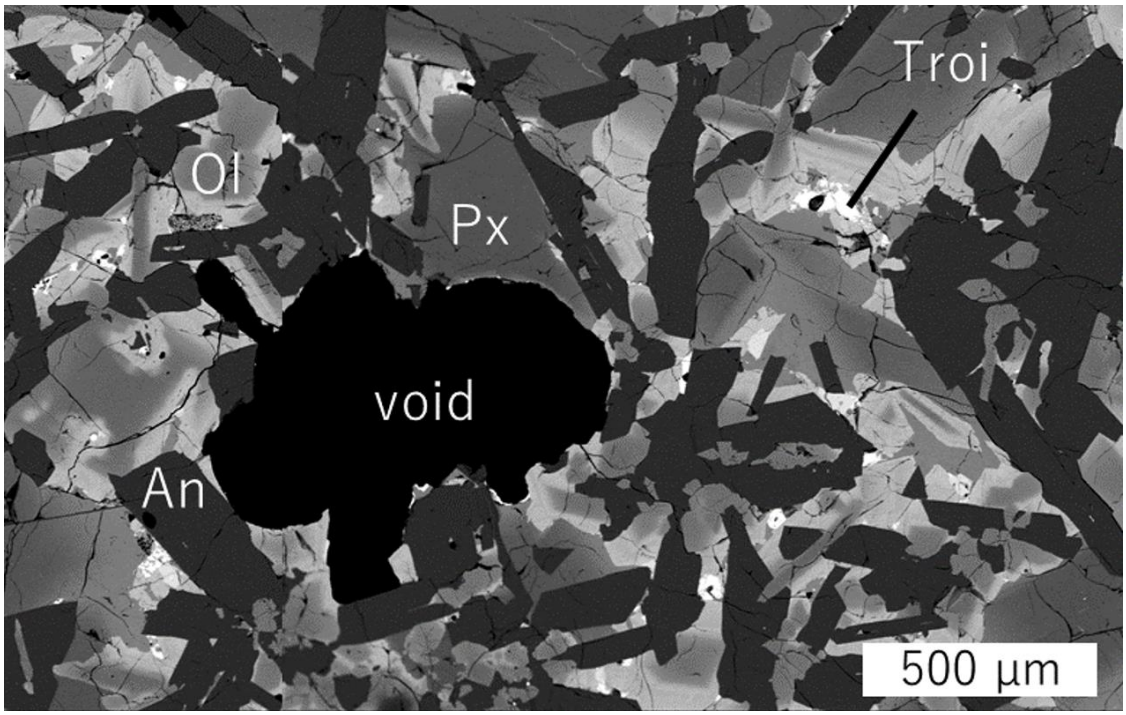

Fig. 10. BSE image of D'Orbigny. Black area indicates the void of D'Orbigny., which is commonly found in this meteorite.

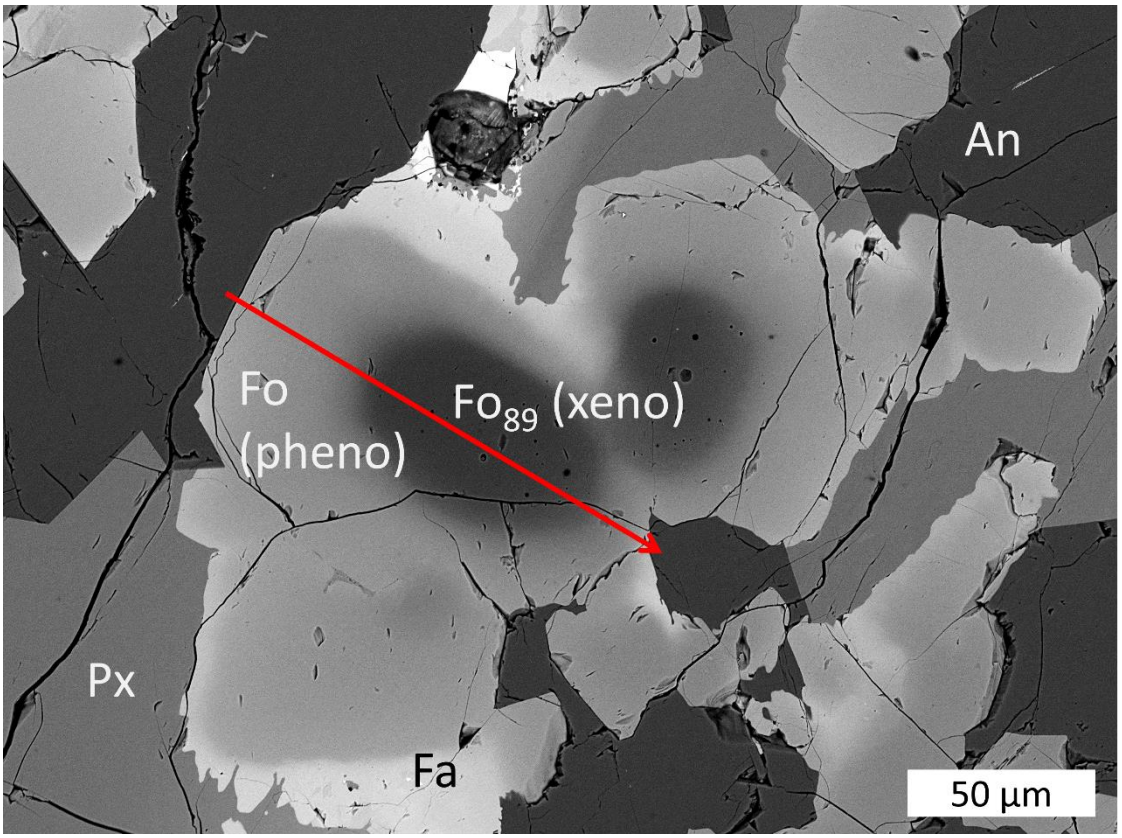

Fig. 11. BSE image of olivine xenocrysts (only relict cores of these grains) in D'Orbigny. This olivine xenocryst exists in the red square of Fig. 12. Line profiles of the red arrow part are shown in Fig. 13. The boundary between xenocrystic core and overgrowth corresponds to dark gray and gray areas of the BSE image.

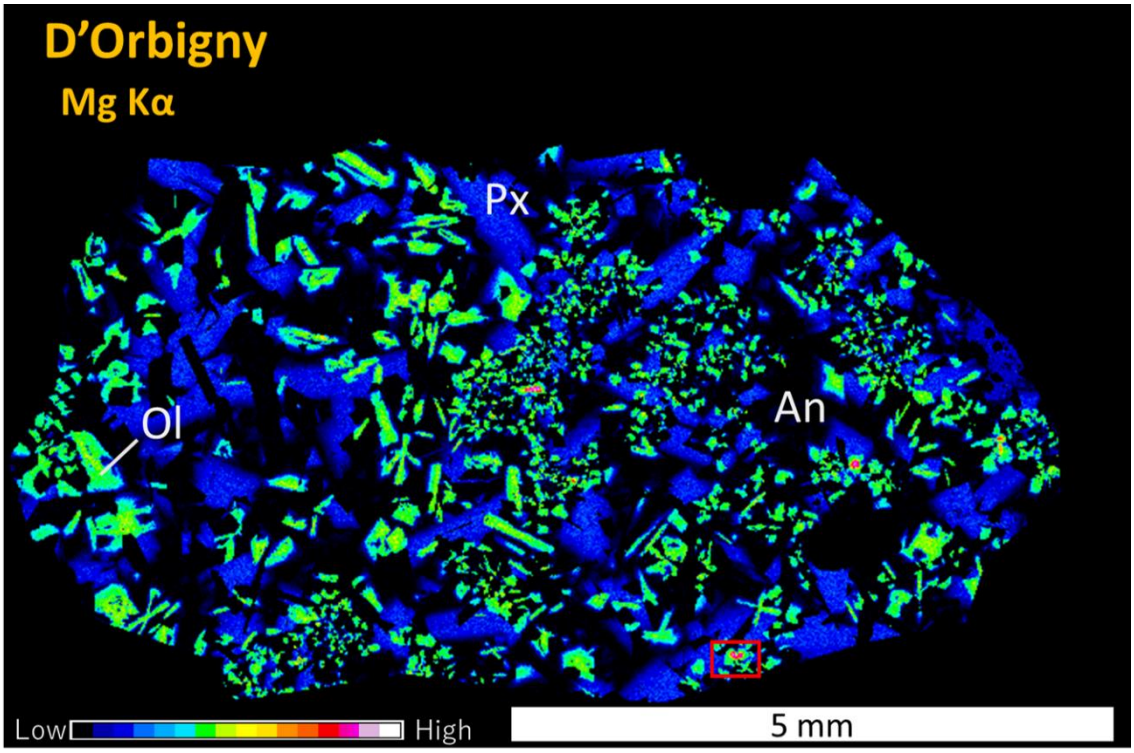

Fig. 12. Mg X-ray map of D'Orbigny. Warm color indicates the high concentration of Mg. Mg-rich olivine grains are found inside the red square. BSE image of these olivines is shown in Fig. 11.

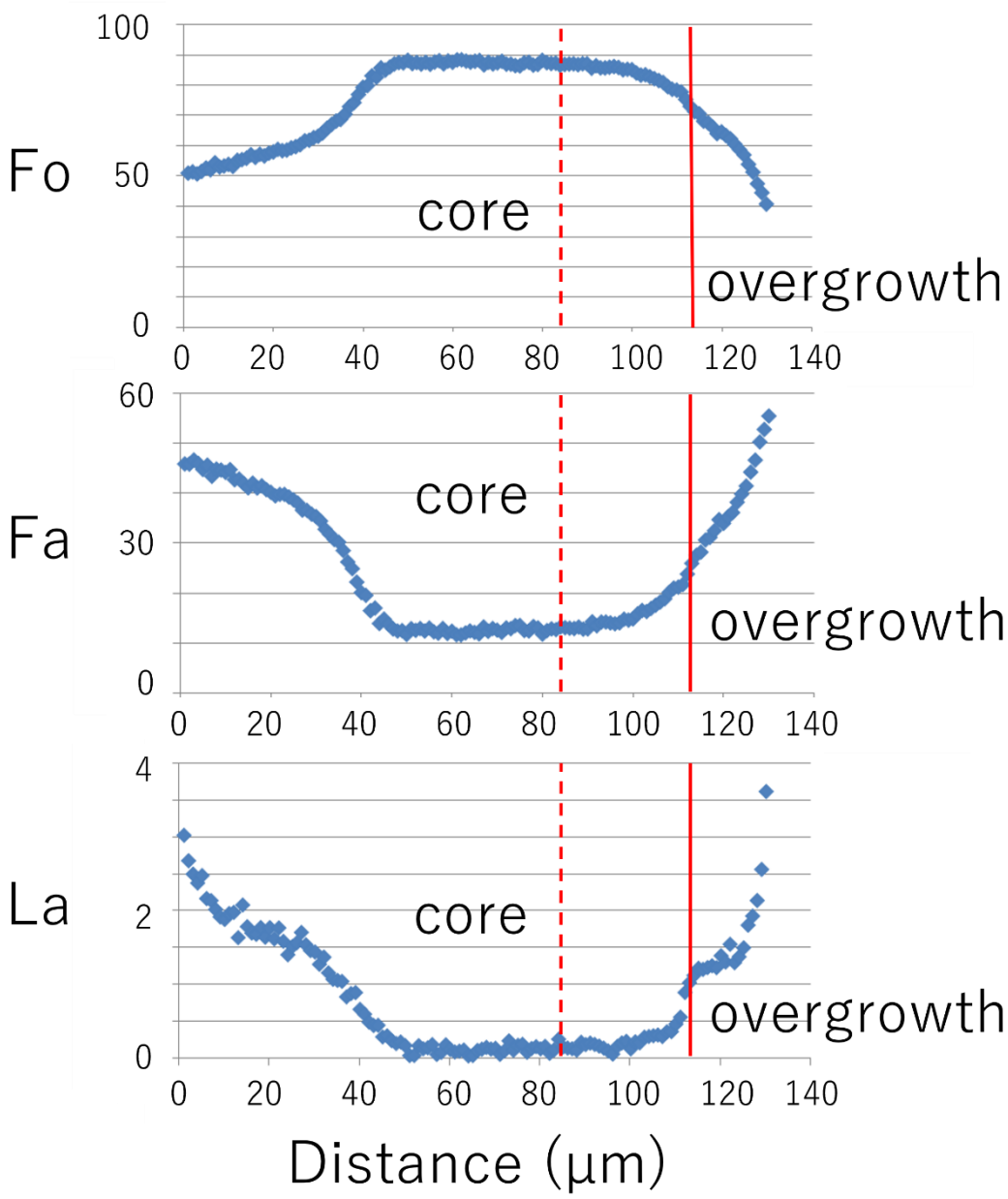

Fig. 13. Obtained EPMA line profiles of olivine xenocryst in D'Orbigny (red arrow part of Fig. 11). Red solid line corresponds to the boundary of olivine xenocryst and overgrowth assumed from the La profile. Red dotted line corresponds to the homogeneous core of olivine xenocryst assumed from the Fa profile.

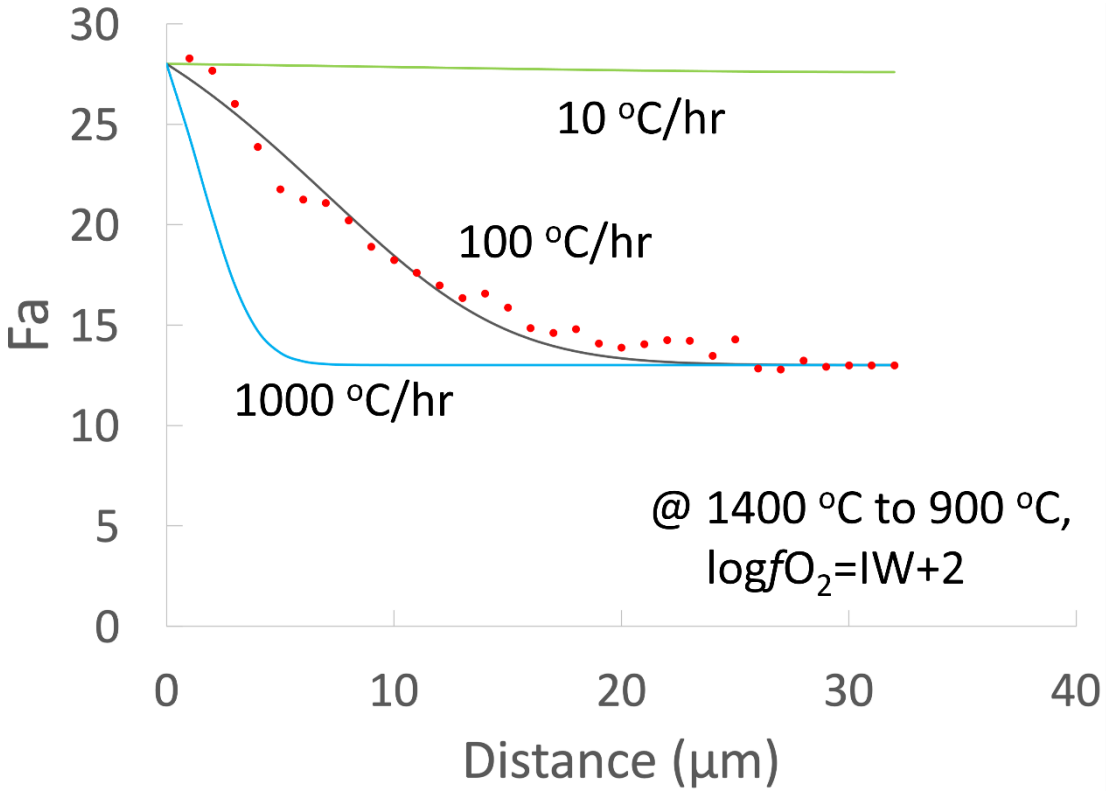

Fig. 14. Estimation for cooling rate of D'Orbigny. Cooling rate is estimated at the enclosed area with red solid line and red dotted line shown in Fig. 13. The best-fit cooling rate is 100 °C/hr. Cooling rates of 10 °C/hr and 1000 °C/hr are also shown for comparison.

3.1.2. Asuka-881371

Asuka-881371 exhibits a relatively coarse-grained texture compared to D'Orbigny (Fig. 15). Olivine megacrysts are mostly 1 mm in size with round shape, but some reach 3-4 mm. They are interpreted to be xenocrysts (e.g., Mikouchi et al. 1996). Fig. 16 is a closeup image of one of such xenocrysts with a core chemical composition of Fo_{89}. The Fo_{89} olivine is out of equilibrium with the bulk chemical composition of Asuka-881371 (Yanai 1994, Mikouchi et al. 1996, Jambon et al, 2005, see 3.3.) as similar to D'Orbigny. Major minerals of Asuka-881371 are olivine, clinopyroxene and anorthite. Fig. 17 is a Mg X-ray map of Asuka-881371. Olivine xenocrysts are shown in orange to pink color. They show large areas of homogeneous cores, but individual grains have different Mg-Fe contents. Olivine phenocrysts are shown in green color in the Mg X-ray map. These olivine phenocrysts contain relatively similar amounts of Mg in the cores, and they could be phenocrysts considering the bulk chemical compositions (see 3.3.). Clinopyroxenes are shown in blue color, and anorthites are shown in dark color, respectively. In the figure, olivine phenocrysts, clinopyroxene and anorthite phenocrysts are several hundreds μm in size.

EPMA line profiles of Fo, Fa and La contents of olivine xenocryst are shown in Fig. 18 (red arrow part of Fig. 16). As a similar manner to the D'Orbigny xenocrysts, I estimated the cooling rates by calculating atomic diffusion profiles produced at the rim by interacting with the surrounding melt (between red solid and dotted lines shown in Fig. 18). The obtained best fit cooling rate of Asuka-881371 is 50 ^{o}C/hr (Fig. 19).

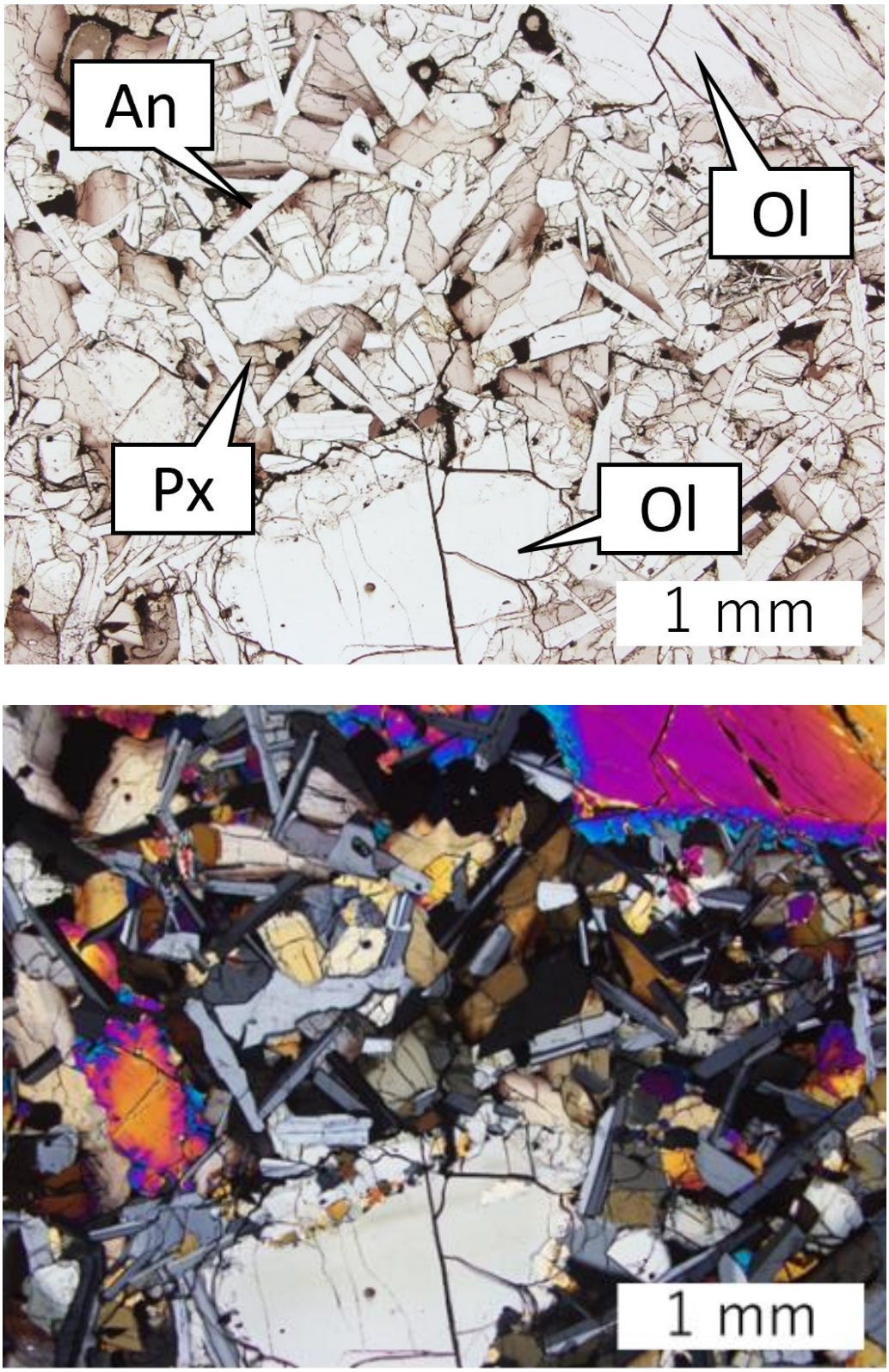

Fig. 15. Open nicol (upper) and crossed nicols (lower) optical photomicrographs of Asuka-881371.

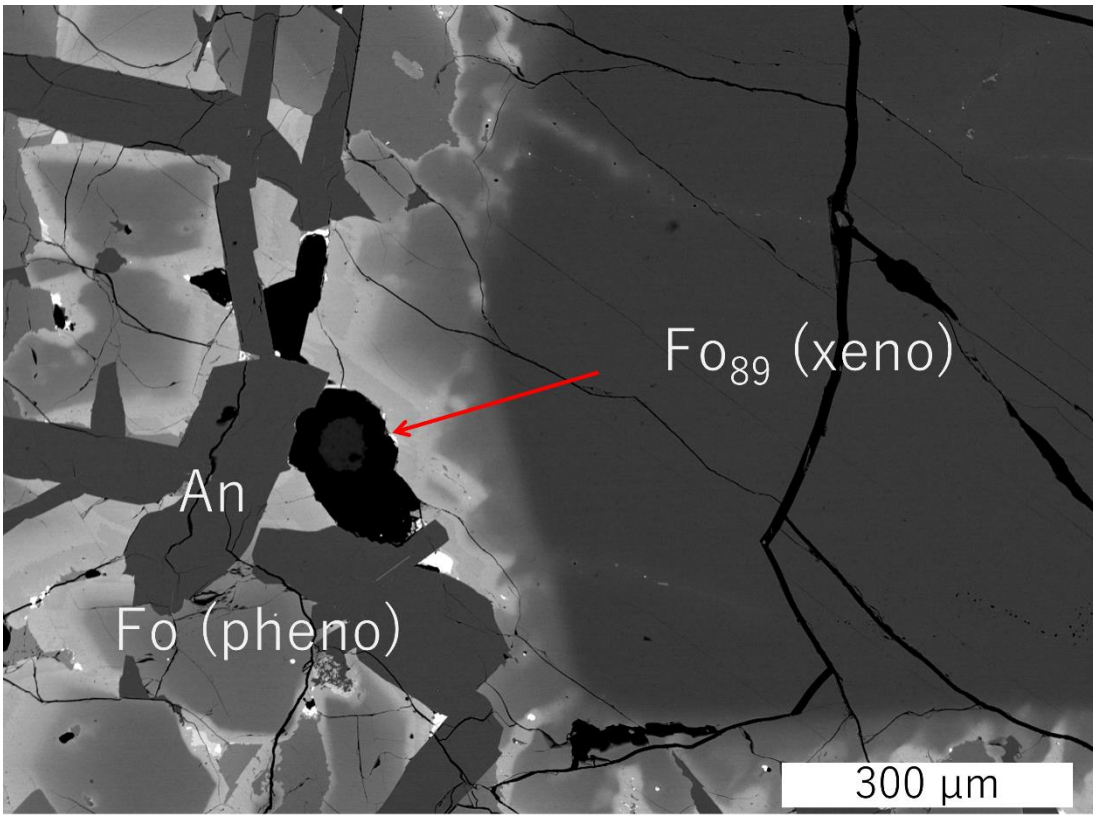

Fig. 16. BSE image of olivine xenocryst in Asuka-881371. This olivine xenocryst is present in the red square of Fig. 17. Line profiles of the red arrow part are shown in Fig. 18. The boundary between xenocrystic core and overgrowth corresponds to dark gray and gray areas of BSE image.

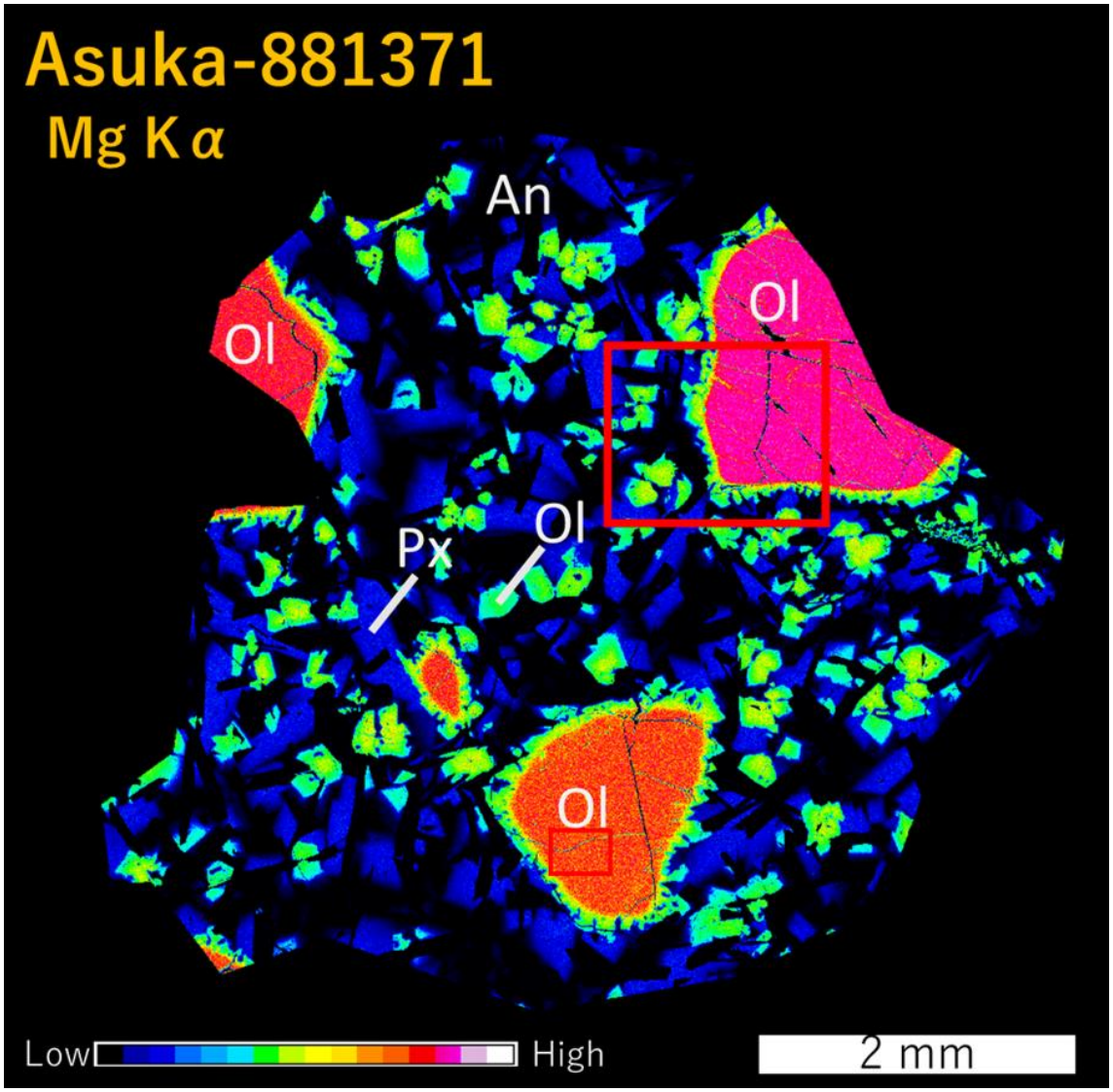

Fig. 17. Mg X-ray map of Asuka-881371. Warm color indicates the high concentration of Mg. BSE image of olivine in red square is shown in Fig. 16.

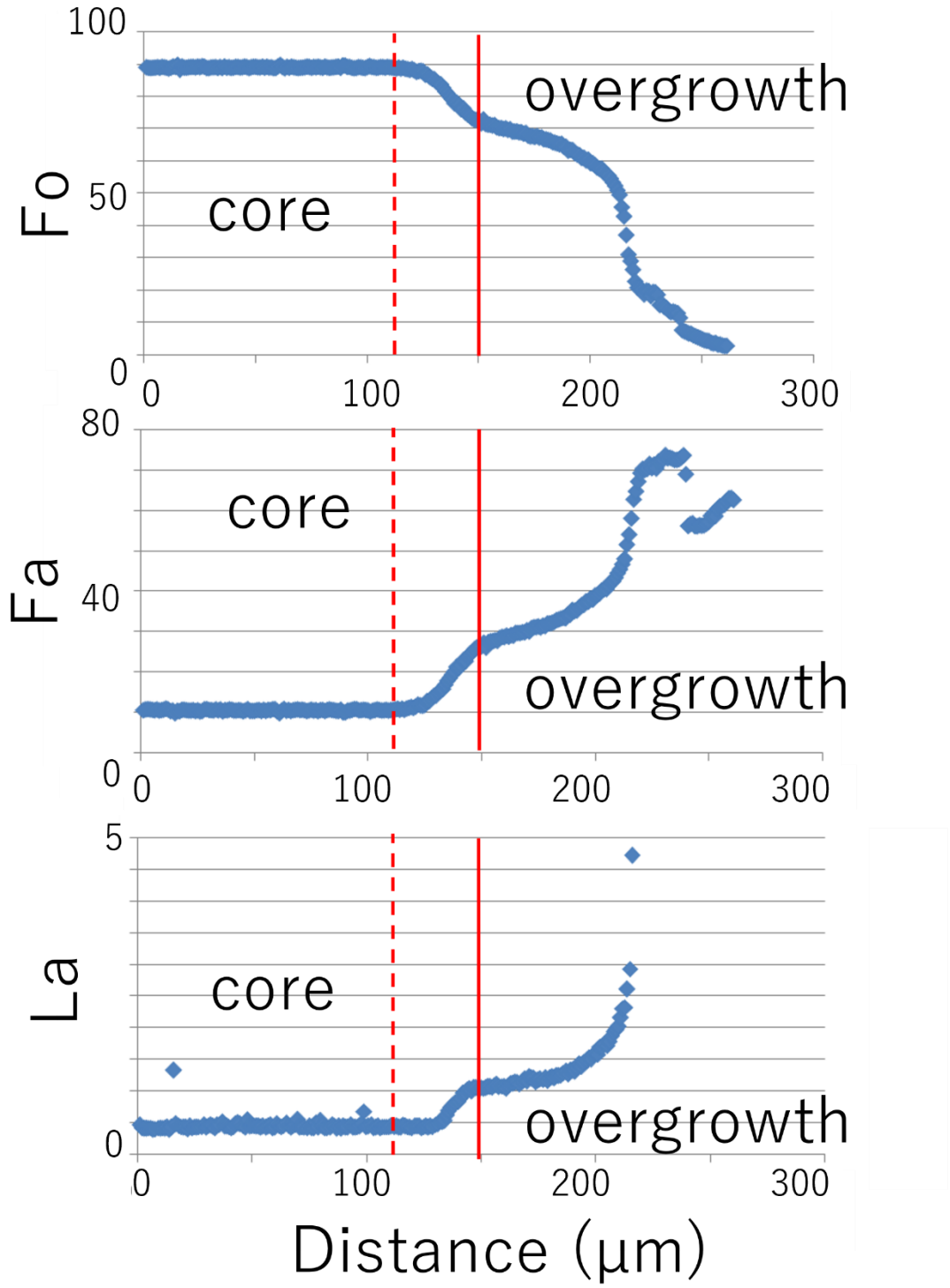

Fig. 18. Line profiles of olivine xenocryst in Asuka-881371 (red arrow part of Fig. 16). Red solid line corresponds to the boundary of olivine xenocryst and overgrowth assumed from the La profile. Red dotted line corresponds to the homogeneous core of olivine xenocryst assumed from the Fa profile.

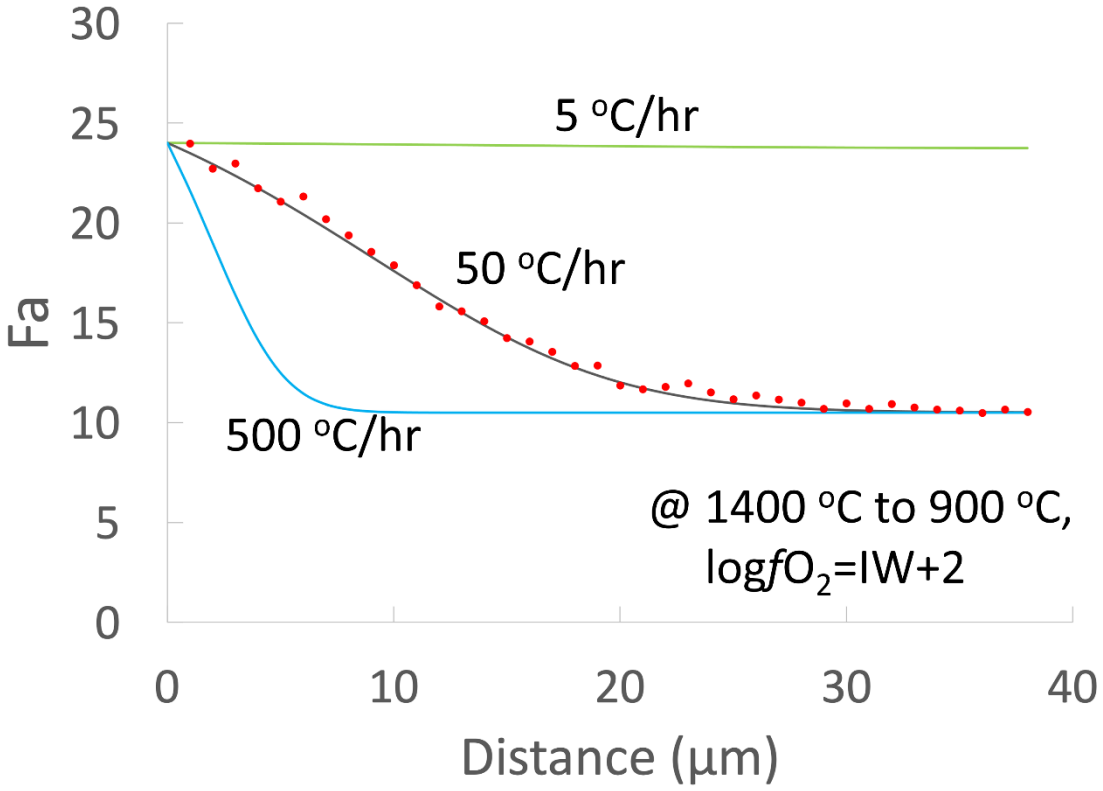

Fig. 19. Estimation for the cooling rate of Asuka-881371. Cooling rate is estimated at the enclosed area with red solid line and red dotted line shown in Fig. 18. The best-fit cooling rate is 50 °C/hr. Cooling rates of 5 °C/hr and 500 °C/hr are also shown for comparison.

3.1.3. Sahara 99555

Sahara 99555 shows a coarse-grained texture similar to those of D'Orbigny and Asuka-881371, but it is slightly finer-grained (Fig. 20). Unlike D'Orbigny and Asuka-881371, Sahara 99555 contains dendrites consisting of olivine and anorthite. Olivine xenocrysts are not found in the thin section studied. Sahara 99555 mainly consists of olivine, clinopyroxene and anorthite. Fig. 21 shows a Mg X-ray map of Sahara 99555, showing the presence of olivine crystals. There are two types of olivine grains: single crystal and constituent of dendrites. From the Mg X-ray map, the single crystal olivine is more Mg-rich (~Fo_{64}, shown in orange color) compared with the dendritic olivine (~Fo_{53}, shown in green color). These olivine compositions are in equilibrium with the bulk chemical composition of Sahara 99555 (see 3.3.), and thus these olivines are phenocrysts. Single olivine crystals sometimes show a hopper shape. Clinopyroxenes are shown in blue color, and anorthites are shown in dark color. Anorthites are elongated in shape (1 mm in length and 100 μm in width). They occasionally grow from the wall of olivine single crystals as crystallization seeds. Anorthites in dendrites are smaller, and they are around several hundreds μm in size. Olivine single crystals are several hundreds μm, and sometimes reach 1 mm. Olivines consisting of dendrites are smaller, and around 100 μm in size. Clinopyroxenes are several hundreds μm in size.

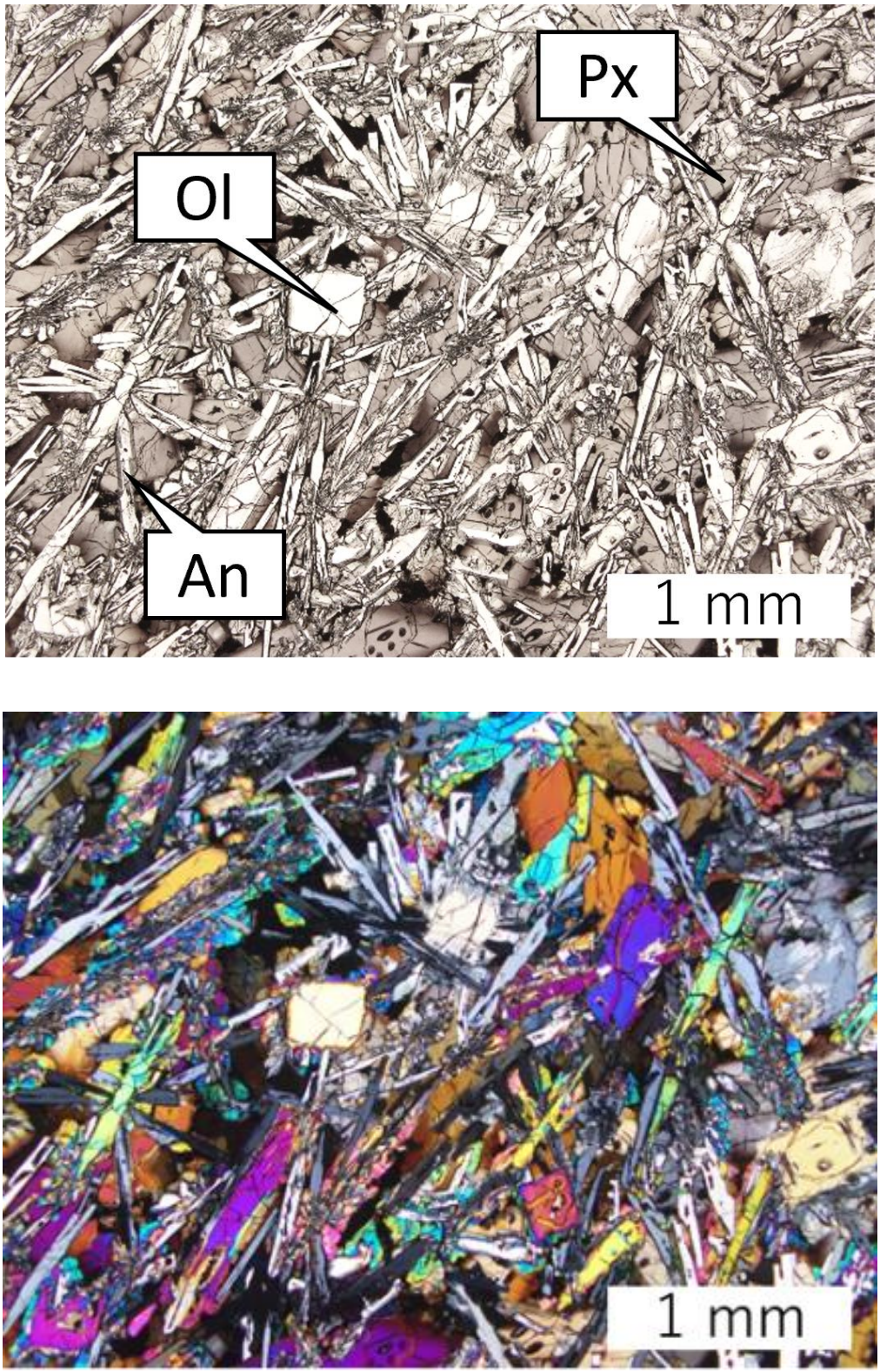

Fig. 20. Optical photomicrograph of Sahara 99555. Open nicol (upper) and crossed nicols (lower).

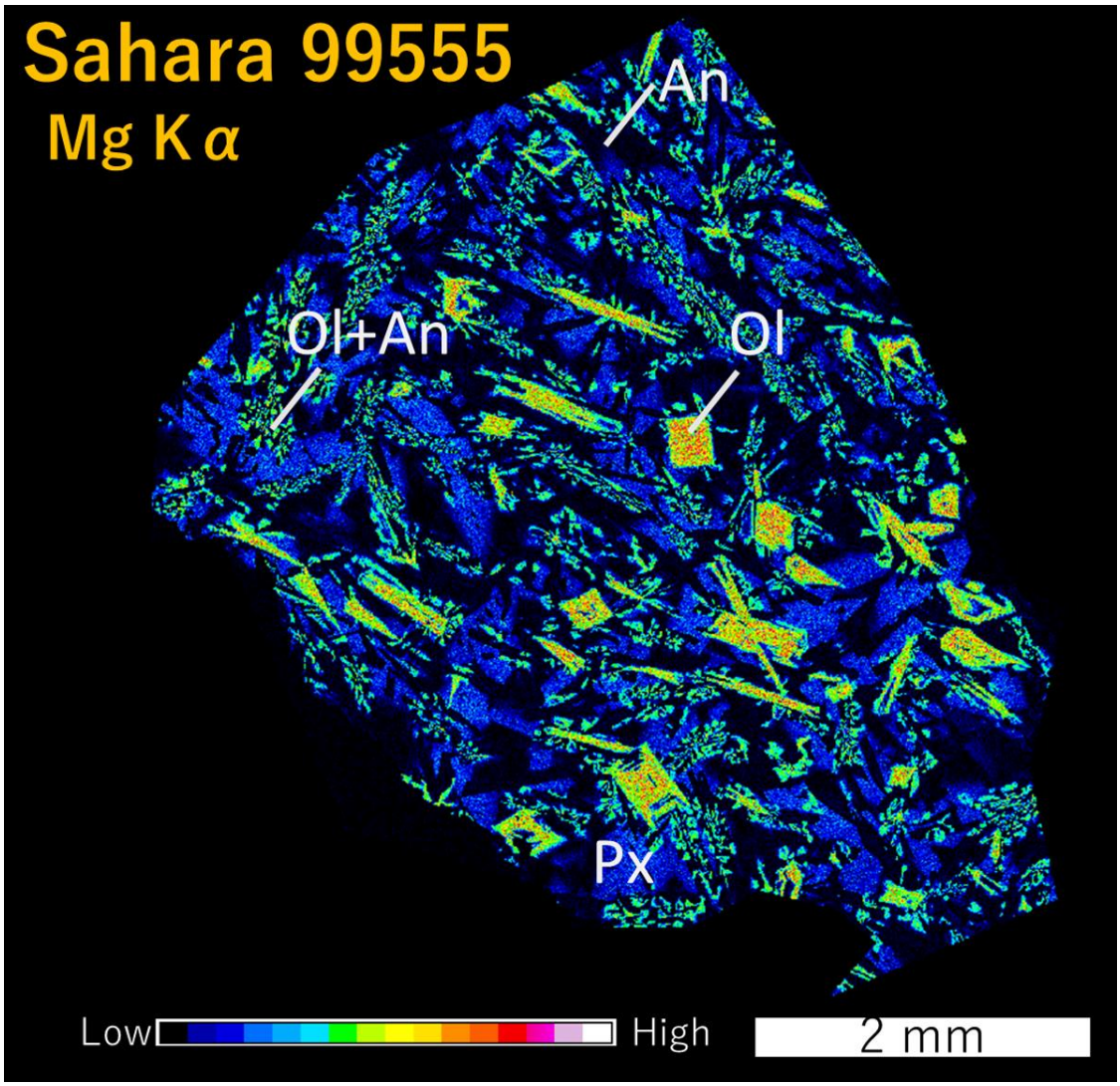

Fig. 21. Mg X-ray map of Sahara 99555. Warm color indicates the high concentration of Mg. Hopper shape olivine phenocrysts (shown in yellow to orange color) are obvious in this map.

3.1.4. NWA 1670

NWA 1670 contains ~5 mm olivine megacrysts (Fig. 22) and is characterized by an anorthite spinifex texture as shown in Fig. 23. Anorthite exhibits an extremely elongated shape (some reach ~ 1 mm in length and 10 μm in width), and they show parallel assembly. Olivine megacrysts (~5 mm)with Fo_{92} compositions are clearly xenocryst as judged from the bulk chemical composition of NWA 1670 (Jambon et al, 2008, see 3.3.) although its bulk composition is also more Mg-rich than other samples (Fig. 24. Such Mg-rich olivine is common in NWA 1670 and is slightly more Mg-rich than other samples described above. Fig. 25 shows a Mg X-ray map of NWA 1670. From the Mg X-ray map, olivine xenocrysts are shown in yellow to pink color. They are rounded in shape. Olivine phenocrysts are often overgrown on the wall of olivine xenocrysts as crystallization seeds, exhibiting a tooth-shape. Some olivine phenocrysts are euhedral in shape. Olivine phenocrysts are also found between the anorthite laths. This type of olivine phenocrysts is Fe- and Ca-rich. Clinopyroxenes are mostly found between the anorthite laths. Sometimes large (~100 μm) clinopyroxenes are found in the groundmass.

I obtained EPMA line traverses of Fo, Fa and La contents of olivine xenocrysts as shown in Fig. 26 (red arrow part of Fig. 24) to estimate cooling rates of NWA 1670 as I did for D'Orbigny and Asuka-881371. In this calculation I also assumed that the cooling was from 1400 ^{o}C to 900 ^{o}C linearly at $\log fO_2$=IW+2 and the diffusive modification of the originally homogeneous composition was applied to the enclosed area with red solid and dotted lines shown in Fig. 26. The obtained cooling rate of NWA 1670 is 3 ^{o}C/hr (Fig. 27).

NWA 1670 has a clear shock texture as shock veins are found in this meteorite. These shock veins are mostly around 50 μm in width and they turned into glass (Fig. 28). In some parts, shock vein cut original igneous textures (~100 μm displacement, Fig. 29). In addition, recrystallized clinopyroxenes are sometimes found in shock veins. Fig. 30 shows the recrystallized clinopyroxene

from one of glassy shock veins. They are several μm in size. This pyroxene has a chemical composition of diopside ~ kushiroite judged by the stoichiometry of pyroxene. XANES spectrum of this recrystallized pyroxene is obtained, and the result is shown in 3.6.

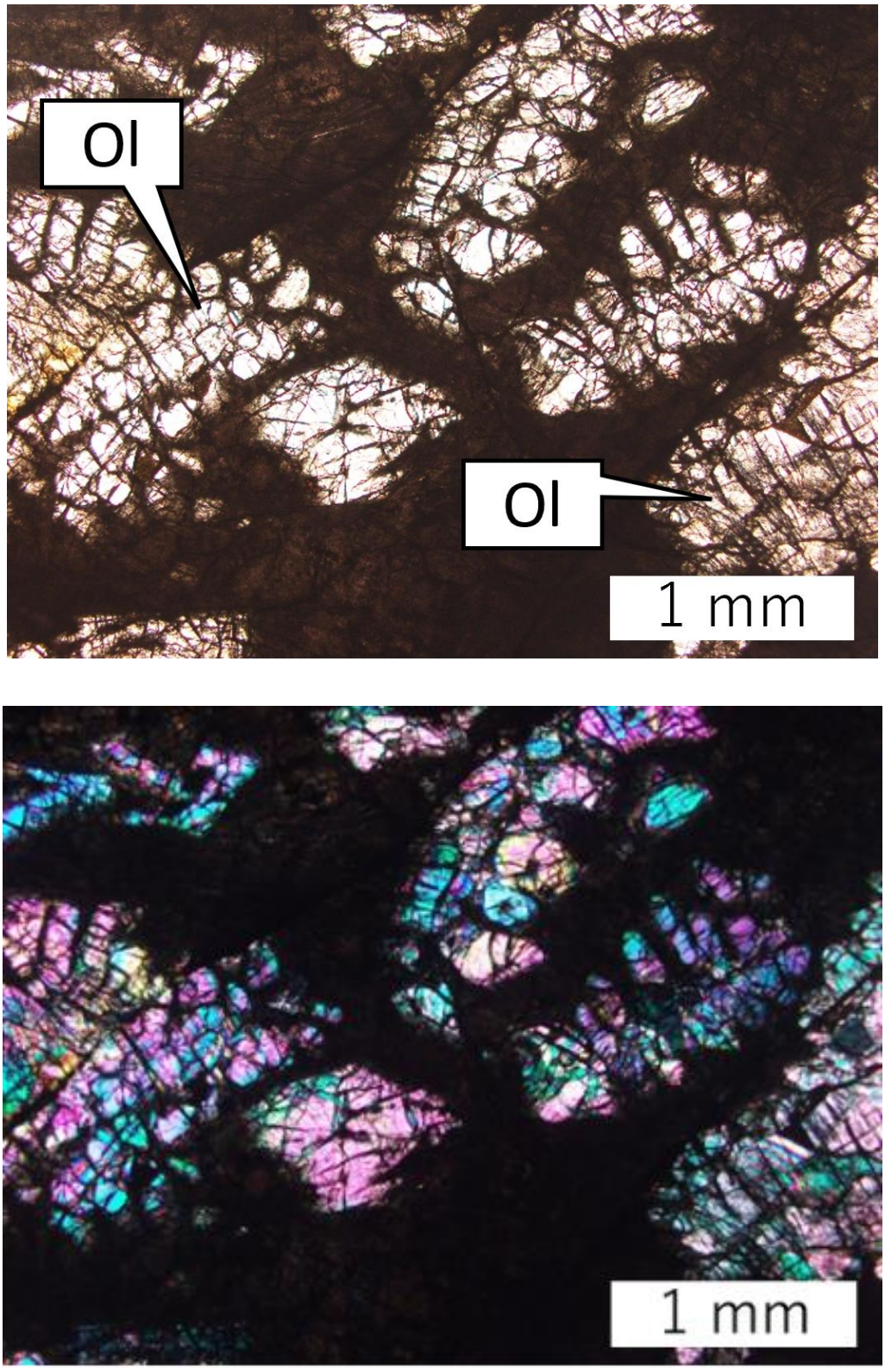

Fig. 22. Open nicol (upper) and crossed nicols (lower) optical photomicrographs of NWA 1670.

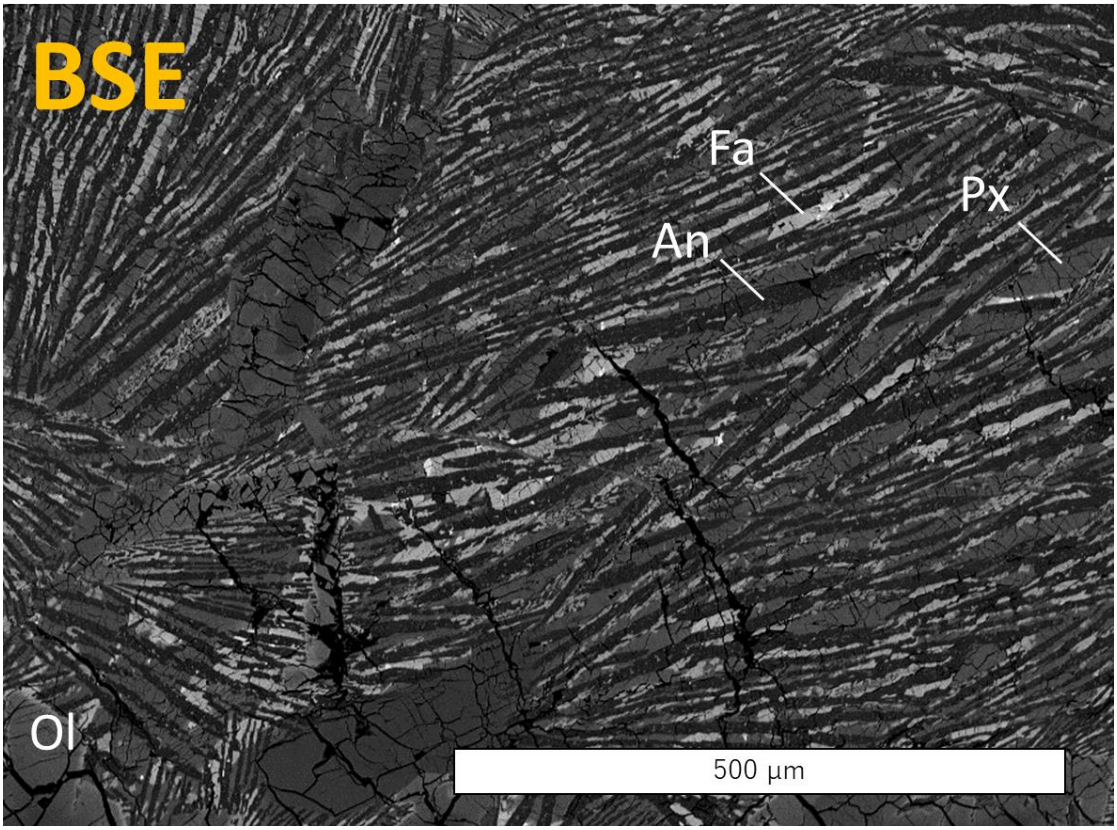

Fig. 23. BSE image of the anorthite spinifex texture. Anorthite exhibits an extremely elongated shape (some reach ~ 1 mm in length and 10 µm in width), and they show parallel assembly.

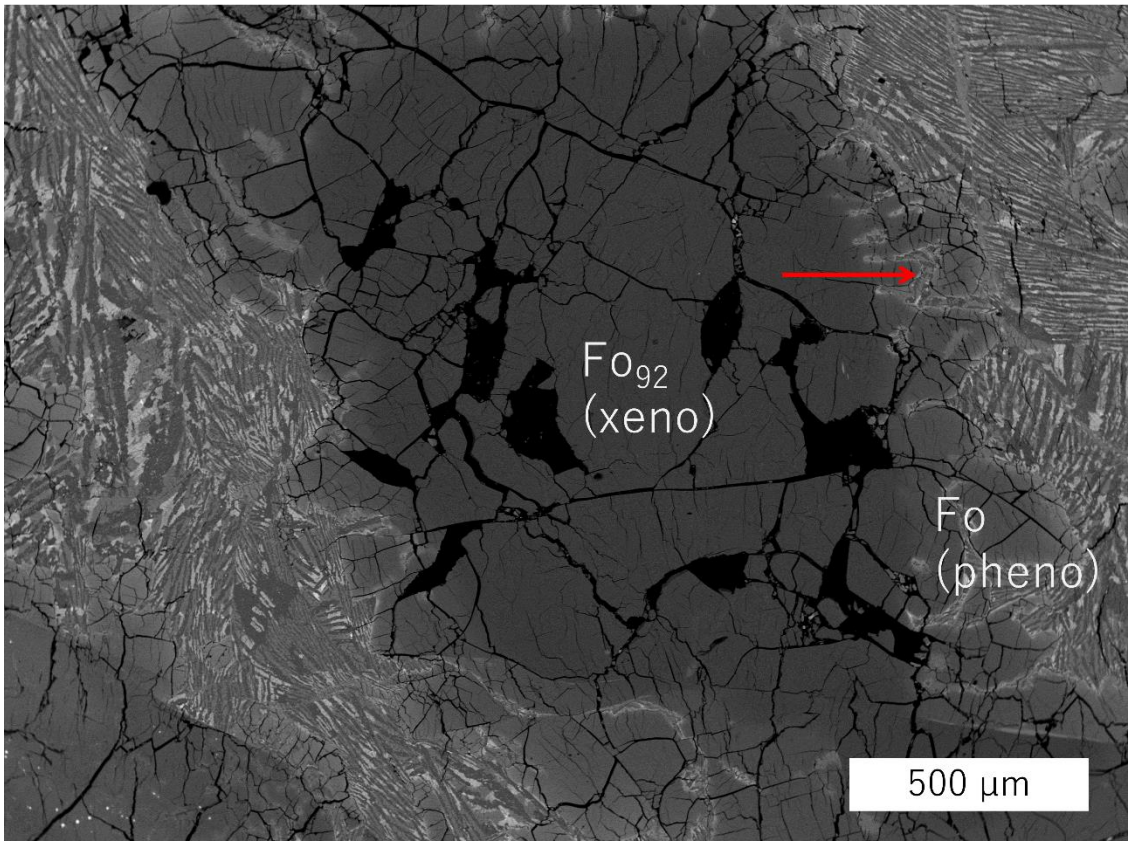

Fig. 24. Olivine xenocryst in NWA 1670. This olivine xenocryst exists in the red square of Fig. 25. Line profiles of red arrow part are shown in Fig. 26. The area of line profile is chosen where cracks are mostly absent. The boundary between xenocrystic core and overgrowth corresponds to dark gray and gray areas of BSE image.

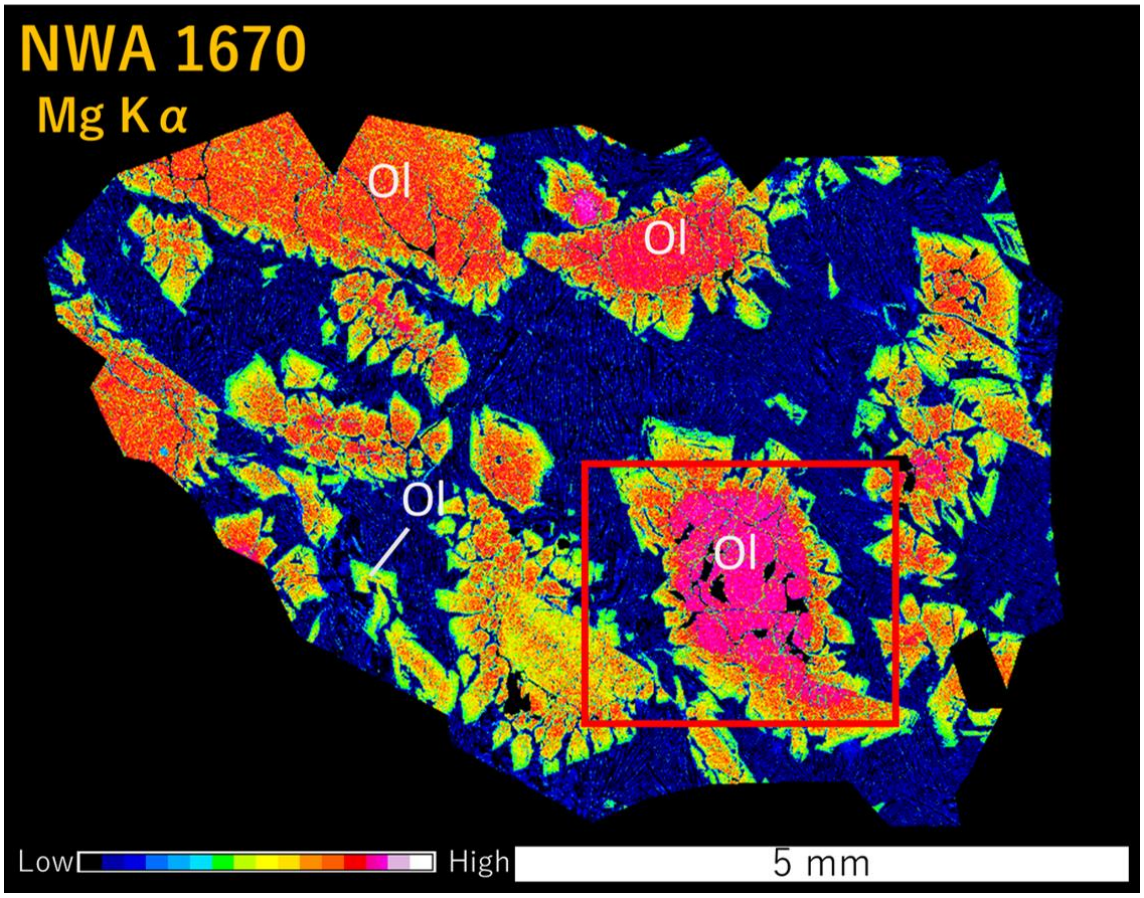

Fig. 25. Mg X-ray map of NWA 1670. Warm color indicates the high concentration of Mg. BSE image of olivine in red square is shown in Fig. 24.

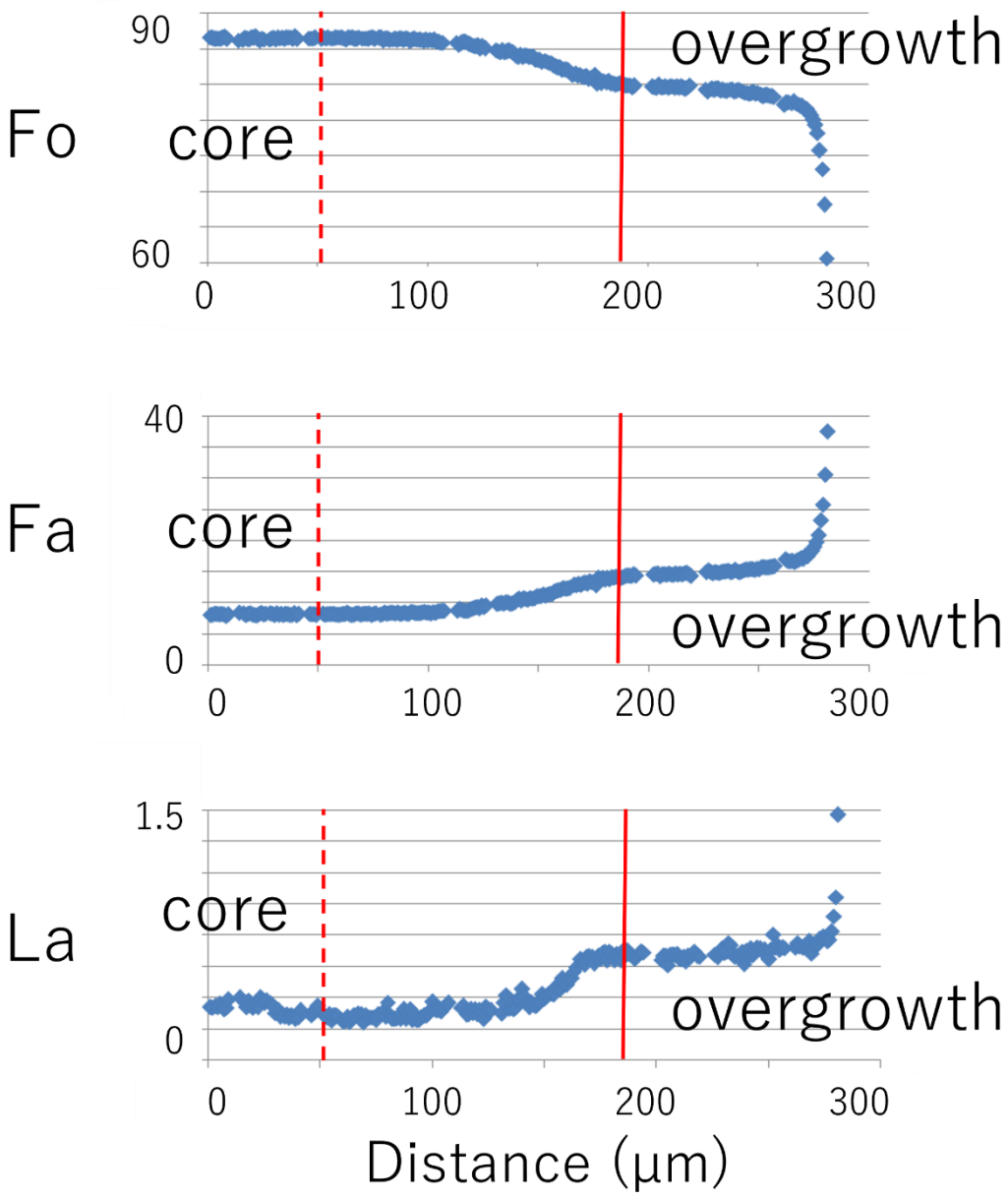

Fig. 26. Line profiles of olivine xenocryst in NWA 1670 (red arrow part of Fig. 24). Red solid line corresponds to the boundary of olivine xenocryst and overgrowth assumed from the La profile. Red dotted line corresponds to the homogeneous core of olivine xenocryst assumed from the Fa profile.

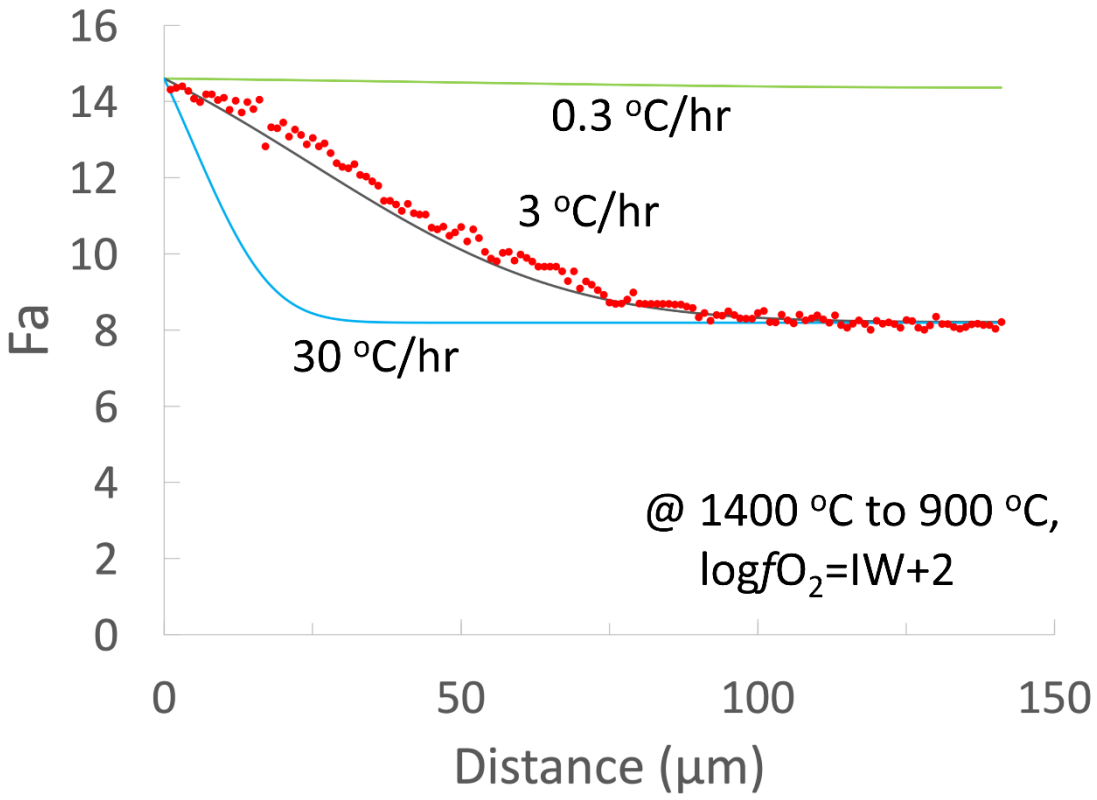

Fig. 27. Estimation for cooling rate of NWA 1670. Cooling rate is estimated at the enclosed area with red solid line and red dotted line shown in Fig. 26. The best-fit cooling rate is 3 °C/hr. Cooling rates of 0.3 °C/hr and 30 °C/hr are also shown for comparison.

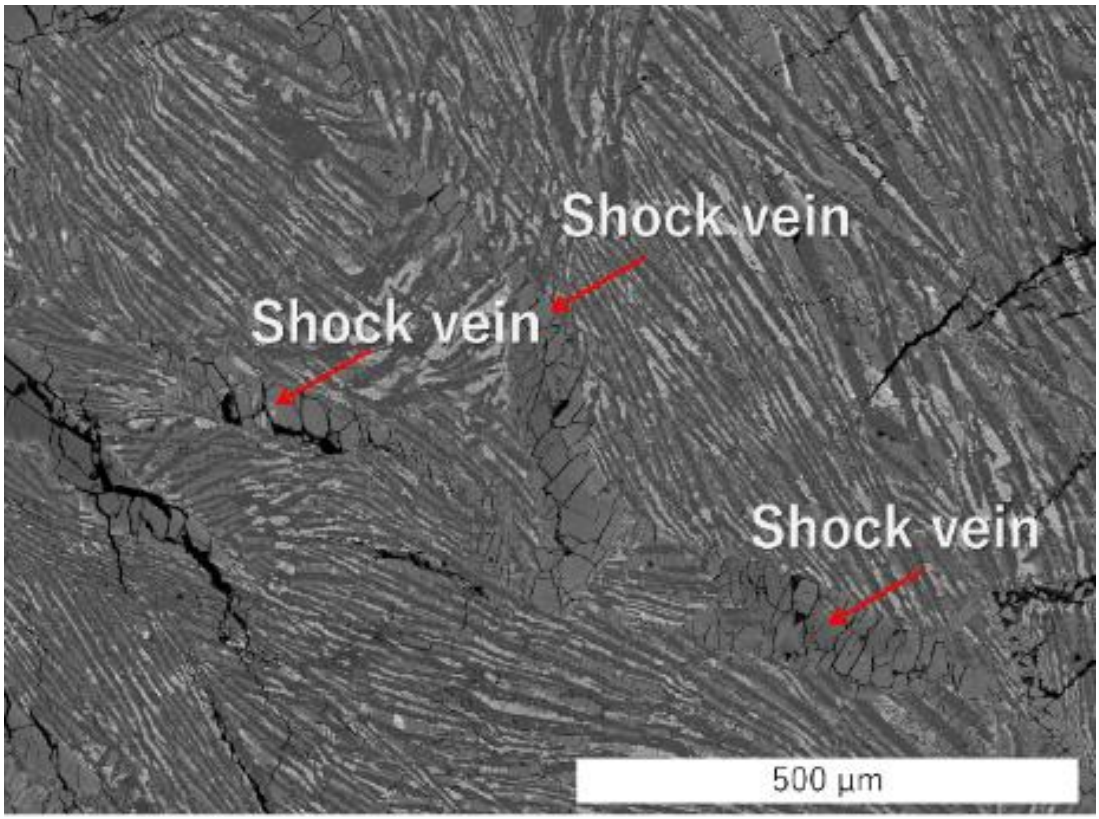

Fig. 28. BSE image of glassy shock melt veins in NWA 1670.

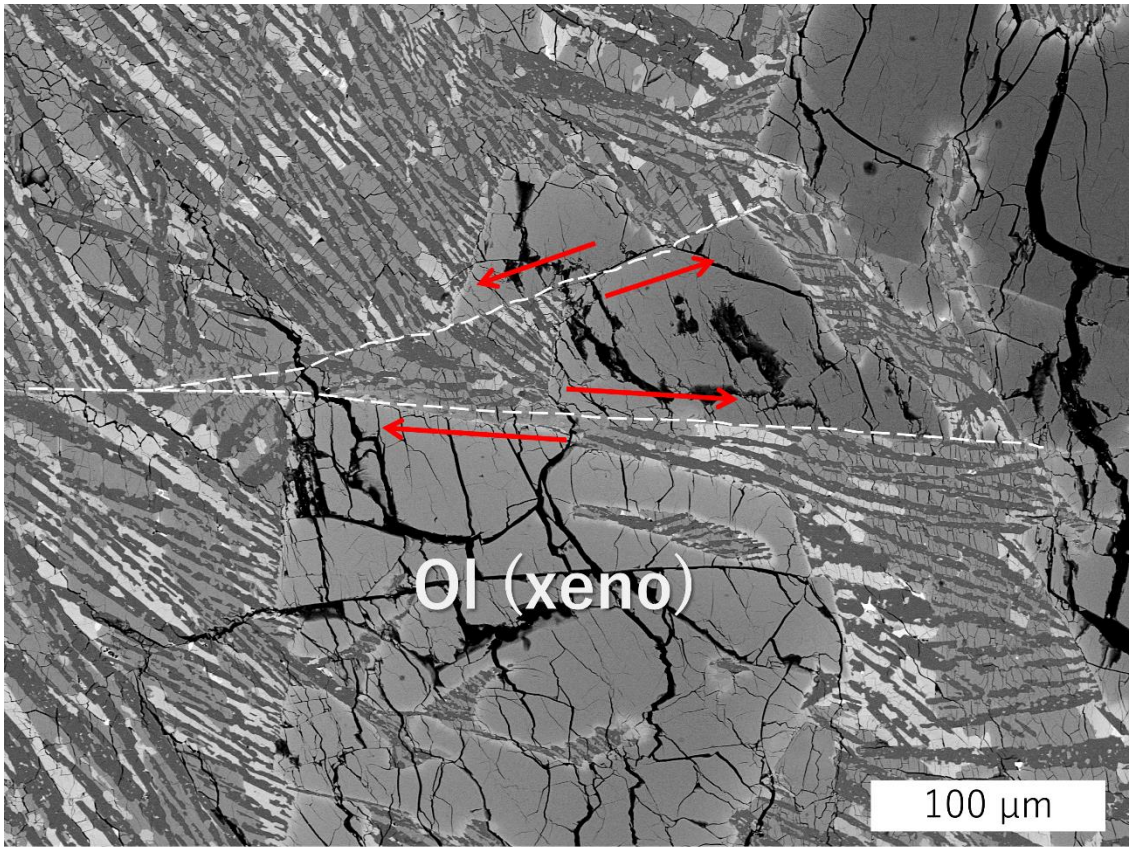

Fig. 29. BSE image showing ~100 μm displacement of the original igneous texture in NWA 1670 presumably caused by shock. The upper fault ends at the part that hits another fault.

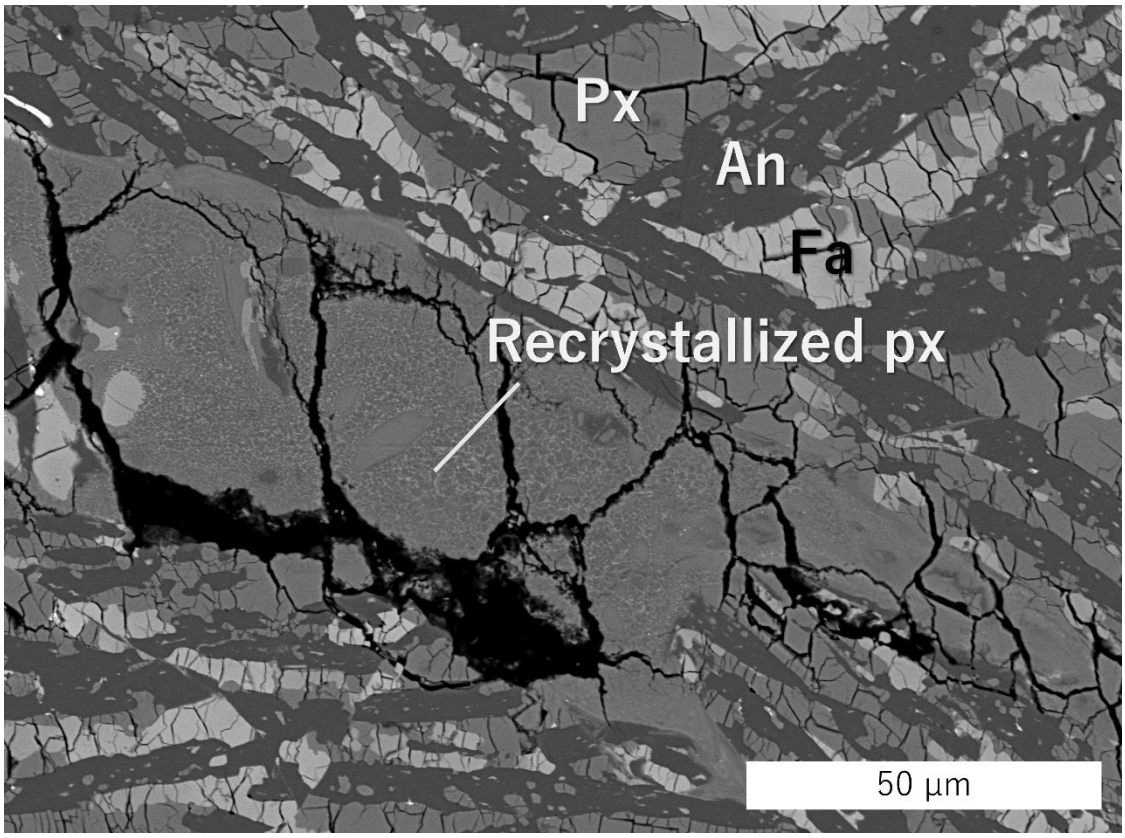

Fig. 30. BSE image of recrystallized clinopyroxene from glassy shock vein.

3.1.5. NWA 7203

（非公開部分）

（非公開部分）

（非公開部分）

（非公開部分）

（非公開部分）

（非公開部分）

（非公開部分）

（非公開部分）

（非公開部分）

（非公開部分）

（非公開部分）

（非公開部分）

（非公開部分）

（非公開部分）

（非公開部分）

（非公開部分）

（非公開部分）

（非公開部分）

（非公開部分）

（非公開部分）

（非公開部分）

（非公開部分）

（非公開部分）

（非公開部分）

（非公開部分）

（非公開部分）

（非公開部分）

（非公開部分）

（非公開部分）

（非公開部分）

3.1.6. NWA 12774

NWA 12774 has a porphyritic texture with relatively large olivine and clinopyroxene phenocrysts (~1 mm) set in the fine-grained ophitic groundmass (Fig. 52). NWA 12774 mainly consists of olivine, clinopyroxene, anorthite and accessory phases such as Al-rich spinel, native iron and troilite. Chemical compositions of the constituent minerals are listed in Table 6.

I performed 21 × 28 point grid analysis once for NWA 12774 with FE-EPMA to obtain its bulk composition. The bulk composition of NWA 12774 is estimated to be SiO_2= 40.1 wt.%, Al_2O_3= 12.8 wt.%, TiO_2= 0.55 wt.%, FeO= 17.6 wt.%, MnO= 0.19 wt.%, MgO= 18.5 wt.%, CaO= 11.0 wt.%, Cr_2O_3= 0.45 wt.%.

Olivine occurs as large phenocrysts (around 1 mm) or as micro-phenocrysts in the groundmass. Large olivine phenocrysts are euhedral to subhedral and they show sharp extinction under optical microscope. Some large olivine grains show several different extinction angles in part. As getting closer to the boundary to the part with the different extinction angle, chemical composition changes more Fe-rich. The core part of large olivine grains in the thin section is $Fo_{92}Fa_8La_0$ ~ $Fo_{58}Fa_{41}La_1$. All large olivine phenocrysts show extensive chemical zoning. The edge composition of the large olivine phenocryst is $Fo_{40}Fa_{58}La_2$ ~ $Fo_{17}Fa_{75}La_8$. Kirschsteinite is rare and chemical composition is $Fo_7Fa_{61}La_{32}$. Olivine micro-phenocrysts in the matrix are $Fo_{52}Fa_{46}La_2$ ~ $Fo_{15}Fa_{81}La_4$. Chemical composition of olivine in NWA 12774 is shown in Fig. 53. Some large olivine grains (~3 mm) are Mg-rich compared to other large olivine grains, and the most Mg-rich olivine grain is Fo_{92} (Fig. 54). These Mg-rich olivines are xenocrysts judged by the bulk chemical composition of NWA 12744 obtained from the EPMA grid analysis (see 3.3.). Fig. 55 shows a Mg X-ray map of NWA 12774. From the Mg X-ray map, olivine xenocrysts are shown in orange ~ red color. I measured EPMA line profiles of olivine xenocryst to estimate a cooling rate of this angrite (Fig. 56, red arrow part of Fig. 54). Line profiles of Fo, Fa and La contents are shown in Fig. 56. I estimate the cooling rates by

calculating atomic diffusion profiles from 1400 °C to 900 °C linearly at logfO_2=IW+2 at the enclosed area with red solid and dotted lines shown in Fig. 56. The method to estimate the cooling rate is the same manner to other xenocryst-bearing quenched angrites (3.1.1). The obtained cooling rate of NWA 12774 is 3.5 °C/hr (Fig. 57). It is considered that 3.5 °C/hr cooling rate of NWA 12774 is not essentially different from the 3 °C/hr cooling rate of NWA 1670 (Fig. 27) although the value can slightly change because of the orientation of olivine.

Clinopyroxene is also present as euhedral large phenocrysts (~1 mm) or as micro-phenocrysts in the matrix. Large clinopyroxene phenocrysts show both high-Al and low-Al parts in one grain, characteristics of sector zoning. Large clinopyroxene contains high Ti (TiO_2 = 1-2 wt%) and is remarkably enriched in Al (Al_2O_3 = 10-12 wt%, 16-18 wt%), and their chemical composition of the high-Al part is $Di_{12}Hd_{37}Ksh_{35}Tp_3En_{13}$ ~ $Di_{23}Hd_{27}Ksh_{36}Tp_4En_{10}$ (Di=$CaMgSi_2O_6$, Hd=$CaFeSi_2O_6$, Ksh=$CaAlAlSiO_6$, Tp=$CaTiAl_2O_6$, and En=$Mg_2Si_2O_6$), and thus some parts of the clinopyroxene are kushiroite (Fig. 58). Clinopyroxene micro-phenocrysts occurring in the matrix contain TiO_2 = 1-2 wt% and Al_2O_3 = 4-6 wt%.

Anorthites show lath textures, and their grain sizes are up to 1 mm in length and 10 μm in width. Their chemical composition is almost pure anorthite ($An_{>99.5}$). Spinel occurs associated with large olivine grains. The size is up to 200 μm, and their chemical composition is ($Fe_{0.49-0.56}$, $Mg_{0.51-0.44}$)($Al_{0.81-0.93}$, $Cr_{0.19-0.07}$)O_4. Spinel close to large olivine phenocrysts is more Fe-poor and Cr-rich. There are also small ulvöspinel grains in the groundmass. The grain size of ulvöspinel is around 10 μm. Native iron (up to 100 μm) occurs in large olivine phenocrysts. Troilite occurs between anorthite laths. The grain size is up to 100 μm, but most grains are around 10 μm.

Table 6. Chemical compositions of the constituent minerals in NWA 12774.

	Ol (Xeno)	Ol (Micro-pheno)	Px (Large)	An (Micro-pheno)
SiO_2	41.58	30.76	41.31	43.99
Al_2O_3	0.04	0.26	17.83	34.89
TiO_2	*b.d.*	0.09	1.51	0.19
FeO	7.35	60.40	8.46	1.83
MnO	0.09	0.78	0.12	0.05
MgO	51.06	4.39	7.76	0.27
CaO	0.23	1.78	22.15	19.91
Na_2O	*b.d.*	0.13	*b.d.*	0.04
K_2O	0.02	*b.d.*	*b.d.*	*b.d.*
Cr_2O_3	0.25	0.02	0.45	0.01
Total	100.62	98.61	99.59	101.19

b.d.: Below detection limit. Detection limits are about 100 ppm for each element.

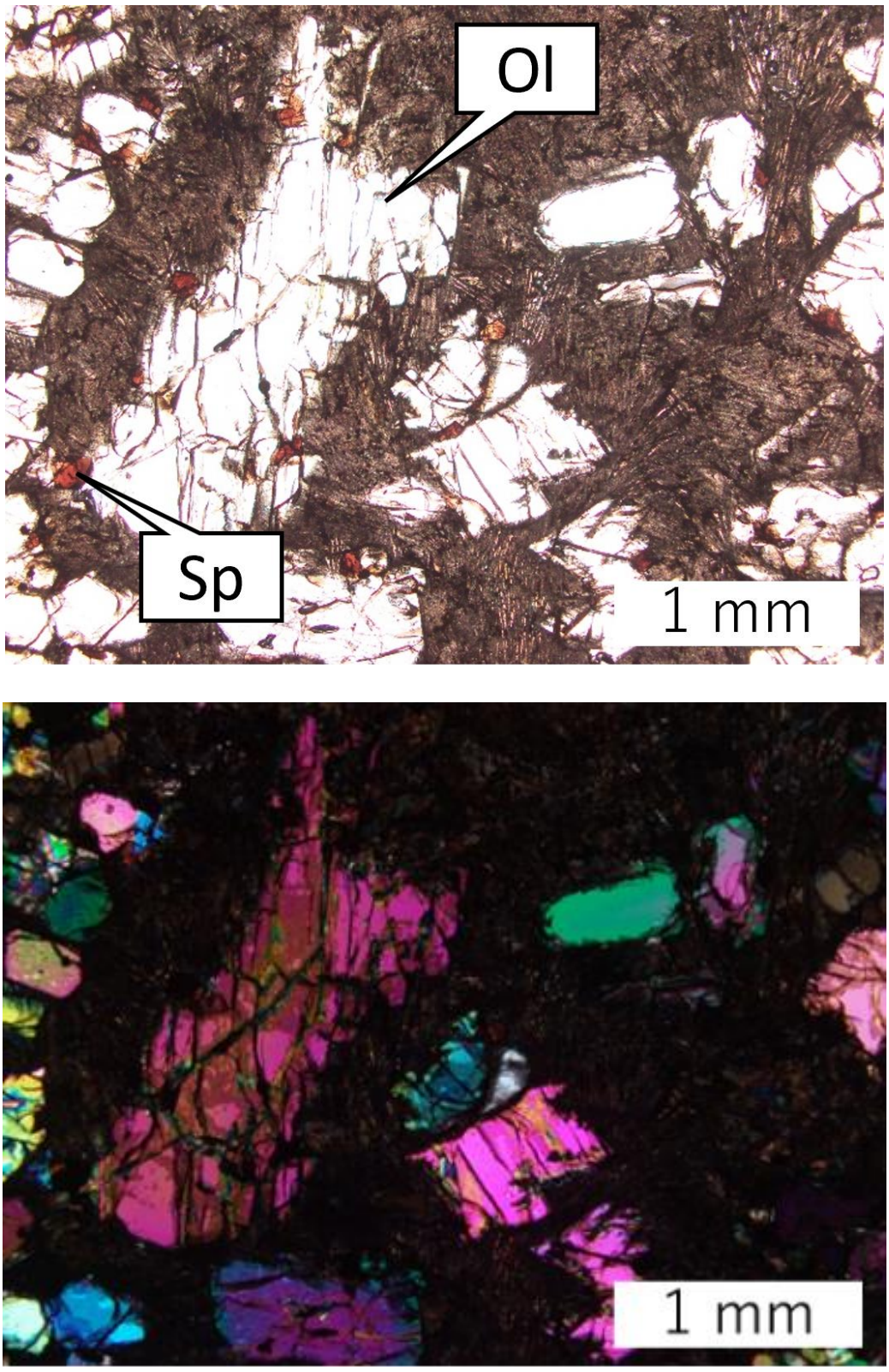

Fig. 52. Open nicol (upper) and Crossed nicols (lower) of optical photomicrograph of NWA 12774.

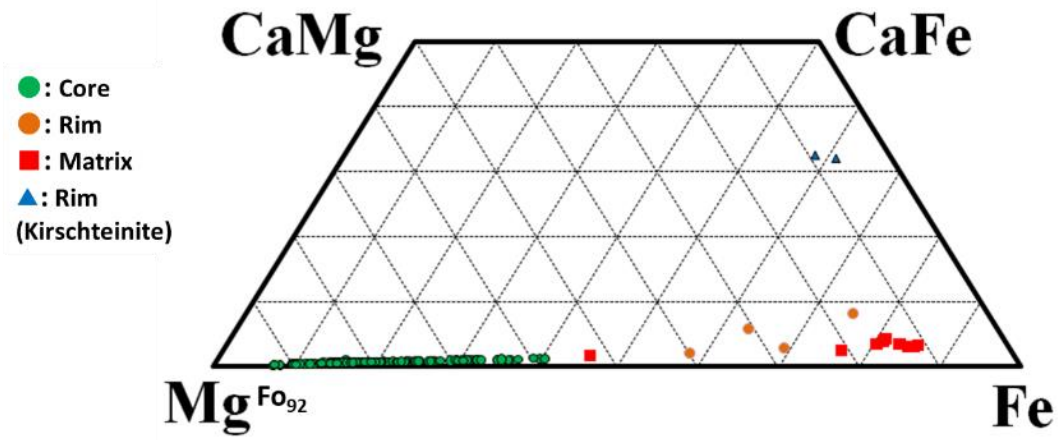

Fig. 53. Chemical composition of olivine in NWA 12774.

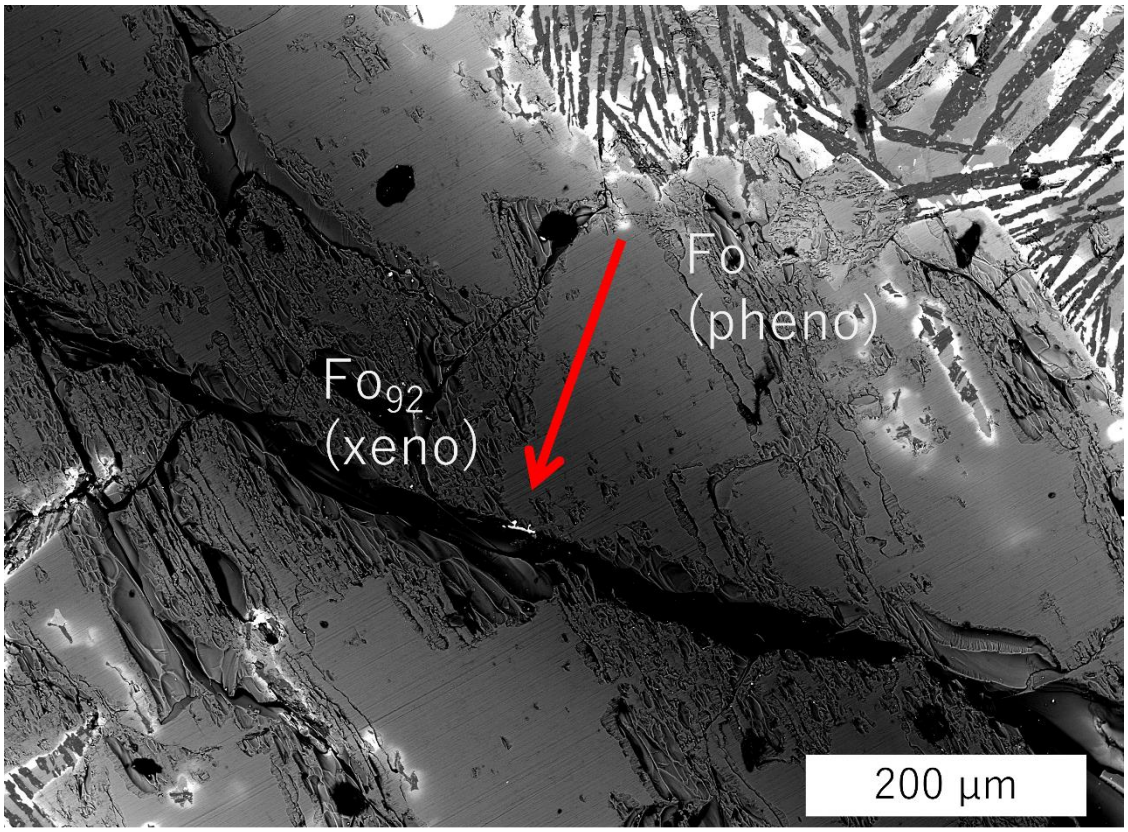

Fig. 54. Olivine xenocryst in NWA 12774. This olivine xenocryst exists in the red solid square of Fig. 55. Line profiles of red arrow part is shown in Fig. 56. The area of line profile is chosen where cracks are mostly absent, and this is the only place without cracks in the studied slice. The boundary between xenocrystic core and overgrowth corresponds to dark gray and gray areas of the BSE image.

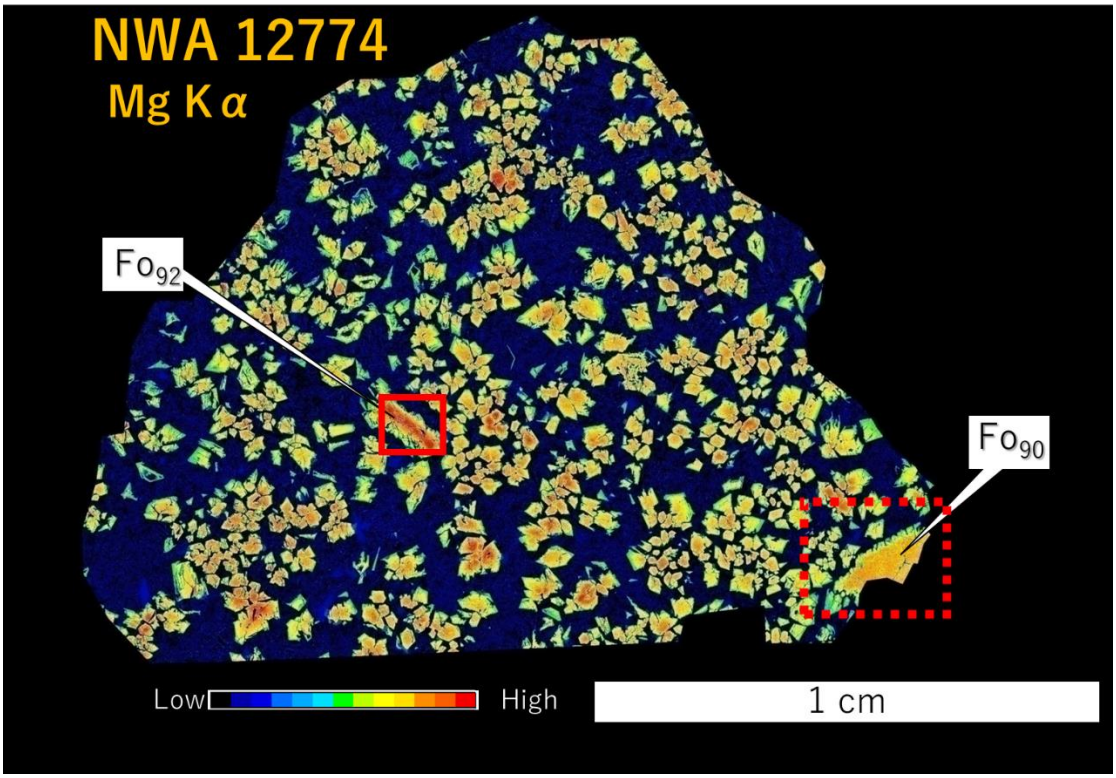

Fig. 55. Mg X-ray map of NWA 12774. Warm color indicates the high concentration of Mg. BSE image of olivine in red solid square is shown in Fig. 54. Oxygen isotopic ratio of olivine xenocryst in NWA 12774 was analyzed from the grain inside of red dotted squares (Table 8 and Fig. 68, see 3.5.).

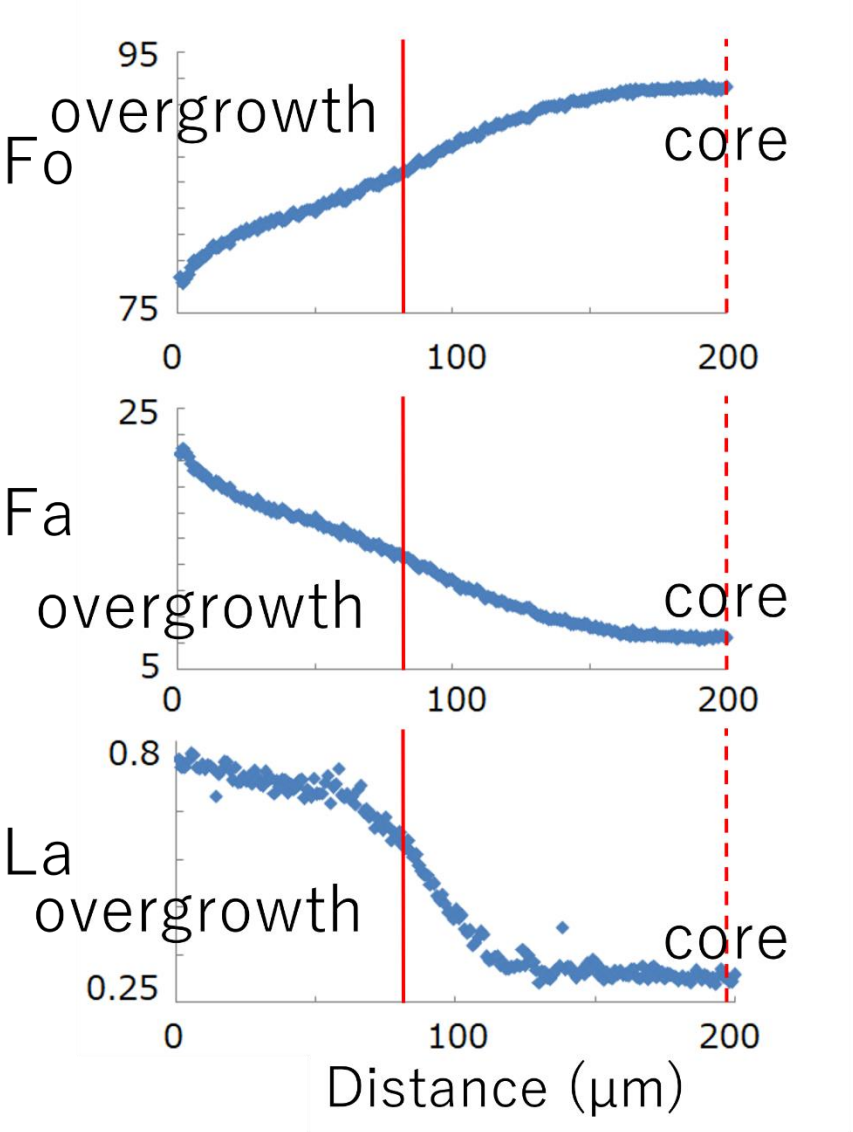

Fig. 56. Line profiles of olivine xenocryst in NWA 12774 (red arrow part of Fig. 54). Red solid line corresponds to the boundary of olivine xenocryst and overgrowth assumed from the La profile. Red dotted line corresponds to the homogeneous core of olivine xenocryst assumed from the Fa profile.

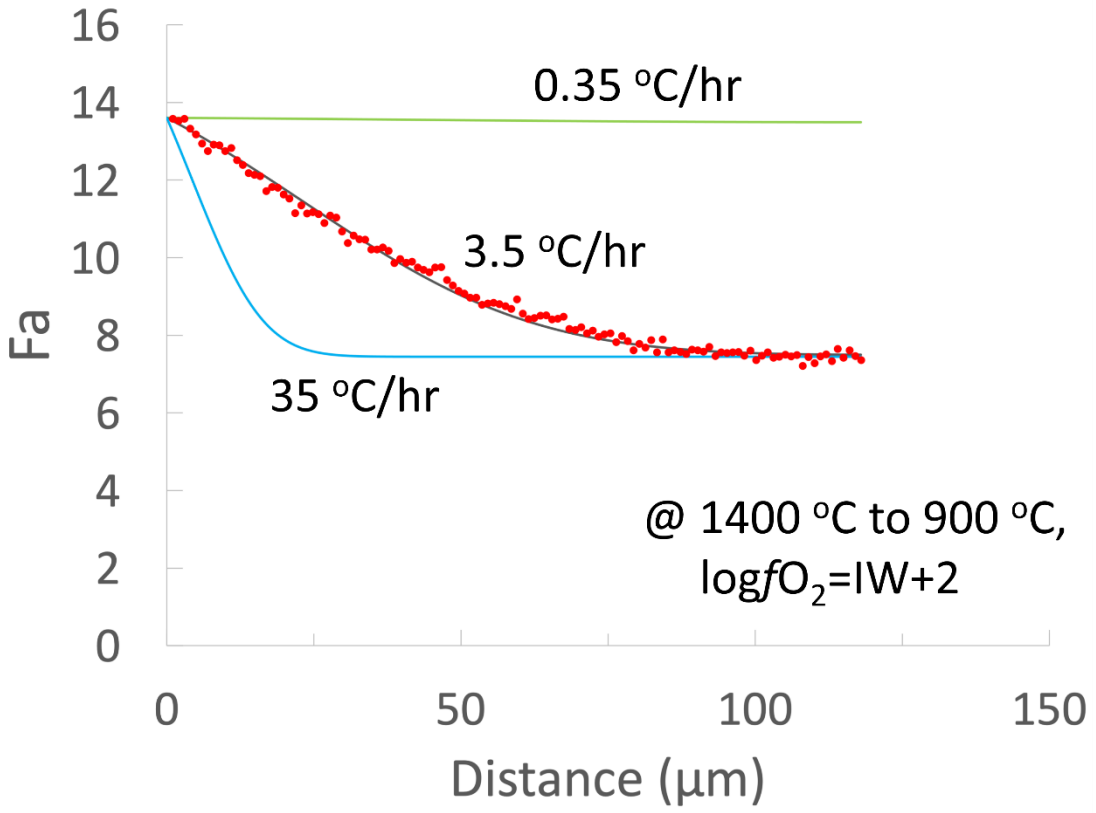

Fig. 57. Estimation for cooling rate of NWA 12774. Cooling rate is estimated at the enclosed area with red solid line and red dotted line shown in Fig. 56. The best-fit cooling rate is 3.5 °C/hr. Cooling rates of 0.35 °C/hr and 35 °C/hr are also shown for comparison.

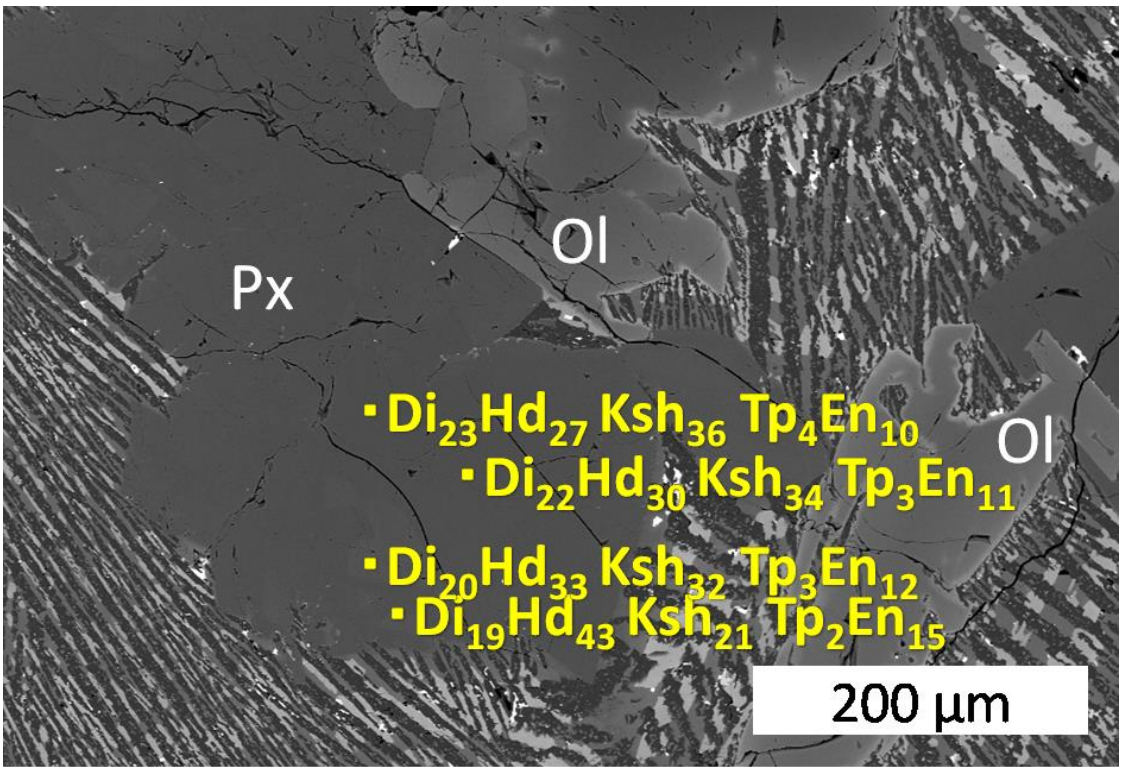

Fig. 58. BSE image of a large clinopyroxene grain in NWA 12774. Chemical composition of clinopyroxene is shown in the figure.

3.2. Textures of quenched angrites

In the previous section (3.1.), I described igneous textures of quenched angrites. This study reveals that the igneous textures of quenched angrites can be divided into three groups: dendritic, relatively coarse-grained and anorthite spinifex (Fig. 59). NWA 7203 shows a dendritic texture in the coarse-grained lithology. The fine-grained lithology of NWA 7203 contains elongated anorthites. This is not similar to NWA 1670, NWA 12774 and LEW 87051 in terms of grain length and cooling rates, but rather similar to the dendritic sample of NWA 1296 (detailed discussion is found in 4.2.). Thus, the fine-grained lithology of NWA 7203 is essentially related to dendritic samples. NWA 7203 (coarse-grained lithology), Sahara 99555, D'Orbigny and Asuka-881371 show relatively coarse-grained textures. NWA 7203 (coarse-grained lithology) and Sahara 99555 also contain dendritic intergrowth, but the overall texture is more similar to a relatively coarse-grained texture than a dendritic texture. Dendritic intergrowth found in NWA 7203 (coarse-grained lithology) and Sahara 99555 might be caused by its characteristic bulk chemical compositions close to the olivine-anorthite eutectic composition, or by relatively rapid cooling rates. NWA 1670 and NWA 12774 exhibit an anorthite spinifex texture. In all textures, olivine, pyroxene and anorthite are the main constituent minerals. Here I add NWA 1296, LEW 87051 and NWA 8535 in Fig. 59. NWA 1296 shows a clear dendritic texture (Jambon et al., 2005) and LEW 87051 has an anorthite spinifex texture (Mikouchi et al., 1996). NWA 8535 is the only dunite angrite known until now (Santos et al, 2016a), and this angrite may be a cumulate. In the quenched angrites, D'Orbigny, Asuka-881371, NWA 1670, LEW 87051 and NWA 12774 contain Mg-rich olivine xenocrysts.

NWA 12774 is most similar to NWA 1670 and LEW 87051 in texture. However, the texture of NWA 12774 is slightly different from NWA 1670. Olivine xenocrysts are abundant in NWA 1670 and display mosaicism or undulose extinction (Mikouchi et al., 2003). Spinel occurs only in olivine xenocryst (Jambon et al., 2008), and pyroxene xenocrysts of NWA 1670 are rare and small (around

100 μm) although they are Al-rich (Jambon et al., 2008). NWA 12774 is also slightly different from LEW 87051. NWA 12774 pyroxenes contain 10-18 wt% of Al_2O_3, but LEW 87051 pyroxenes contain only 4-6 wt% of Al_2O_3 (McKay et al., 1990). Also, the grain size of groundmass minerals in LEW 87051 is larger than those of NWA 12774. In addition, spinel in NWA 12774 is unusually large compared to other quenched angrites except for NWA 8535 (Santos et al., 2016b). Thus, NWA 12774 is not paired with either NWA 1670 or LEW 87051, but they are closely related in petrogenesis because all of them contain similar olivine xenocrysts.

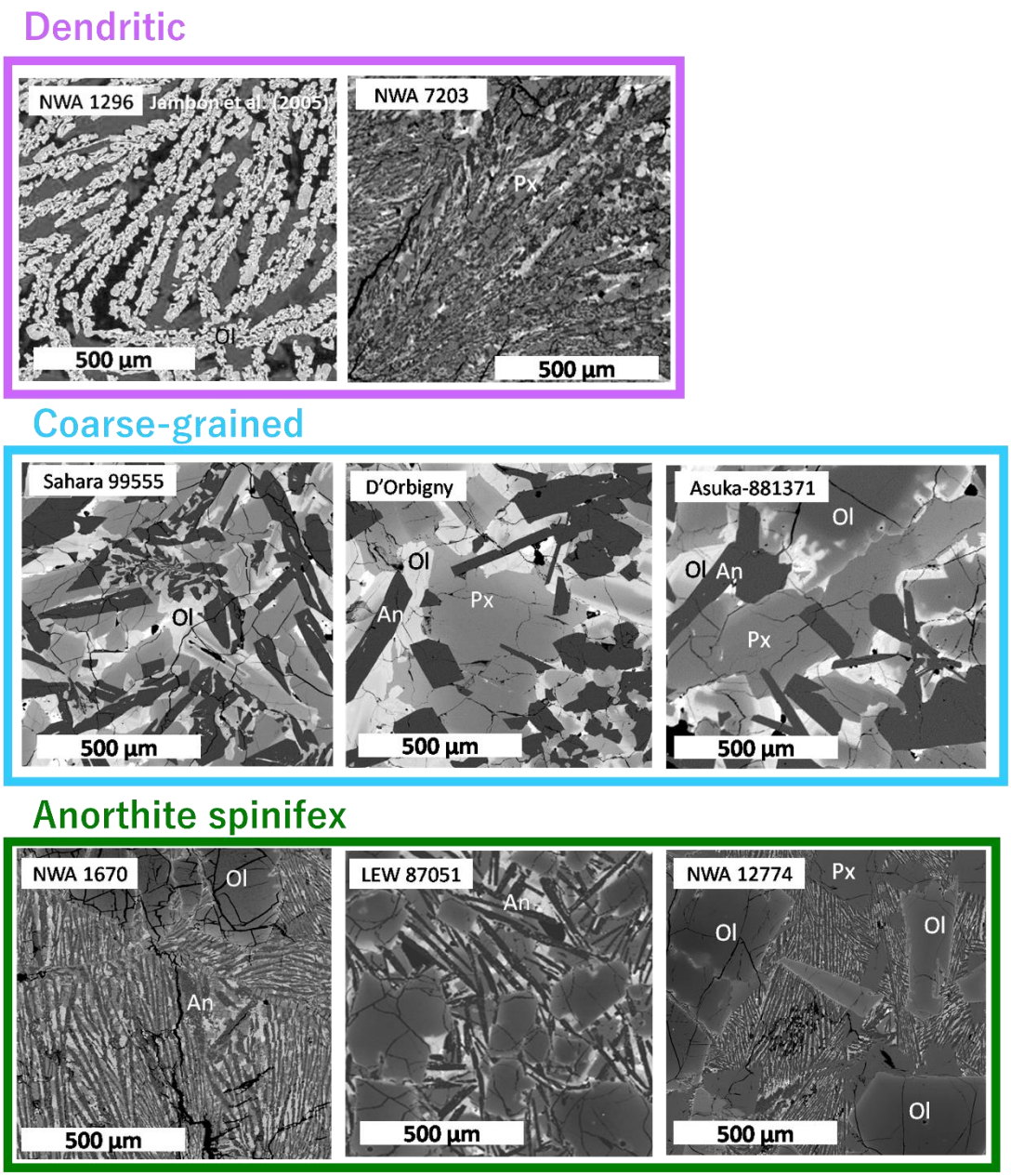

Fig. 59. BSE images of igneous textures of quenched angrites. The igneous textures of quenched angrites can be divided into three groups: dendritic (NWA 1296 and NWA 7203), relatively coarse-grained (Sahara 99555, D'Orbigny, and Asuka-881371) and anorthite spinifex (NWA 1670, LEW 87051, and NWA 12774). The BSE image of NWA 1296 taken from Jambon et al. (2005).

3.3. Bulk chemical compositions of quenched angrites

Bulk chemical compositions of several quenched angrites have been reported in previous studies (e.g., Mittlefehldt et al., 2002; Mittlefehldt and Lindstrom, 1990). In addition, bulk chemical compositions of NWA 7203 and NWA 12774 are obtained from EPMA grid analyses in this study (see 3.1.5. and 3.1.6.). In Table 7, bulk chemical compositions of these quenched angrites are summarized. From the distribution coefficient of $K_D = \frac{(X_{FeO}^{Ol})}{(X_{FeO}^{Liq})}\frac{(X_{MgO}^{Liq})}{(X_{MgO}^{Ol})} = \sim 0.30$ between melt and olivine (Roeder and Emslie, 1970), I can estimate Fo# of olivine crystallizing from these angritic melts, if I assume that these bulk compositions are equal to melt compositions of each quenched angrite. The estimated Fo# of olivine crystallized from each angritic melt is Fo_{61} in NWA 1296, Fo_{66} in NWA 7203, Fo_{64} in Sahara 99555, Fo_{61} in D'Orbigny, Fo_{79} in Asuka-881371, Fo_{86} in LEW 87051, Fo_{82} in NWA 1670 and Fo_{86} in NWA 12774, respectively.

However, Filiberto and Dasgupta (2011) considered that K_D = 0.35 $\pm$ 0.01 is more appropriate for Fe-rich Martian basalt. Angritic basalt is also Fe-rich, and when I employ K_D = 0.35, the estimated Fo# of olivine crystallized from each angritic melt is Fo_{58} in NWA 1296, Fo_{60} in NWA 7203, Fo_{61} in Sahara 99555, Fo_{57} in D'Orbigny, Fo_{76} in Asuka-881371, Fo_{84} in LEW 87051, Fo_{80} in NWA 1670 and Fo_{84} in NWA 12774, respectively.

Note that these values are approximation because Fo# of olivine crystallized from melt should be strictly estimated from a real melt composition. Such a real melt composition is difficult to estimate only from modal abundance of olivine xenocryst because it is difficult to distinguish olivine xenocrysts and overgrowth. In addition, depending on literature distribution coefficient values used, Fo# can include an error of about 10%.

Table 7. Bulk chemical compositions of angrites (all in wt%).

		SiO_2	TiO_2	Al_2O_3	Cr_2O_3	FeO	MnO	MgO	CaO	Total
Quenched angrites	NWA 1296 [1]	39	0.93	12.18	0.068	25.0	0.28	6.71	14.65	100
	NWA 7203 (fine)	40.4	0.89	22.0	0.07	22.0		6.3	15.5	100.4
	NWA 7203 (coarse)	40.6	0.7	14.7	0.08	21.9		7.7	14.6	100.6
	Sahara 99555 [2]	38.6	0.91	12.5	0.046	23.1	0.26	7.04	15.1	97.72
	D'Orbigny [2]	38.4	0.89	12.4	0.042	24.7	0.28	6.49	15.0	98.38
	Asuka-881371 [3]	37.3	0.88	10.07	0.13	23.43	0.2	14.81	12.51	100.77
	LEW 87051 [4]	40.4	0.73	9.19	0.17	19.0	0.24	19.4	10.8	100.0
	NWA 1670 [5]	42.2	0.67	11.7	0.14	18.52	0.22	14.6	11.95	100.14
	NWA 12774	40.1	0.55	12.8	0.45	17.6	0.19	18.5	11.0	101.1
Slowly-cooled Angrites	ADoR [4]	43.7	2.05	9.35	0.21	9.4	0.1	10.8	22.9	98.7
	LEW 86010 [4]	39.6	1.15	14.1	0.11	18.5	0.2	7.0	17.5	98.3
	NWA 2999 [6]	33.4	0.42	4.71		31.2	0.24	19.0	7.37	96.34
	NWA 4590 [7]	37.49	1.46	8.5		27.16	0.31	17.84	6.8	100.03

References: [1] Jambon et al. (2005), ICP-AES; [2] Mittlefehldt et al. (2002), EPMA and INAA; [3] Yanai (1994), EPMA; [4] Mittlefehldt and Lindstrom (1990), EPMA; [5] Jambon et al. (2008), ICP-AES; [6] Gellissen et al. (2007), XRF and INAA; [7] Shirai et al. (2009), analysis of the fusion clast.

3.4. Olivine compositions of quenched angrites

I performed quantitative measurement of minor elements in olivine for quenched angrites. The analytical conditions were shown in 2.2.3. I found that olivines in quenched angrites exhibit characteristic trends in minor element contents. I focus on Cr_2O_3 and CaO content on olivine xenocrysts, because olivine xenocrysts have characteristic Cr_2O_3 and CaO contents and also because diffusion coefficients of these elements are small and thus, they retain original information. Fig. 60 shows Fo# vs Cr_2O_3 contents in olivines for each quenched sample. Olivine phenocrysts are enclosed in light colors and olivine xenocrysts are enclosed in dense colors. Olivine xenocrysts are found in NWA 12774, NWA 1670, Asuka-881371 and D'Orbigny as shown in the previous section. NWA 7203 and Sahara 99555 do not contain olivine xenocrysts. In Fig. 60, it is obvious that olivine phenocrysts (shown in light colors) are Cr-poor for each sample and olivine xenocrysts (shown in dense colors) contain relatively higher Cr contents. In most cases, Cr contents of olivine xenocrysts are higher compared to olivine phenocrysts. Olivine xenocrysts in Asuka-881371 (and maybe D'Orbigny) show variety of Cr contents. On the other hand, olivine xenocrysts in NWA 12774 and NWA 1670 show different trends. As Fo# of olivine xenocrysts increase, Cr contents also increase. This trend might reflect the environment of crystallization of olivine xenocrysts.

Fig. 61 shows Fo# *vs.* CaO contents in olivines for each quenched sample. The phase equilibrium relationships of Ca-Mg-Fe olivine (at 800~1000 ℃) are reported by Davidson and Mukhopadhyay (1984) and can be used to understand the olivine compositional variation of quenched angrites (Fig. 39). In Fig. 61, olivine compositional trends of NWA 1670 and NWA 12774 whose Fo contents are below Fo_{85} plot along the phase equilibrium relationships of Ca-Mg-Fe (Fig. 39). Olivine xenocrysts in Asuka-881371 and D'Orbigny show variable of Ca contents, which are different from the phase equilibrium relationships of Ca-Mg-Fe olivine. This trend is the same for Cr. On the other hand, olivine xenocrysts in Asuka-881371 and D'Orbigny show relatively similar trends plotted for the

equilibrium relationships of Ca-Mg-Fe olivine. The most Mg-rich (Fo_{96}) olivine xenocryst in NWA 1670 has low Cr and Ca contents compared with other olivine xenocrysts in NWA 1670. The chemical compositional trend of this olivine xenocryst might be similar to those of Asuka-881371 and D'Orbigny.

From Fig. 60, I can identify Fo# of the most Mg-rich olivine phenocryst in each quenched angrite. NWA 7203 and Sahara 99555 do not contain olivine xenocrysts, and thus the most Mg-rich olivine is the most Mg-rich olivine phenocryst. The most Mg-rich olivine phenocrysts are Fo_{64} for both NWA 7203 and Sahara 99555. Asuka-881371 and D'Orbigny contain Mg-rich olivine xenocrysts, but the chemical compositions have a large gap between olivine xenocryst and phenocryst. Thus, it is easy to distinguish olivine xenocryst and phenocryst. The most Mg-rich olivine phenocrysts in D'Orbigny and Asuka-881371 are Fo_{65} and Fo_{72}, respectively.

It is difficult to determine the most Mg-rich olivine phenocrysts in NWA 12774 and NWA 1670, because olivine phenocryst is also Mg-rich and the chemical composition is similar to xenocryst. I calculated the most Mg-rich olivine phenocryst in NWA 12774 as Fo_{86} and that of NWA 1670 as Fo_{82} from the bulk chemical compositions with the distribution coefficient of Fe-Mg in olivine of 0.30 (Roeder and Emslie, 1970) or those in NWA 12774 as Fo_{84} and in NWA 1670 as Fo_{80} with the distribution coefficient of 0.35 (Filiberto and Dasgupta, 2011) (see 3.3.). However, the bulk compositions contain contributions of olivine xenocrysts. If I try to deduct the contribution of olivine xenocryst, the theory will circulate. Thus, it is needed to estimate the Fo# of most Mg-rich olivine phenocrysts of NWA 12774 and NWA 1670 from another way.

Fig. 62 shows the Cr_2O_3 *vs.* CaO contents in olivines for four EPMA line profiles of olivines in NWA 12774. The Cr_2O_3 content is high in the core and decreases towards the rim, but increases once again at the overgrowth. This trend is similar to olivines in LEW 87051 (Mikouchi et al., 1996). Fig. 63 shows the Cr_2O_3 *vs.* CaO contents and Fo# of the core for olivine grains in NWA 12774. Olivine

can be divided in three types (Ⓐ, Ⓑ, and Ⓒ, see Fig. 62) according to the Cr_2O_3 *vs.* CaO contents in olivines. Olivines which show the Ⓒ chemical compositions in Fig. 62 are their rim parts and they also have Fe-rich ($Fo_{\leqq\sim70}$) compositions (Fig. 63). Thus, Ⓒ is phenocryst. Ⓐ and Ⓑ show different trends in the CaO-Cr_2O_3 compositional systematics (Fig. 62). Ⓐ is relatively rare and Ⓑ is more common. Also, Ⓐ olivines show Mg-rich ($Fo_{\geqq\sim84}$) composition while Ⓑ olivines show $Fo_{\sim70}$ ~ $Fo_{\sim84}$ (Fig. 63). In Fig. 62, all grains show two trends with both positive and negative slopes. The core part is Ca-poor and gradually becomes Ca-rich as getting closer to the rim. All olivine grains go to around CaO = 0.5 wt.% and Cr_2O_3 = 0.17 wt.%, that may imply that the first crystallization of olivine phenocryst overgrowth. In this case, Ⓑ is considered to be a phenocryst. Ⓐ is Mg-rich ($Fo_{\geqq\sim84}$) and has a different trend in the CaO-Cr_2O_3 compositional systematic from Ⓑ, suggesting that the crystallization environment of Ⓐ is different from that of Ⓑ. Thus, I concluded Ⓐ as a xenocryst. This is also confirmed by Fo# vs Cr_2O_3 contents in olivines for NWA 12774 (Fig. 60). In conclusion, the most Mg-rich olivine phenocryst in NWA 12774 is Fo_{84}. This value is close to the most Mg-rich Fo# (Fo_{86} or Fo_{84}) calculated from bulk chemical composition of NWA 12774 (see 3.3.).

Olivine in NWA 1670 has similar trends to that in NWA 12774. Thus, I can infer its most Mg-rich olivine phenocryst in a similar manner to NWA 12774. From Fo# vs Cr_2O_3 contents in olivines for NWA 1670 (Fig. 60), the most Mg-rich olivine phenocryst in NWA 1670 is around Fo_{85}. In the case of NWA 1670, Fe-rich (Fo_{77}) olivine xenocryst exists (Fig. 64). EPMA line profiles of this olivine xenocryst are shown in Fig. 65 (red arrow part of Fig. 64). Line profiles of Fo, Fa, La and Cr_2O_3 contents are shown in Fig. 65. Fe-rich olivine xenocryst in NWA 1670 has core and overgrowth. The chemical composition of core part has a flat pattern and chemical composition gradually changes Mg-rich towards the rim at the overgrowth area. Between the core and overgrowth, chemical composition changes by atomic diffusion. The most Mg-rich olivine phenocryst is Fo_{85}.

This is corresponding to the most Mg-rich olivine phenocryst in NWA 1670. In conclusion, the most Mg-rich olivine phenocryst in NWA 1670 is considered as Fo_{85}. This value is close to the most Mg-rich Fo# (Fo_{82} or Fo_{80}) calculated from bulk chemical composition of NWA 1670 (see 3.3.).

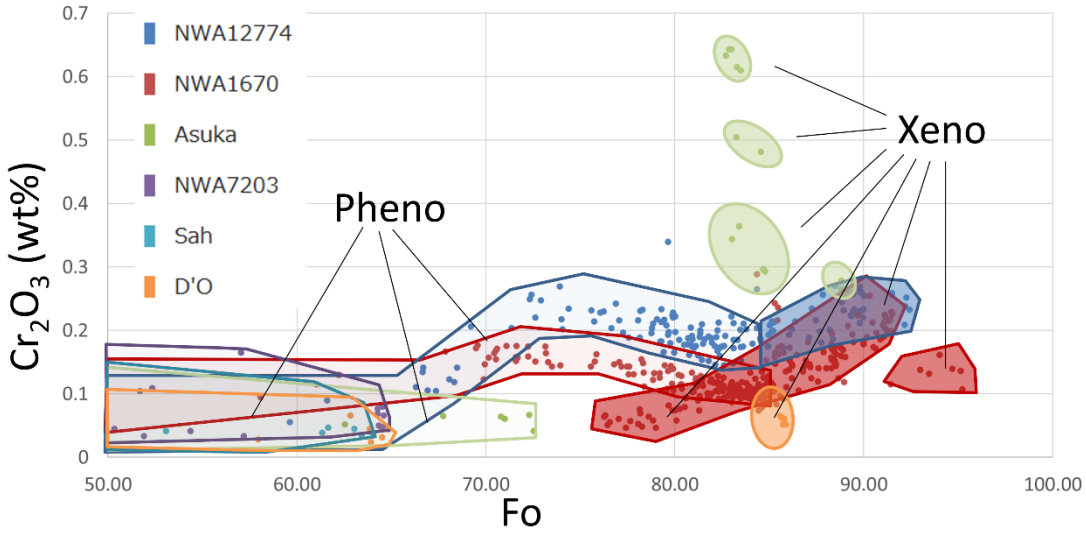

Fig. 60. Fo# *vs.* Cr_2O_3 content in olivines for each quenched angrites.

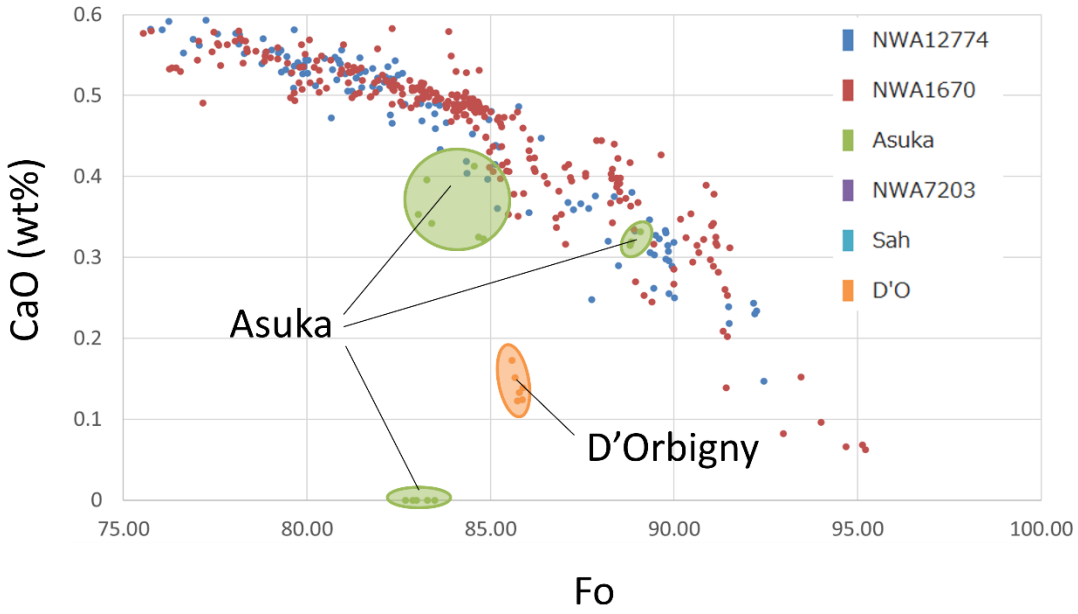

Fig. 61. Fo# *vs.* CaO content in olivines for each quenched angrites. Shades are added for Asuka-881371 and D'Orbigny in order to make it easier to find.

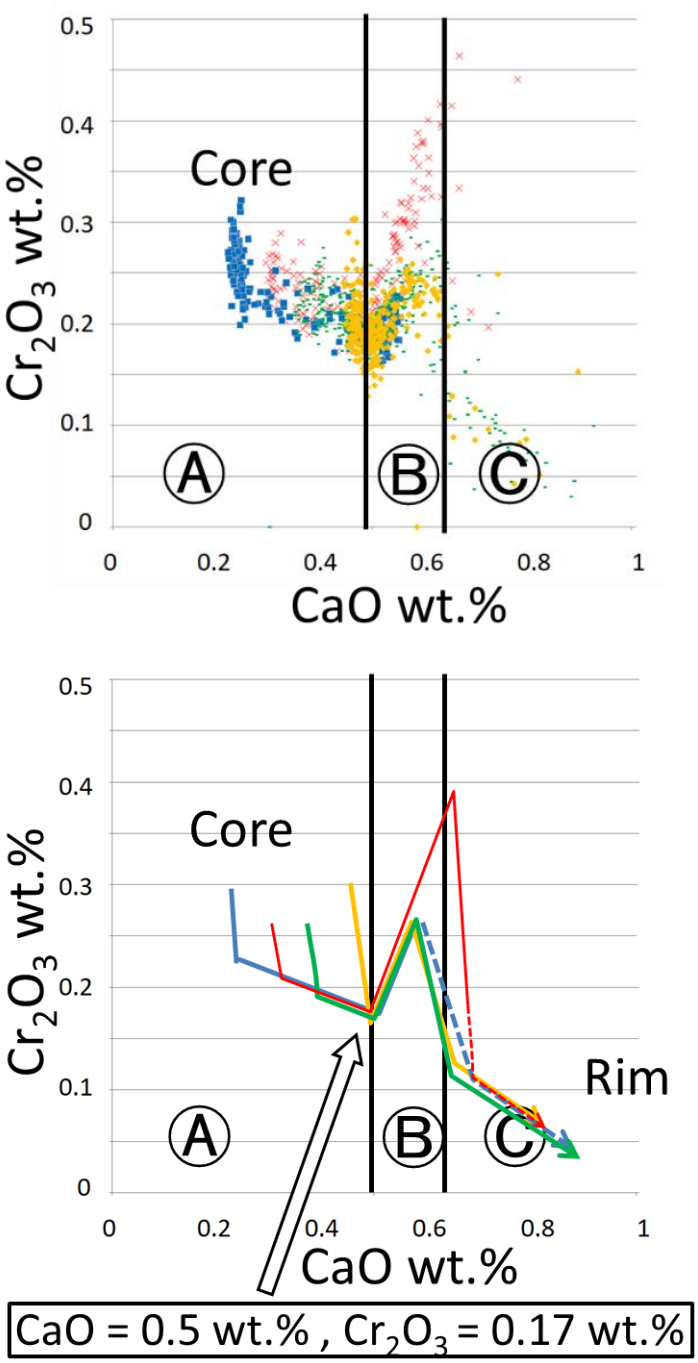

Fig. 62. Cr_2O_3 *vs.* CaO contents in olivines for four line profiles of olivines in NWA 12774 (upper figure). The core compositions of olivines are Fo_{92} for blue symbol, Fo_{90} for red symbol, Fo_{84} for green symbol and Fo_{82} for yellow symbol, respectively. The upper figure shows the raw data, and the lower figure shows the simplified graph. Olivine can be divided in three types (Ⓐ, Ⓑ, and Ⓒ) according to the Cr_2O_3 *vs.* CaO contents in olivines. All olivines go to around CaO = 0.5 wt.% and Cr_2O_3 = 0.17 wt.%.

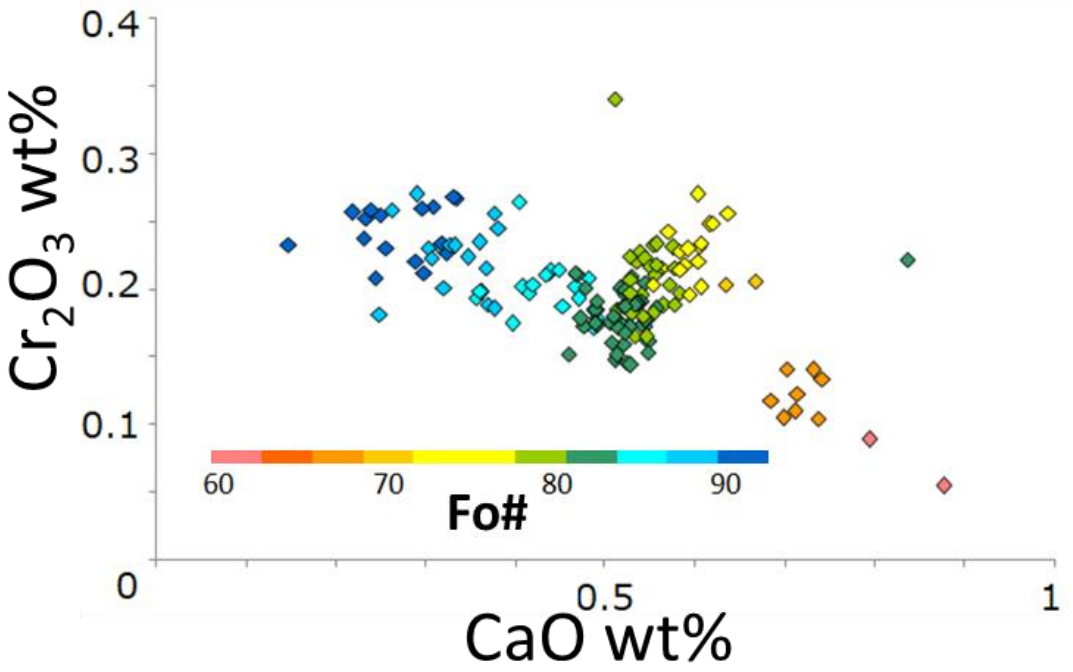

Fig. 63. Cr_2O_3 *vs.* CaO contents and Fo# of the core for olivine grains in NWA 12774. Fo# is shown by the symbol colors. Olivine grains in NWA 12774 show similar trends with four olivines in Fig. 62.

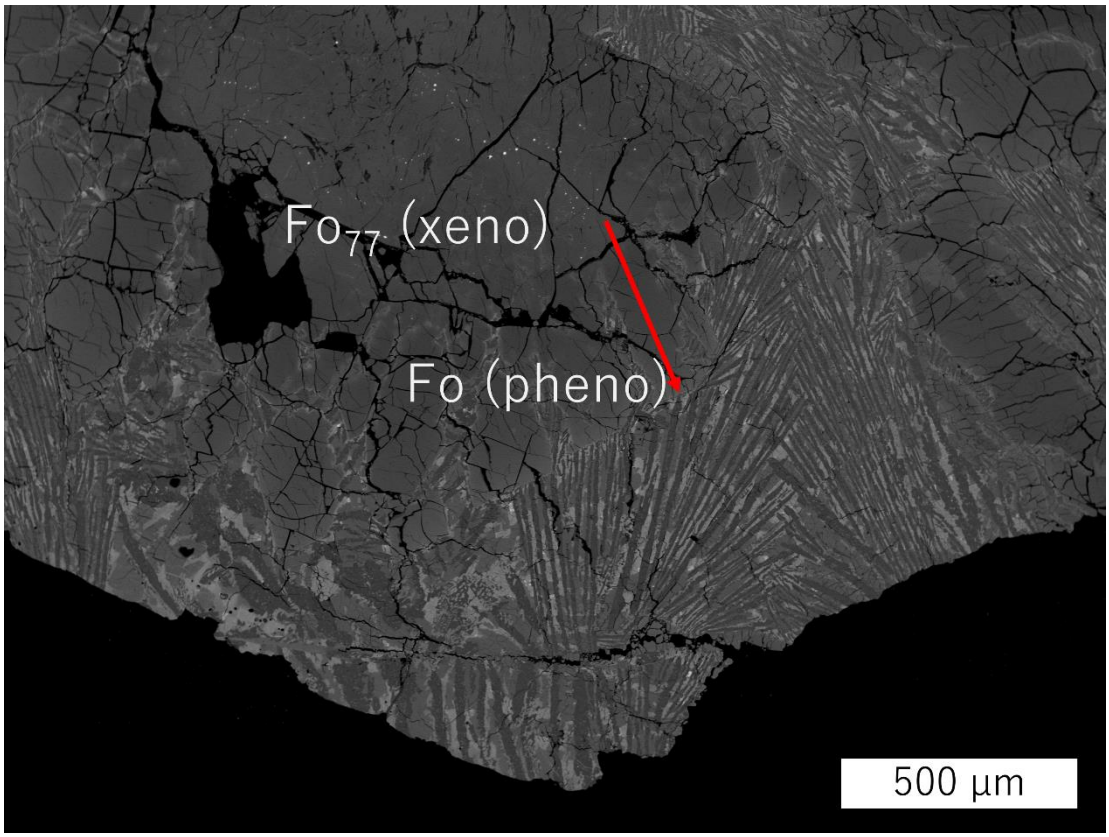

Fig. 64. BSE image of Fe-rich (Fo_{77}) olivine xenocryst in NWA 1670. Line profiles of red arrow part is shown in Fig. 65.

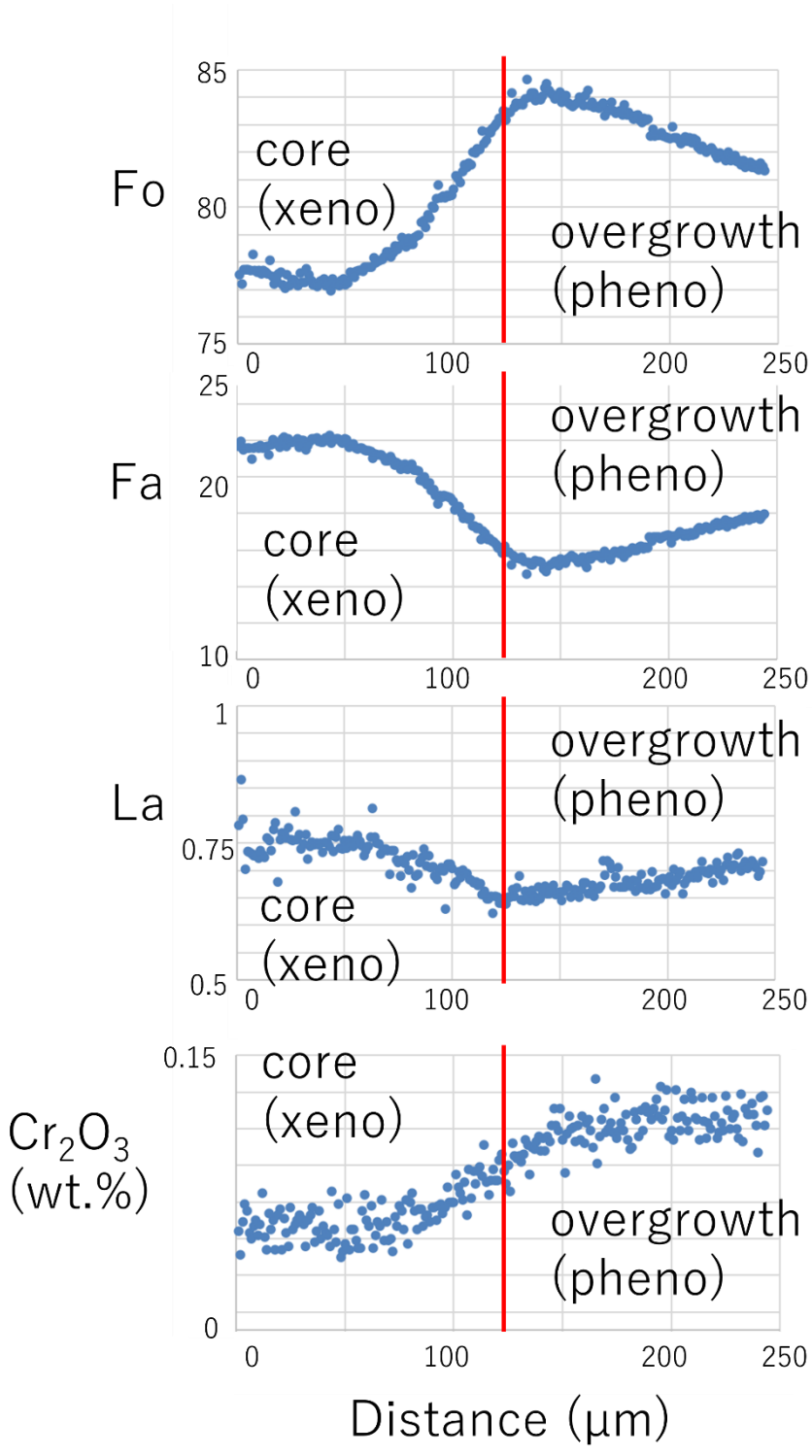

Fig. 65. Line profiles of the Fo_{77} olivine xenocryst in NWA 1670 (red arrow part of Fig. 64). Red solid line corresponds to the boundary of olivine xenocryst and overgrowth assumed from the La profile.

3.5. Oxygen isotopic compositions

（非公開部分）

（非公開部分）

（非公開部分）

（非公開部分）

（非公開部分）

（非公開部分）

3.6. Fe^{3+} ratios of recrystallizing clinopyroxenes in NWA 7203 and NWA 1670

I measured Fe-XANES spectra of recrystallized clinopyroxenes in shock melt veins in NWA 7203 and NWA 1670 (see 3.1.4. and 3.1.5.). In Wilke et al. (2001), the relationship between the energy centroid position (eV) and Fe^{3+}ratio is discussed. I applied Fe^{2+} for the tetrahedral site and Fe^{3+} for the octahedral site, considering the pyroxene crystal structure. Fig. 69 and Fig. 70 show the measurement area of recrystallized clinopyroxene in NWA 7203 (essenite ~ $CaFe^{3+}Fe^{3+}SiO_6$) and NWA 1670 (diopside ~ kushiroite). I also measured a XANES spectrum of clinopyroxene in the coarse-grained lithology of NWA 7203 for comparison. Note that the XANES signal comes from larger (~ around 30 μm) areas than the actual X-ray beam size (~ around 5 μm), and thus the data contain not only clinopyroxene but also other surrounding minerals and glasses in shock melt veins in some amounts. The obtained XANES spectra are shown in Fig. 71 (recrystallized pyroxene in NWA 7203), Fig. 72 (recrystallized pyroxene in NWA 1670) and Fig. 73 (pyroxene phenocryst in NWA 7203). Pre-edge areas are also shown in the figures. Purple gaussian corresponds to the pre-edge of Fe^{2+} and light blue gaussian corresponds to the pre-edge of Fe^{3+}. The area-weighted average position of the centroid peak corresponds to the ratio of Fe^{2+} and Fe^{3+}, and the estimated Fe^{3+}ratios ($Fe^{3+}/(Fe^{2+}+Fe^{3+})$) for each sample using the parameter of Wilke et al. (2001) are shown in Table 9. The Fe^{3+} ratio of recrystallized clinopyroxene in NWA 7203 is 13~16%, and this is the most enriched in Fe^{3+}. The Fe^{3+} ratio of recrystallized clinopyroxene in NWA 1670 is 12~13%. These values are clearly higher than that of normal clinopyroxene (7%), suggesting that certain amount of Fe^{3+} was incorporated to recrystallizing clinopyroxenes in shock melts.

Table 9. The estimated Fe^{3+} ratios for each sample using synchrotron Fe-XANES spectra.

Sample	Fe^{3+} ratio
NWA 7203_PX_1	13%
NWA 7203_PX_2	16%
NWA 7203_Large PX	7%
NWA 1670_PX_1	13%
NWA 1670_PX_2	12%

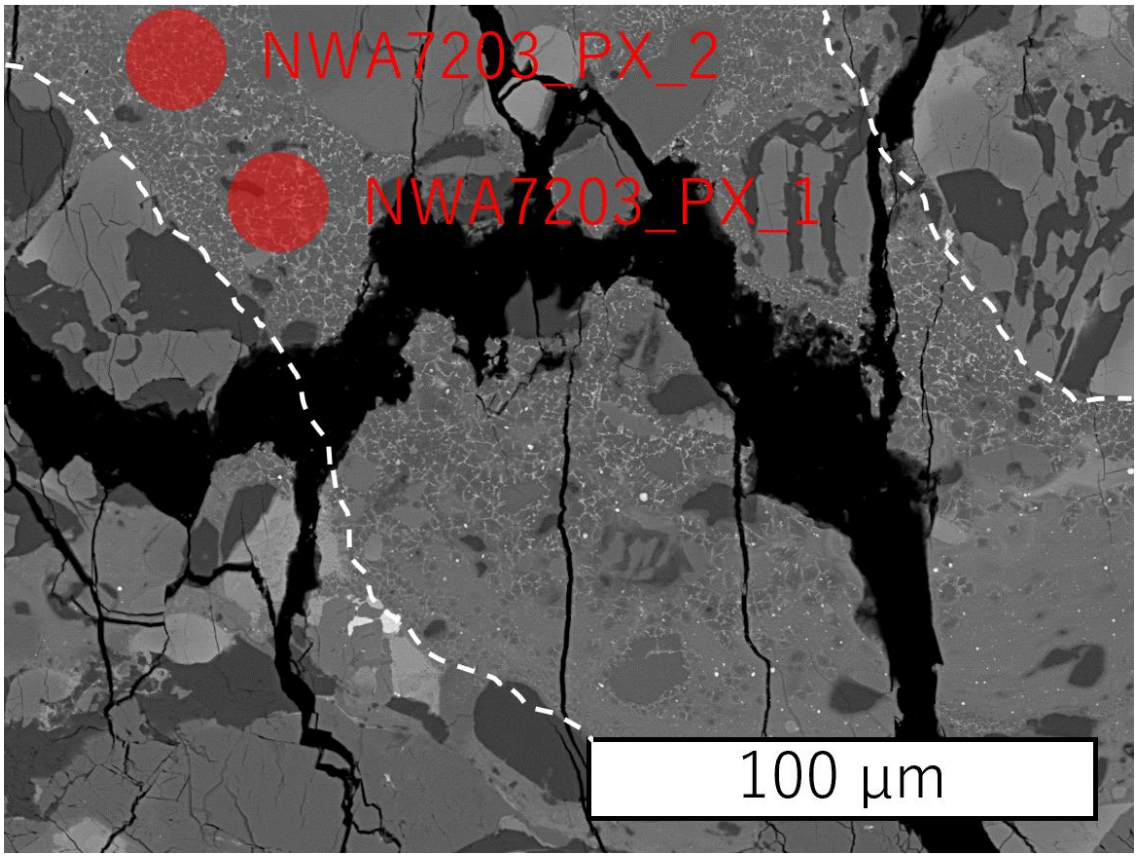

Fig. 69. Measurement area of recrystallized clinopyroxene in NWA 7203 by synchrotron Fe-XANES. The shock melt vein is shown in white dotted lines.

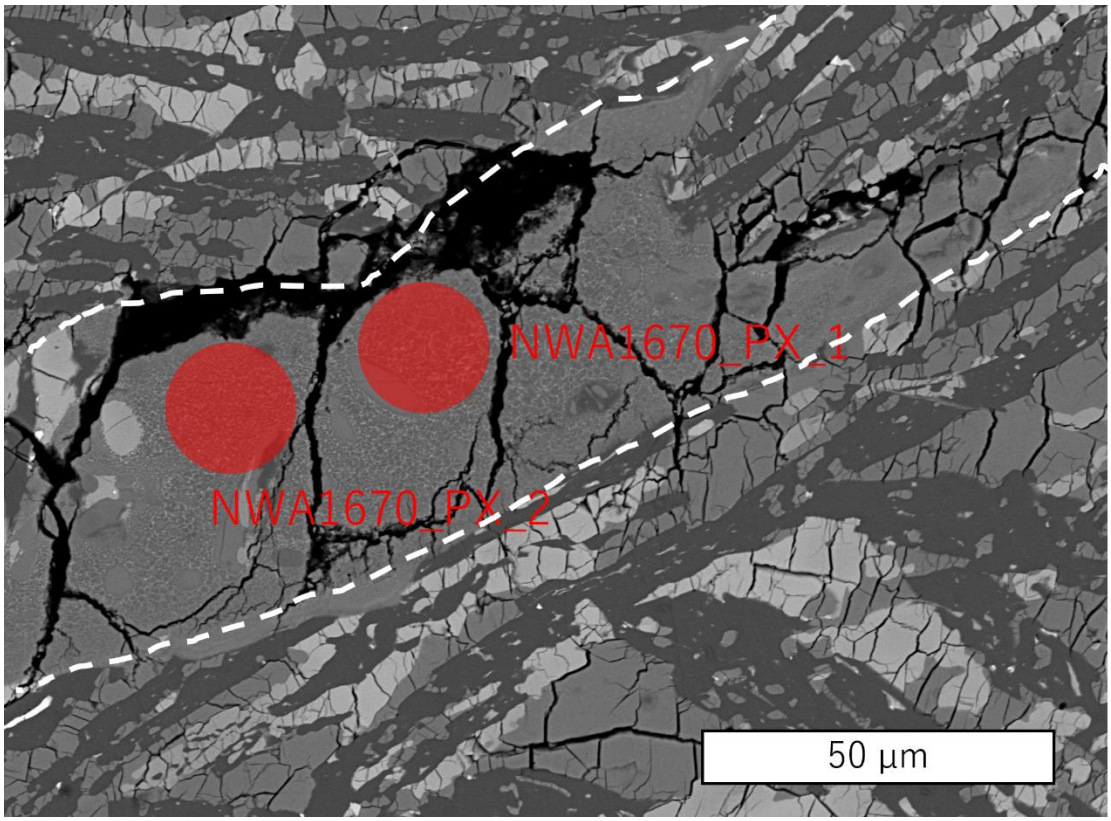

Fig. 70. Measurement area of recrystallized clinopyroxene in NWA 1670 by synchrotron Fe-XANES. The shock melt vein is shown in white dotted lines.

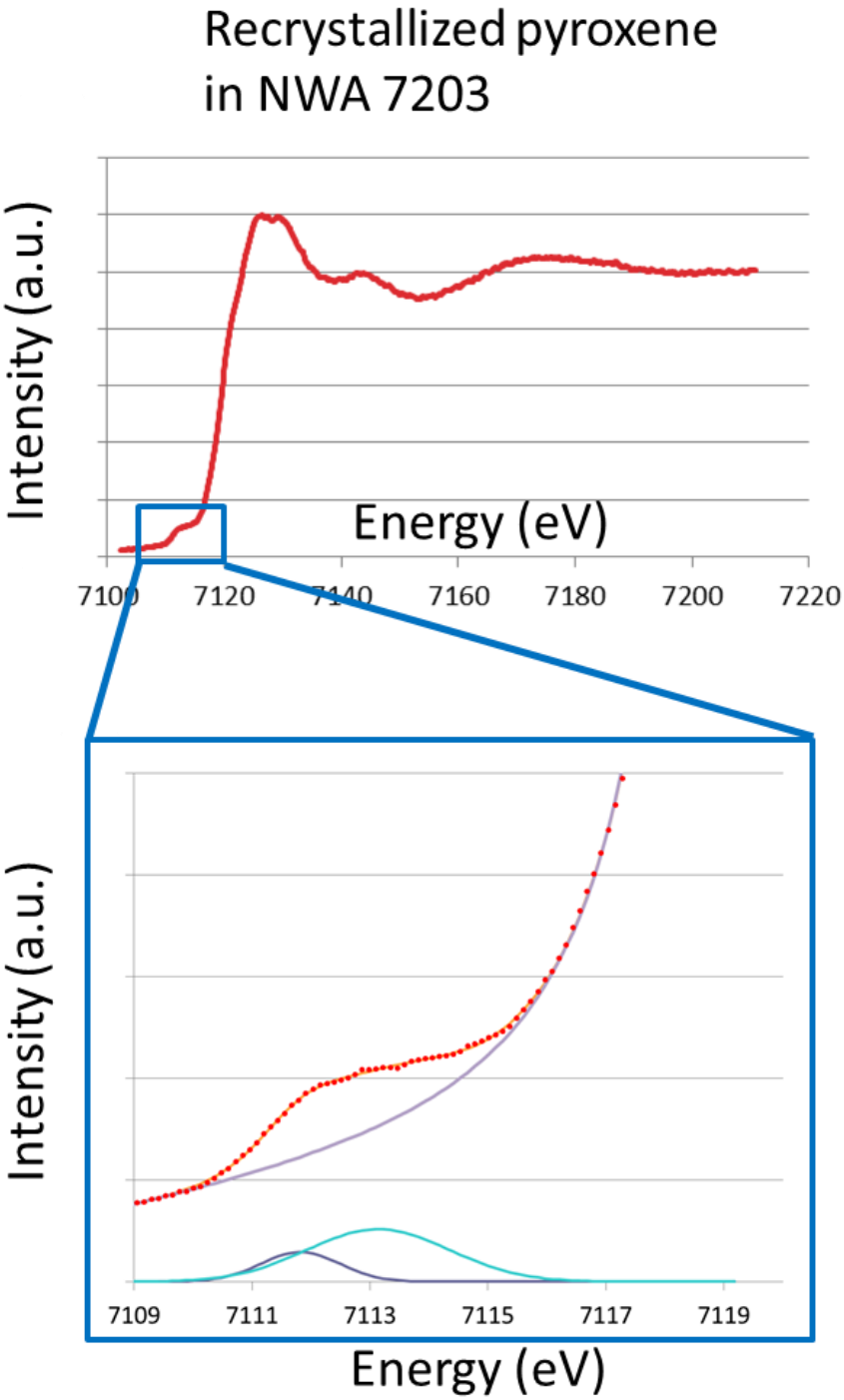

Fig. 71. XANES spectrum of recrystallized pyroxene in NWA 7203 (NWA 7203_PX_1 in Fig. 69). Pre-edge area is also shown. Purple gaussian corresponds to the pre-edge of Fe^{2+} and light blue gaussian corresponds to the pre-edge of Fe^{3+}.

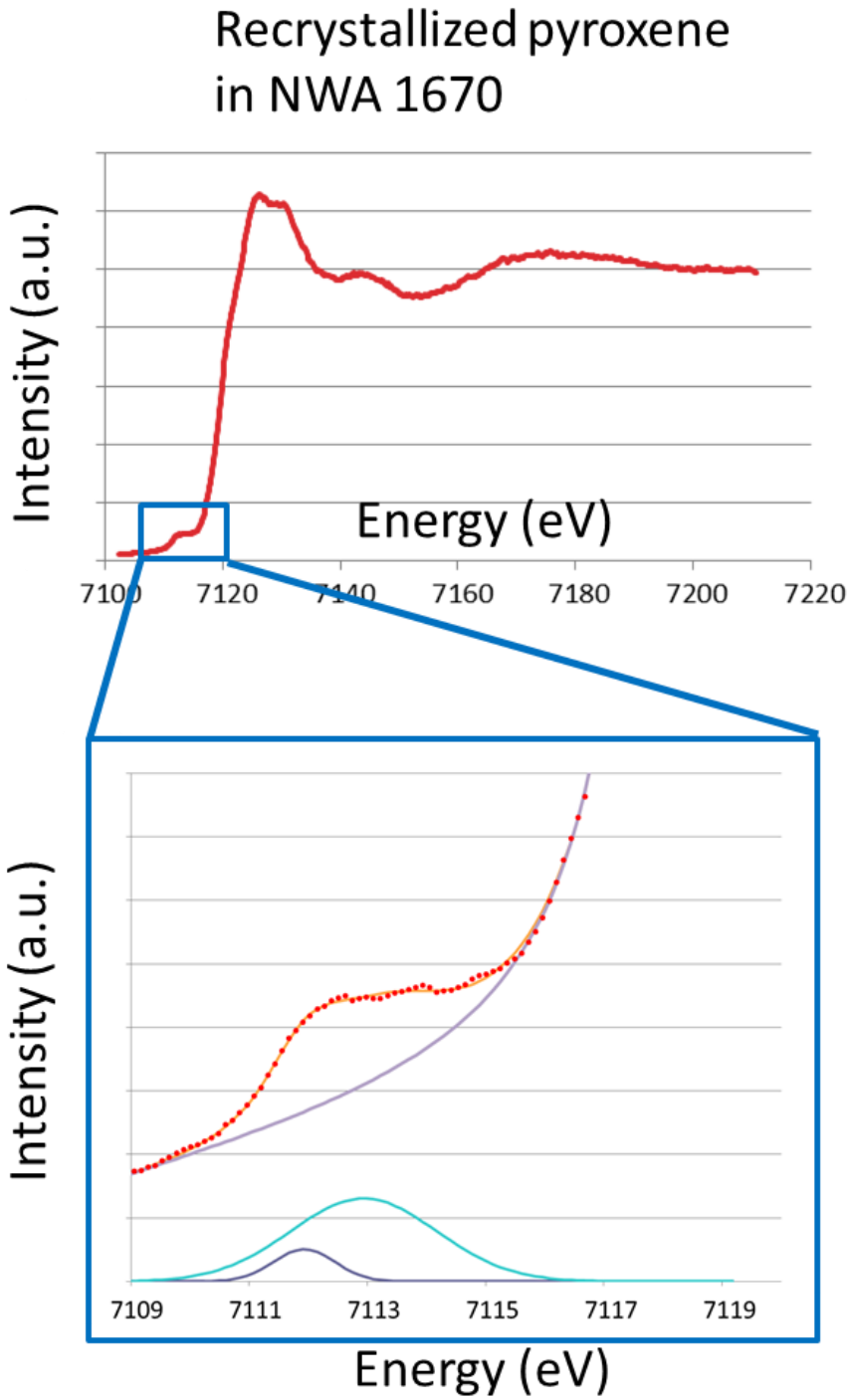

Fig. 72. XANES spectrum of recrystallized pyroxene in NWA 1670 (NWA 1670_PX_1 in Fig. 70). Pre-edge area is also shown. Purple gaussian corresponds to the pre-edge of Fe^{2+} and light blue gaussian corresponds to the pre-edge of Fe^{3+}.

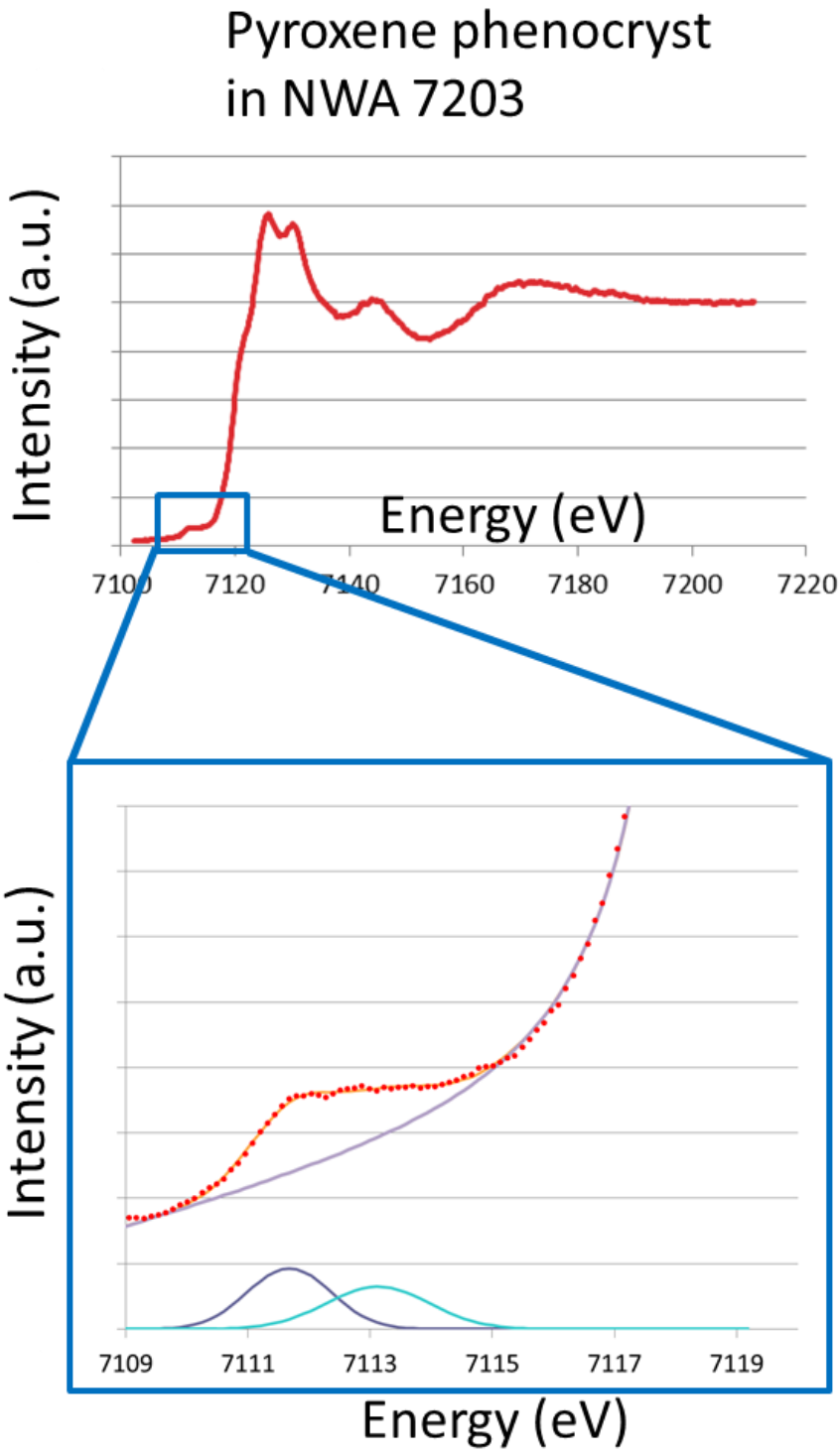

Fig. 73. XANES spectrum of pyroxene phenocryst in NWA 7203. Pre-edge area is also shown. Purple gaussian corresponds to the pre-edge of Fe^{2+} and light blue gaussian corresponds to the pre-edge of Fe^{3+}.

4. Discussion

4.1. Crystallization history of NWA 7203

（非公開部分）

（非公開部分）

（非公開部分）

（非公開部分）

（非公開部分）

4.2. Comparison between NWA 7203 and other quenched angrites

（非公開部分）

（非公開部分）

（非公開部分）

（非公開部分）

4.3. Shock metamorphism of angrites

（非公開部分）

（非公開部分）

（非公開部分）

4.4. Bulk chemical compositions of quenched angrites

Reported bulk chemical compositions of quenched angrites are summarized in Table 7 along with NWA 7203 and NWA 12774 obtained in this study by EPMA grid analyses. Mikouchi et al. (2004) discussed the bulk chemical compositions of quenched angrites. They discussed that two elemental compositional systematics of bulk chemical compositions of quenched angrites show correlations, that can be explained by incorporation of Mg-rich olivine xenocrysts (e.g., Fo_{90}, CaO = 0.40 wt.% and Cr_2O_3 = 0.45 wt.%). However, there are only a few quenched angrite samples known at that time, and so the relationship between bulk chemical compositions and textures of quenched angrites was unclear and not discussed. I plotted compositional systematics for each element of bulk chemical compositions of angrites in Fig. 77 (CaO-MgO), Fig. 78 (CaO-Cr_2O_3), Fig. 79 (CaO-TiO_2) and Fig. 80 (FeO-MgO). In Fig. 77 to Fig. 80, dendritic quenched angrites are shown in purple symbols, coarse-grained samples are shown in light blue symbols and anorthite spinifex samples are shown in green symbols, respectively. Slowly-cooled angrites (e.g., Angra dos Reis, LEW 86010) are shown in red symbols for comparison. Bulk chemical compositional change of Sahara 99555 is shown by a red arrow when olivine with the angritic xenocryst composition (Fo_{90}, CaO = 0.40 wt.% and Cr_2O_3 = 0.45 wt.%, following Mikouchi et al., 2004) is added. All four elemental compositional systematics show correlations. From these figures, Sahara 99555, D'Orbigny, NWA 1296 and NWA 7203 have similar bulk chemical compositions and might represent a 'pristine angrite magma' which corresponds to the parent melt of quenched angrites. The absence or rarity of olivine xenocrysts in these angrites supports this hypothesis. Thus, incorporation of olivine xenocrysts is considered as minor for NWA 1296, Sahara 99555, NWA 7203 and D'Orbigny. In contrast, the proportion of incorporated xenocryst in magma would be 20 % for Asuka-881371 and NWA 1670, and 40 % for LEW 87051 and NWA 12774 when Fig. 77 ~Fig. 80 are collectively considered. However, the Cr content of NWA 12774 is higher (Fig. 78). This is accommodated to the fact that NWA 12774

contains Cr-rich clinopyroxenes (Table 6) and large Cr-rich spinel. Large Cr-rich spinel is known only in NWA 12774 and NWA 8535 (Santos et al., 2016b) among quenched angrites. One of the reasons that the bulk chemical composition of NWA 12774 is Cr-rich is incorporation of Cr-rich olivine or spinel xenocrysts. Another explanation is that large Cr-rich spinel crystallized at the end of the crystallization process. I consider that olivine xenocrysts sank towards the deeper place in a common igneous body of quenched angrites (see 4.7). Such large Cr-rich spinel is found only in NWA 8535 and NWA 12774 (and NWA 1670; smaller and Cr-poor, shown in Fig. 82), corresponding deeper samples of the igneous body of quenched angrites (see 4.7). These Cr-rich spinel grains are present associated with the olivine xenocrysts, supporting the late crystallization of large Cr-rich spinel because Cr-rich spinel grows with olivines as crystallization seeds. Hercynitic spinel is considered to crystallize as the second phase during olivine crystallization from the D'Orbigny bulk chemical composition (the first phase is Mg-rich olivine phenocryst) (Mittlefehldt et al., 2002; Longhi, 1999), and this is also consistent with late-stage crystallization of Cr-rich spinel in NWA 12774. Thus, I prefer the latter explanation for the reason of Cr-rich bulk chemical composition of NWA 12774.

The Fe contents of quenched angrites do not show strong correlations with Mg and other elements. This might be caused by the variation of Fo# of incorporated olivine xenocrysts. Incorporation degree of olivine xenocrysts is compiled in Fig. 81. In Fig. 81, incorporation degree of olivine xenocrysts is the lowest in dendritic samples and some of relatively coarse-grained samples (D'Orbigny and Sahara 99555), intermediate in Asuka-881371 and the highest in anorthite spinifex samples. This indicates that incorporation degree of olivine xenocrysts in quenched angrites and bulk chemical compositions of quenched angrites are correlated.

Fig. 83 shows REE contents normalized to the abundance of CI chondrite for each quenched angrite. REE patterns change when olivine xenocryst is added (containing small amount of REE,

reported in Sanborn and Wadhwa, 2010) to Sahara 99555, which is considered to have “pristine angrite magma” chemical composition of quenched angrites. The REE patterns of quenched angrites thus show flat patterns. This means that REE patterns of quenched angrites do not show evidence for fractional crystallization except for olivine, rather supporting simple mechanical mixing of ‘pristine angrite magma’ and olivine xenocrysts. Olivine fractional crystallization does not change the flat REE patterns, and this is also possible to have occurred in some quenched angrites.

HSE abundances and U isotope compositions of quenched angrites are obtained by Riches et al. (2012) and Tissot et al. (2017). The HSE abundances and U isotope compositions of quenched angrites might be also explained by simple mechanical mixing of ‘pristine angrite magma’ and olivine xenocrysts, but it is difficult to conclude because the data in Riches et al. (2012) and Tissot et al. (2017) do not contain sufficient sample numbers to discuss, and do not show a strong correlation.

“Pristine angrite magma” is considered to be produced by partial melting of quenched angrite source. Jurewicz et al. (1993) showed that ~ 30% partial melting of CV or CM chondritic material at around 1200 ^{o}C under an oxidizing condition ($\log fO_2$=IW+2) will produce partial melts with very similar composition of “pristine angrite magma” (Mikouchi et al., 2004). Thus, I consider that the quenched angrite source might be a CV or CM chondrite like material in terms of major-minor elemental compositions.

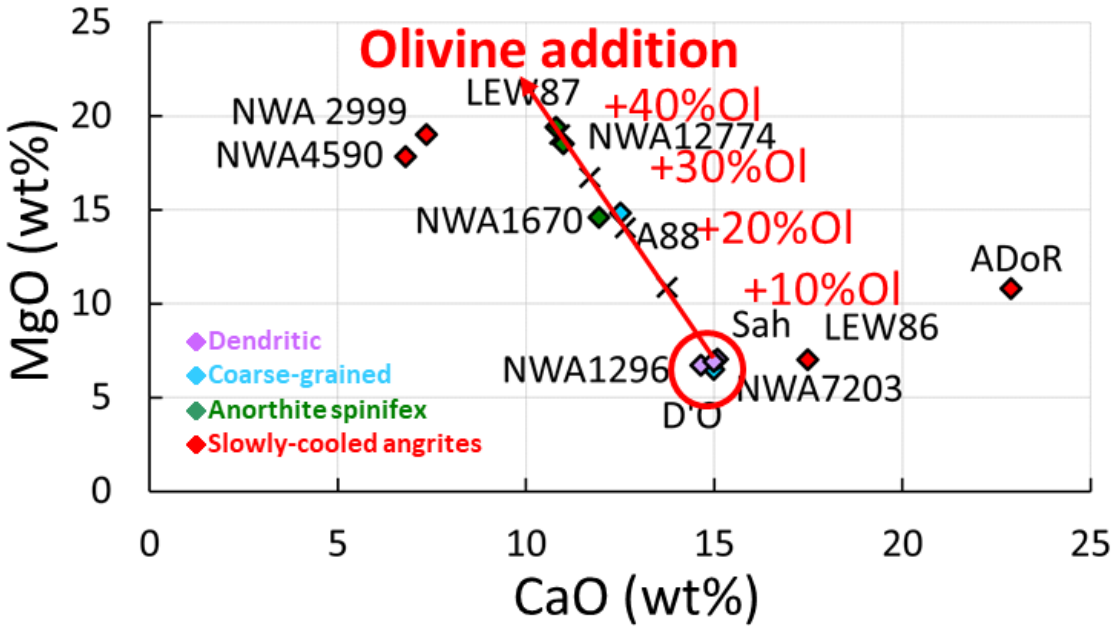

Fig. 77. CaO-MgO systematics of bulk chemical compositions of angrites.

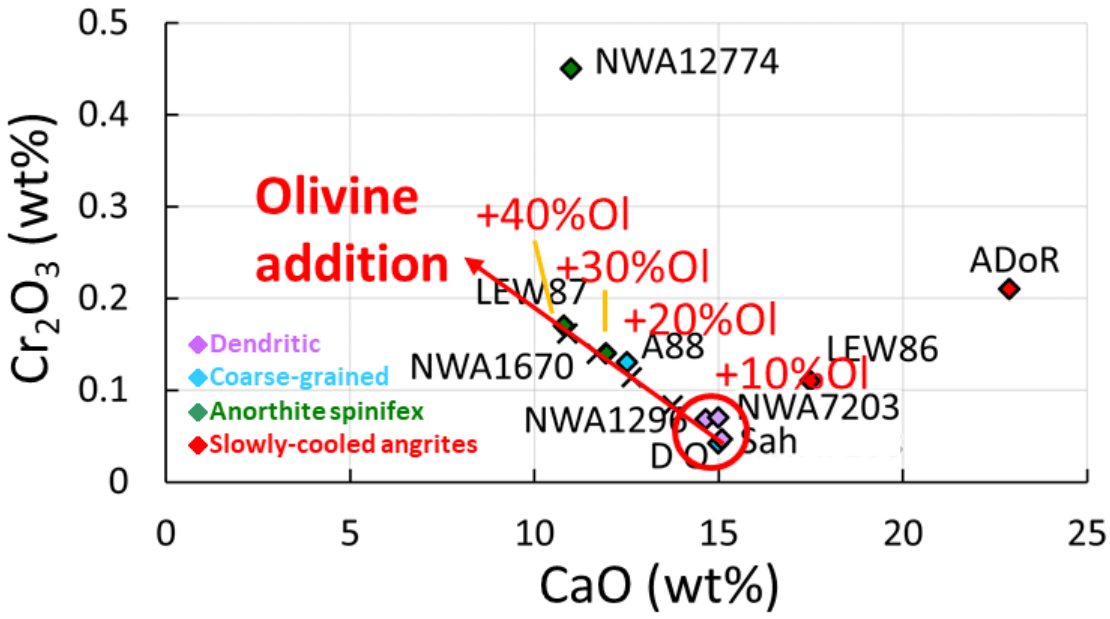

Fig. 78. CaO-Cr_2O_3 systematics of bulk chemical compositions of angrites.

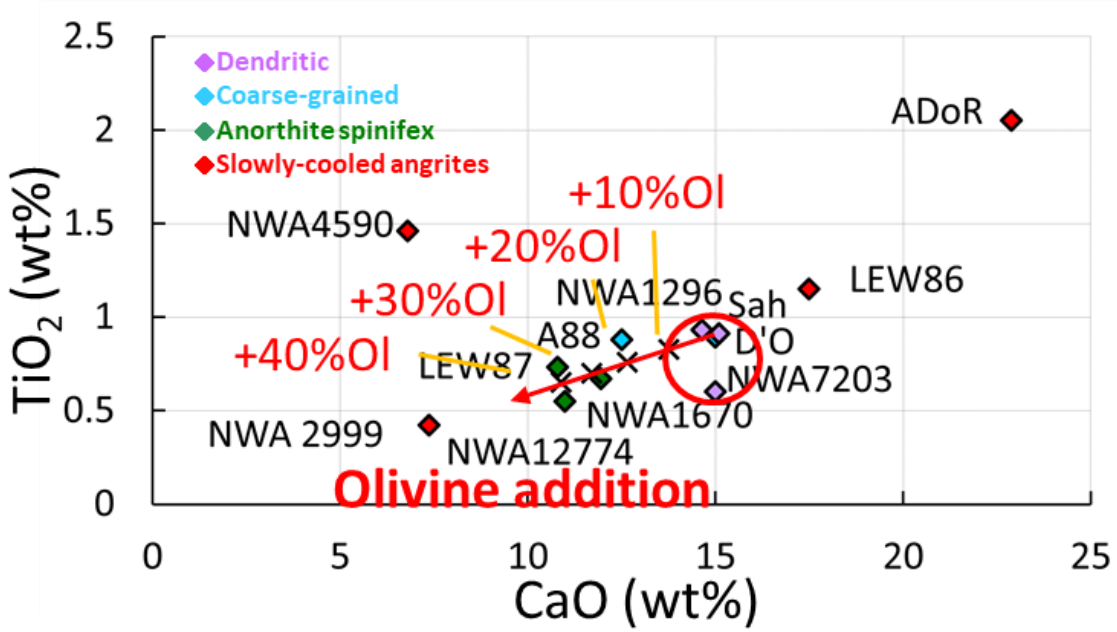

Fig. 79. CaO-TiO_2 systematics of bulk chemical compositions of angrites.

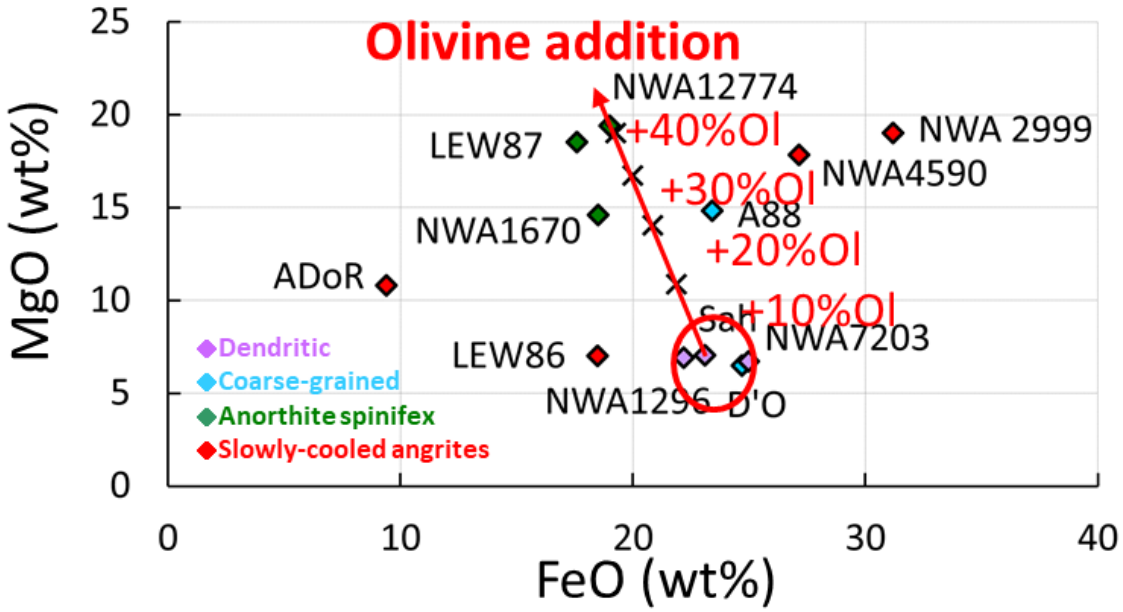

Fig. 80. FeO-MgO systematics of bulk chemical compositions of angrites.

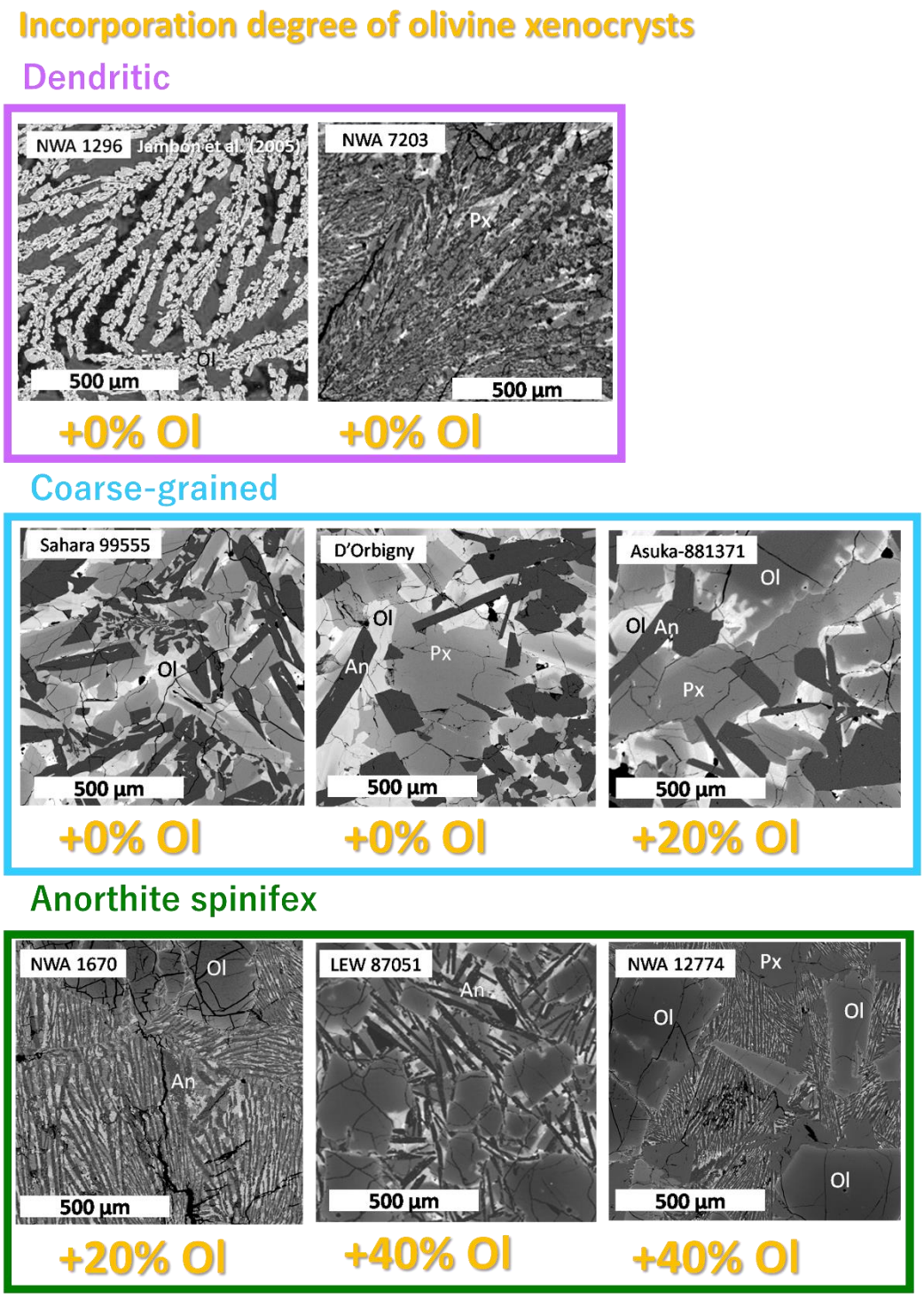

Fig. 81. Incorporation degree of olivine xenocrysts for each quenched angrites. Incorporation degree of olivine xenocrysts is the lowest in dendritic samples and some of relatively coarse-grained samples (D'Orbigny and Sahara 99555), intermediate in Asuka-881371 and the highest in anorthite spinifex samples. The BSE image of NWA 1296 taken from Jambon et al. (2005).

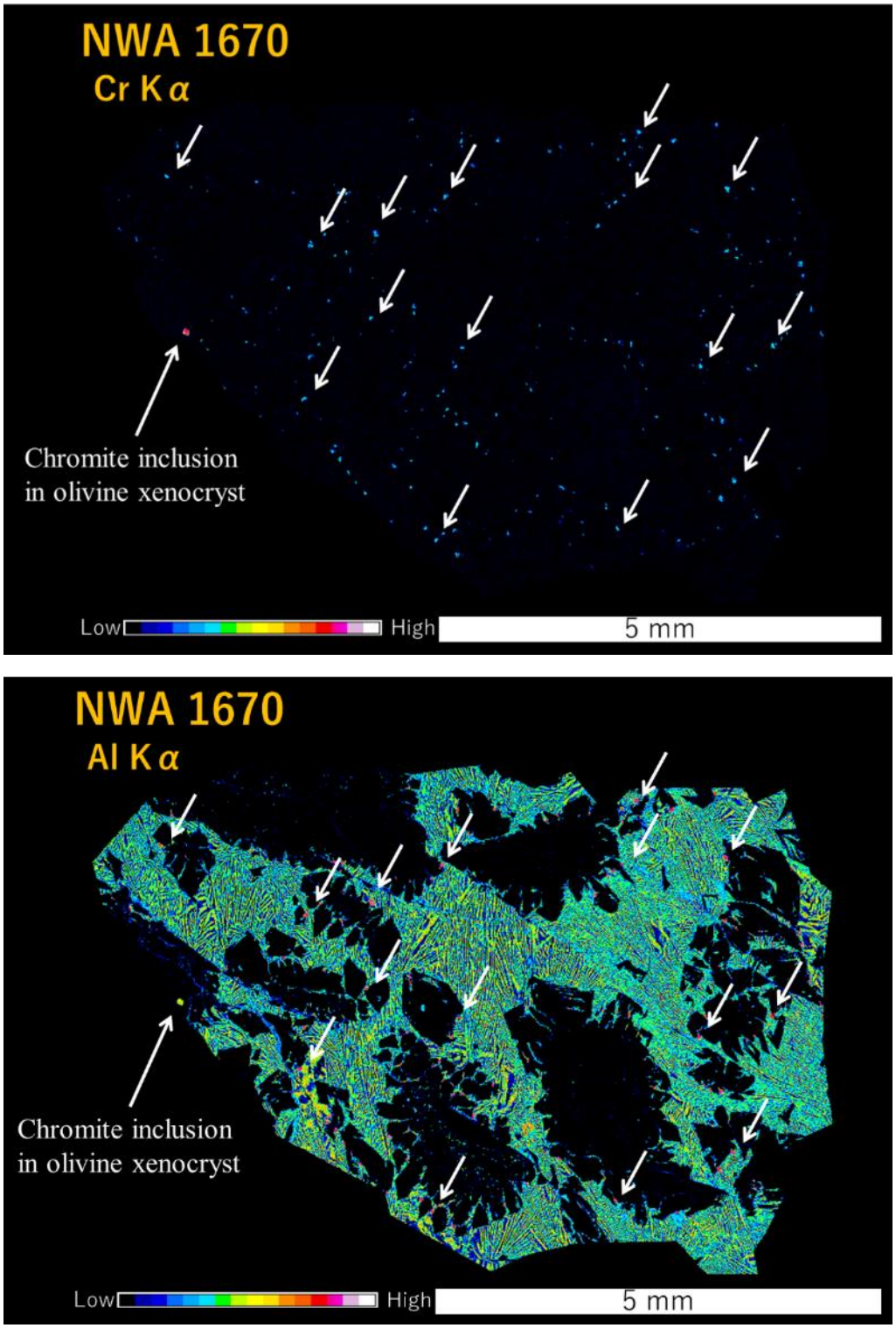

Fig. 82. Spinels found in Cr X-ray map of NWA 1670 (upper figure) and Al X-ray map of NWA 1670 (lower figure). Spinels occur associated with large olivine xenocrysts (shown in Al X-ray map of NWA 1670 as large dark area).

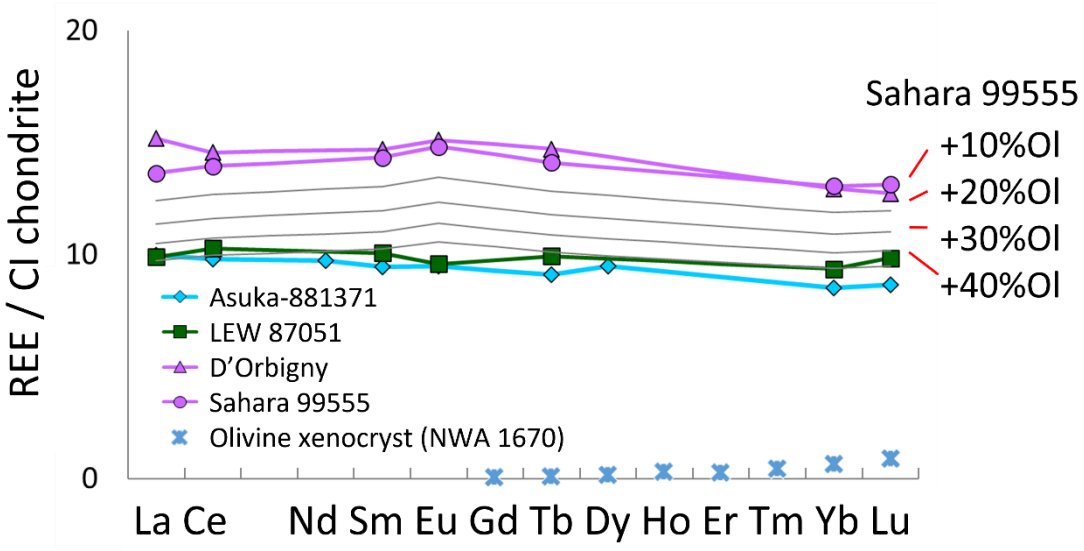

Fig. 83. REE patterns of quenched angrites. REE patterns change when olivine xenocryst is added (containing small amount of REE, reported in Sanborn and Wadhwa, 2010) to Sahara 99555 (10, 20, 30, and 40 %) are also shown.

4.5. Incorporation of olivine xenocrysts

In terms of bulk chemical compositions of quenched angrites, it seems that olivine xenocrysts were incorporated into 'pristine angrite magma' (see 4.4.). In order to understand the incorporated process of olivine xenocrysts, firstly I estimated the modal abundances of olivine xenocrysts in quenched angrites from X-ray elemental maps. Olivine xenocrysts are found in D'Orbigny, Asuka-881371, NWA 1670 and NWA 12774 in the thin sections studied. Modal abundances of olivine xenocrysts in D'Orbigny and Asuka-881371 are easy to obtain because the Fo# of olivine phenocrysts and olivine xenocrysts can be clearly separated. Modal abundances of olivine xenocrysts in NWA 12774 may contain some errors because Fo# of olivine phenocrysts ($Fo_{\leqq 84}$) and olivine xenocrysts are ($Fo_{\geqq 84}$) close to each other, and thus ~Fo_{84} olivines are difficult to distinguish. Some olivine xenocrysts in NWA 1670 are more Fe-rich compared to the most Mg-rich olivine phenocrysts, and thus it is difficult to distinguish olivine phenocrysts and olivine xenocrysts perfectly from the X-ray map. Modal abundances of olivine xenocrysts are estimated as 0% for Sahara 99555 and NWA 7203, ~0% for D'Orbigny, 14% for Asuka-881371, ~11% for NWA 1670 and 13% for NWA 12774. Modal abundances are 0% (no olivine xenocrysts; Jambon et al., 2005) for NWA 1296 and 10% for LEW 87051 (Mikouchi et al., 1996) (Fig. 84).

The most Mg-rich olivine phenocrysts are Fo_{64} for Sahara 99555 and NWA 7203, Fo_{65} for D'Orbigny, Fo_{72} for Asuka-881371, Fo_{84} for NWA 12774 and Fo_{85} for NWA 1670, respectively (see 3.1.1. ~ 3.1.6.). The most Mg-rich olivine phenocryst with Fo_{64} is reported for NWA 1296 (Jambon et al., 2005) and Fo_{80} for LEW 87051 (Mikouchi et al., 1996).

As I discussed above, I propose that olivine xenocrysts were incorporated into "pristine angrite magma" from the view of variation of bulk chemical compositions. From modal abundances of olivine xenocrysts and the most Mg-rich olivine phenocryst compositions, it can be concluded that olivine xenocrysts are dissolved into 'pristine angrite magma', which made the melt composition

more Mg-rich, but some of olivine xenocrysts remain unmelted. This model is consistent with the fact that olivine xenocrysts are present as relict cores of large olivine grains. Olivine fractional crystallization is considered to have occurred with overgrowth of olivine xenocrysts and sinking of olivine xenocrysts.

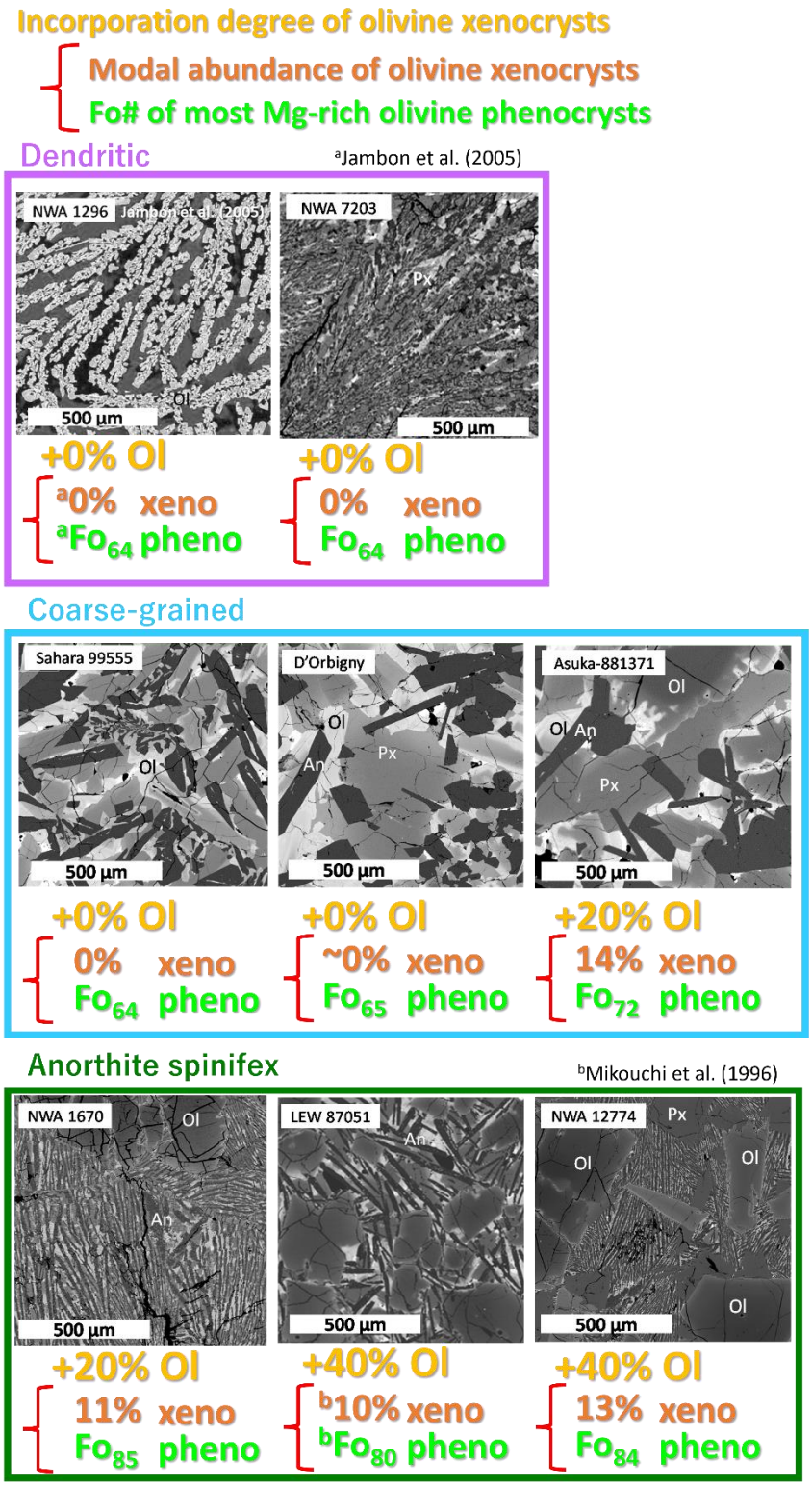

Fig. 84. Modal abundances of olivine xenocrysts and Fo# of most Mg-rich olivine phenocrysts for each quenched angrite. Incorporation degrees of olivine xenocrysts for each quenched angrite are also shown. The BSE image of NWA 1296 taken from Jambon et al. (2005).

4.6. Origin of olivine xenocrysts

Olivine xenocrysts have variety of Fo#, Ca and Cr contents. It is difficult to crystallize these olivine crystals in a single crystallization process. The origin of olivine xenocrysts has been discussed by several earlier works, but no conclusion has been reached. There are three possibilities of the origin of olivine xenocrysts: remnant of mantle materials (Jambon et al., 2008), crystallization from impact melts (Jambon et al., 2008) and relict impactors (Keil, 2012). For the impact melt hypothesis, Keil (2012) discussed that total impact melt rock is difficult to generate (Keil et al., 1997), and thus it seems implausible. However, both remnant of mantle materials and relict impactors hypotheses are not denied.

As shown above, oxygen isotopic ratios of olivine xenocrysts in NWA 12774 plot on the AFL (see Fig. 68). This means that olivine xenocrysts in NWA 12774 crystallized in APB, not in other source regions of the solar system. From this, mantle material of APB is the most plausible origin of olivine xenocrysts.

If I consider the presence of mm-sized Mg-rich olivine grains with homogeneous cores in achondrite meteorites, ureilite is known with such characteristics. Olivines in ureilite are coarse-grained (~several mm), ranging in composition from Fo_{74} to Fo_{95}, and olivine core compositions within each ureilite are homogeneous (e.g., Mittlefehldt et al., 1998). In the ureilite parent body (UPB), Mg# of mantle materials varies depending on burial depth (Goodrich et al., 2004), and homogeneous coarse-grained olivines found in polymict ureilites are considered as breccias of mantle materials. Such characteristics of ureilite olivine are similar to olivine xenocrysts in quenched angrites. Olivine xenocrysts in quenched angrites are large crystals (~mm), have homogeneous cores with variety of Fo# and Ca and Cr contents, which are most likely to come from the different depth locations of the APB mantle. In this scenario, olivine in the mantle was trapped by parental melt and then brought to near or on the surface of APB. This is consistent with the model

proposed by Sanborn and Wadhwa (2021) that the parent melt of quenched angrites formed by partial melting of their reservoir and crystallized in a near-surface environment. A schematic illustration is shown in Fig. 85. The parent melt was produced by the partial melting of the quenched angrite source at depth (see 4.4.). The parent melt rose from a quenched angrite source in mantle to the surface during which olivine grains having various Fo# was trapped by the parent melt. Then, the parent melt was erupted on the surface of the APB and quenched at the surface. Alternatively, if the mantle of the APB has heterogeneous olivine chemical compositions, the mantle did not have to be compositionally layered.

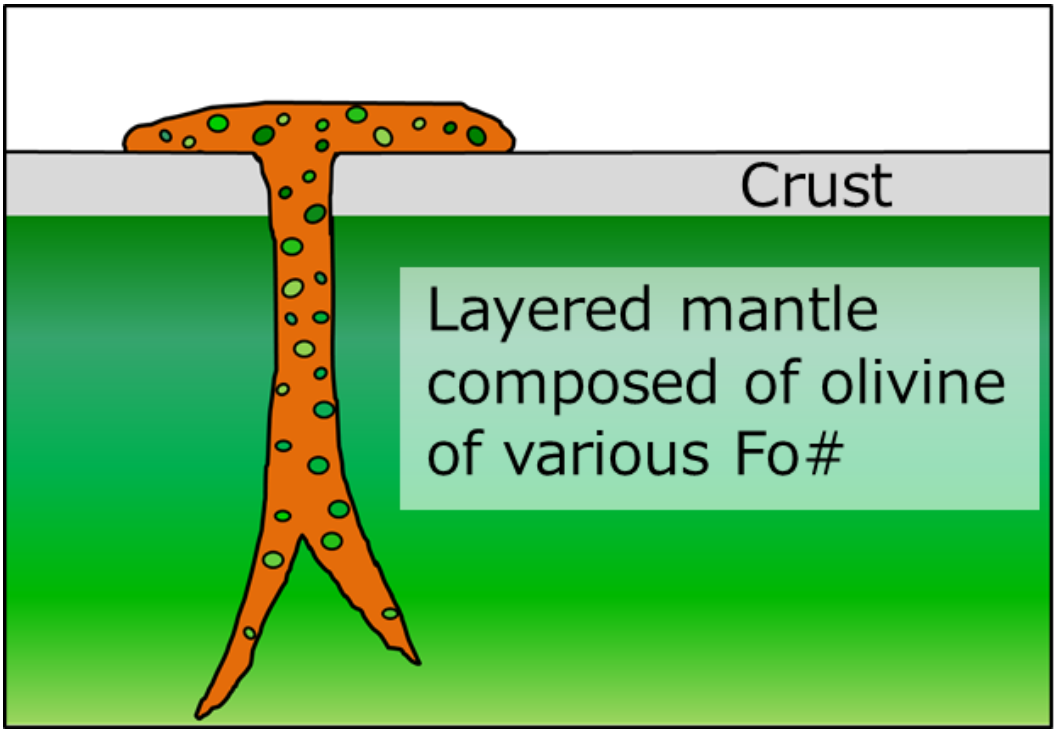

Fig. 85. Schematic illustration of partial melting of the quenched angrite source, olivine trapping by the parent melt, and eruption process of quenched angrites.

4.7. Stratigraphy of the igneous body of quenched angrites

As I estimated the cooing rates of quenched angrites in 3.1., at the conditions from 1400 ºC to 900 ºC linearly at logfO_2=IW+2, cooling rates are estimated as >300 ºC/hr for the fine-grained lithology of NWA 7203, 100 ºC/hr for D'Orbigny, 50 ºC/hr for Asuka-881371, 3 ºC/hr for NWA 1670 and 3.5 ºC/hr for NWA 12774. I also estimated the cooling rate of LEW 87051 from the line profile data reported in Mikouchi et al. (1996) in the same condition above and obtained 18 ºC/hr (Fig. 86). These cooling rates are compiled in Fig. 87. In Fig. 87, it is obvious that cooling rates are faster in dendritic samples, middle in relatively coarse-grained samples and slower in anorthite spinifex samples. This indicates that the texture of quenched angrites varies according to the burial depth in the igneous body of quenched angrites.

I discussed textures, bulk chemical compositions and cooling rates of quenched angrites in the previous sections (see 3.2. and 4.4.). I summarized textures, cooling rates, bulk chemical compositions, modal abundances of olivine xenocryst and Fo# of the most Mg-rich olivine phenocrysts in Fig. 87. Textures and bulk chemical compositions of quenched angrites have correlations, and textures and cooling rates of quenched angrites are also correlated. Thus, it is interpreted that cooling rates change depending on depth in a lava flow, indicating that quenched angrites came from a single common igneous body where bulk chemical compositions and cooling rates change depending on burial depth. Cooling rates are faster near the surface and slower at a lower part, producing textural varieties. The bulk chemical compositions of the samples are pristine (Mg-poor and true parent melt composition) near the surface and Mg-rich at a lower part due to accumulation of the trapped mantle olivine xenocrysts by sinking in the igneous body. Both modal abundance of olivine xenocryst and Fo# of the most Mg-rich olivine phenocrysts increase according to the increment of incorporation degree of olivine xenocrysts, indicating that olivine xenocrysts are dissolved into 'pristine angrite magma', which made the melt composition more Mg-rich, but some

of olivine xenocrysts remain unmelted (see 4.5.). From these results, the possible stratigraphy of the igneous body of quenched angrites is proposed as Fig. 88. In Fig. 88, quenched angrites can be divided into four types based upon texture: dendritic, relatively coarse-grained, anorthite spinifex and cumulate from the top to bottom of the igneous body. The burial depth of LEW 87051 is estimated around 2 m from the surface from thermal conductivity and cooling rate (Mikouchi et al., 1995). LEW 87051 shows an anorthite spinifex texture which exists near the bottom of the igneous body of quenched angrites, and thus the layer thickness might be ~several meters. Each quenched angrite has a single texture implying that the crystallization process of most quenched angrites was controlled by a simple cooling event except NWA 7203 that exhibits two distinct textures (fine-grained variolitic texture and coarse-grained dendritic texture) with a 1-2 mm transition zone, suggesting that NWA 7203 records cooling rate variations of a single eruption cycle in which a lobe of quenching basalt is overridden by a new breakout of lava from the main flow. The cooling rate of NWA 8535 dunite angrite is not obtained, but it is suggested that NWA 8535 would be located near the bottom of the lava because of its olivine-enriched characteristics. The stratigraphy of the igneous body of quenched angrites shown in Fig. 88 is similar to that of komatiite formed in Archean age on the surface of the earth. I will discuss the stratigraphic comparison between quenched angrites and komatiites in 4.8. First, I will discuss the formation process of the igneous body of quenched angrites.

As considered above, I propose the formation process of the igneous body of quenched angrites as follows; (a) The parent melt was produced by the partial melting of the quenched angrite source and rose to near the surface as trapping the mantle olivine at variable depths. (b) A lava flow with trapped mantle olivine as Mg-rich olivine xenocrysts was erupted onto the surface of the APB. (c) Rapid cooling of the lava flow and sinking and melting of olivine xenocrysts started. (d) Subsequent lava flow came and overlay on NWA 7203 in the middle of the crystallization. (e) Cooling rates were

faster near the surface and slower at a lower part, producing textural varieties. Cooling rate change produced both fine-grained and coarse-grained areas of NWA 7203. A schematic illustration of the formation process of the igneous body of quenched angrites is shown in Fig. 89.

This process is nearly identical to that of terrestrial komatiite, although olivine xenocrysts are not present in komatiite except a rare case. I will further compare quenched angrites and komatiites in terms of their igneous bodies in the next paragraph.

In order to evaluate the validity of this model, I checked whether olivine could sink to the bottom of the igneous body before crystallization completed. The falling terminal velocity of olivine is described as follows.

$$V = \frac{2r^2 g \Delta\rho}{9\eta}$$

where r = radius of olivine crystal, g = gravity of the APB, $\Delta\rho$ = density difference between olivine and the melt, and η = viscosity of the melt. The gravity of APB is described as $g = \frac{4\pi}{3} \cdot G\rho r$, where r = radius of APB and ρ = density of the APB, respectively. I assume that density of the APB as 4000 kg/m^3 (4 Vesta that has a metallic core, e.g., Zuber et al., 2011) and radius of APB as 100 km (e.g., Weiss et al., 2008), and obtain the gravity of APB as ~ 0.11 m/s^2. Density of quenched angrites is estimated in the method of Lange (1994), and when the olivine density is decided as 3500 kg/m^3, I can estimate the density difference between olivine and the melt. Viscosity of the melt is estimated from Shaw et al. (1972). These parameters are compiled in Table 10. When I assume the time for olivine sinking as 100 hr, sinking distance is 20 ~ 60 cm (shown in Table 10). These values are not enough for olivine sinking. The igneous body of quenched angrites is assumed as eruption of lava flow in this model. It is considered that olivine sinking continued during one cycle of eruption, thus 100 hr of sinking time could be short estimation. It is difficult to determine the time scale of eruption, but if it is possible, the lower limit of the APB size can be constrained because gravity is the function of the APB size.

Table 10. Viscosity, density, olivine sinking velocity and olivine sinking distance (@100 hr) of quenched angrites.

	NWA 1296	NWA 7203	Sahara 99555	D'Orbigny	Asuka-881371	LEW 87051	NWA 1670	NWA 12774
Viscosity (Pa・S)	4.0	5.7	4.1	3.9	1.3	1.6	3.6	1.9
Density (g/cm^3)	3.3	3.3	3.3	3.3	3.4	3.2	3.2	3.2
Sinking velocity (10^{-6} m/s^2)	2.5	2.6	2.9	2.6	6.7	9.8	5.2	9.5
Sinking distance (m) @100 hr	0.2	0.2	0.2	0.2	0.4	0.6	0.3	0.6

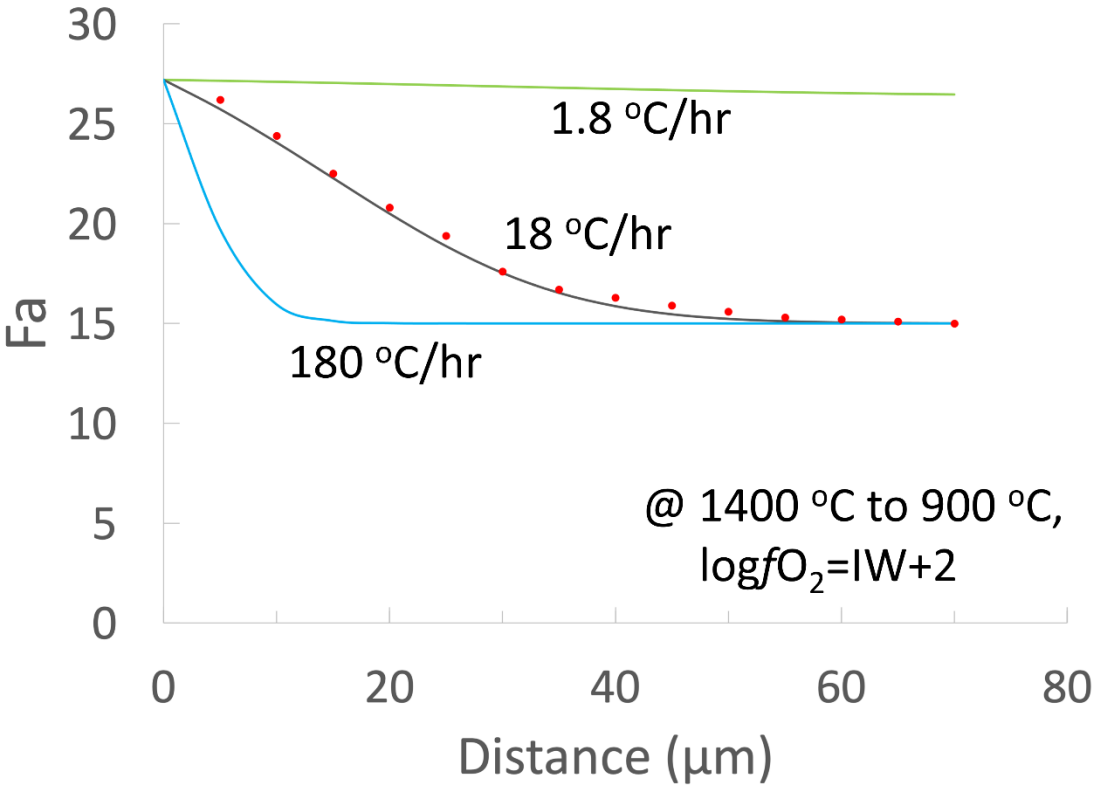

Fig. 86. Estimation for cooling rate of LEW 87051. The best-fit cooling rate is 18 °C/hr. Cooling rates of 1.8 °C/hr and 18 °C/hr are also shown for comparison.

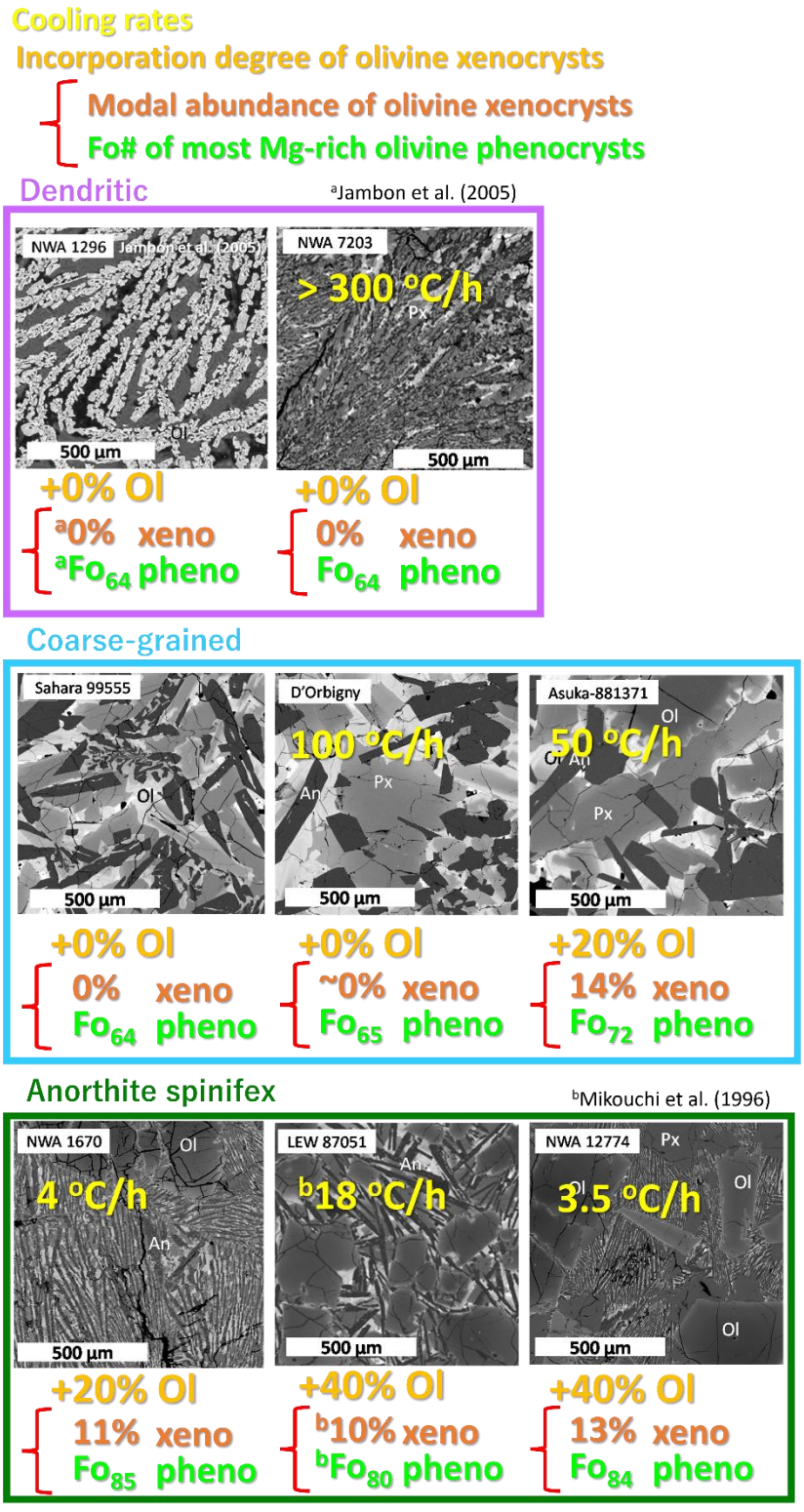

Fig. 87. Cooling rates of quenched angrites. Incorporation degree of olivine xenocrysts, modal abundances of olivine xenocrysts, and Fo# of most Mg-rich olivine phenocrysts for each quenched angrites are also shown. The BSE image of NWA 1296 taken from Jambon et al. (2005).

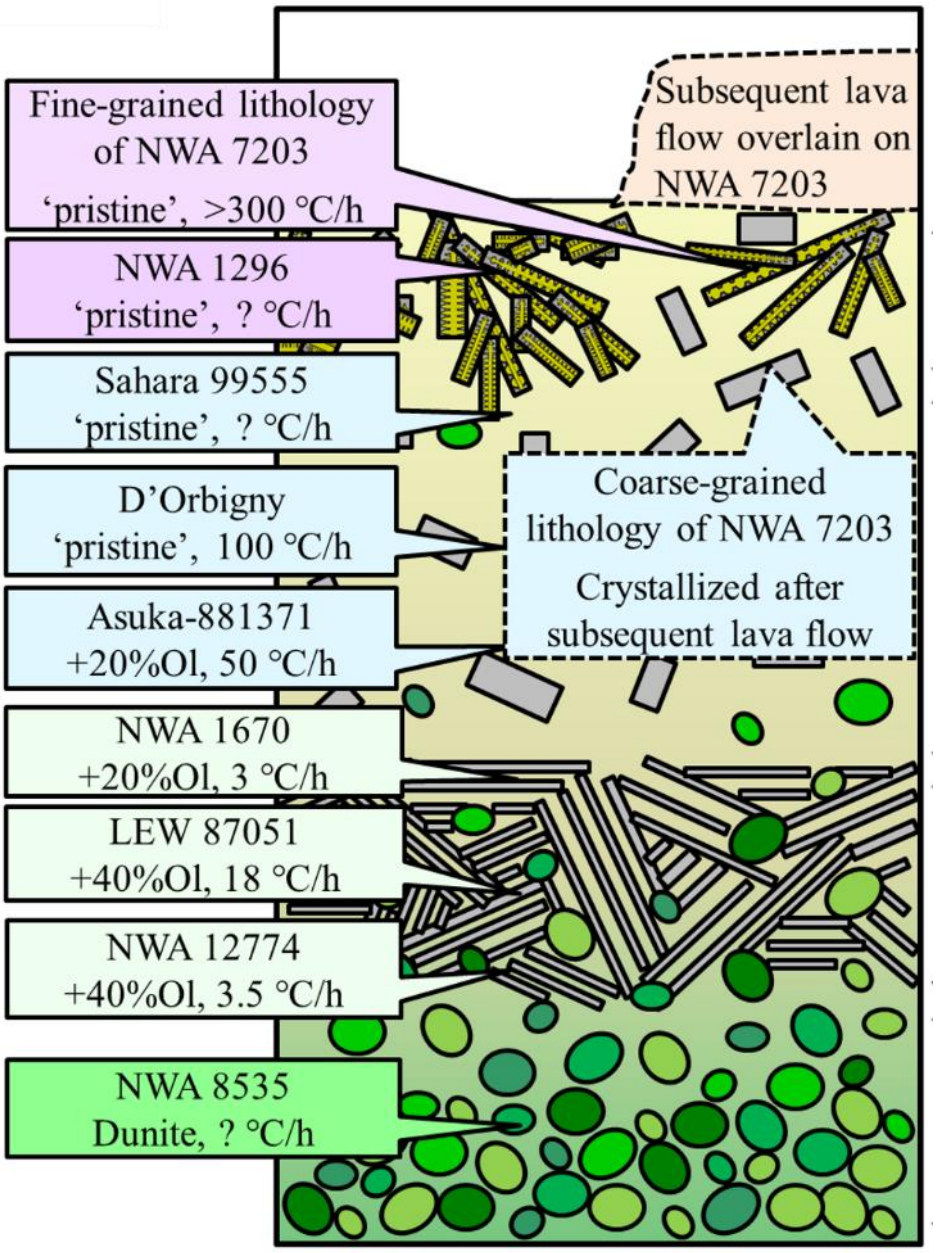

Fig. 88. Stratigraphy of the igneous body of quenched angrites. Cooling rates are faster near the surface and slower at a lower part, producing textural varieties. The bulk chemical compositions of the samples are pristine (Mg-poor and true parent melt composition) near the surface and Mg-rich at a lower part due to accumulation of the trapped mantle olivine xenocrysts by sinking in the igneous body.

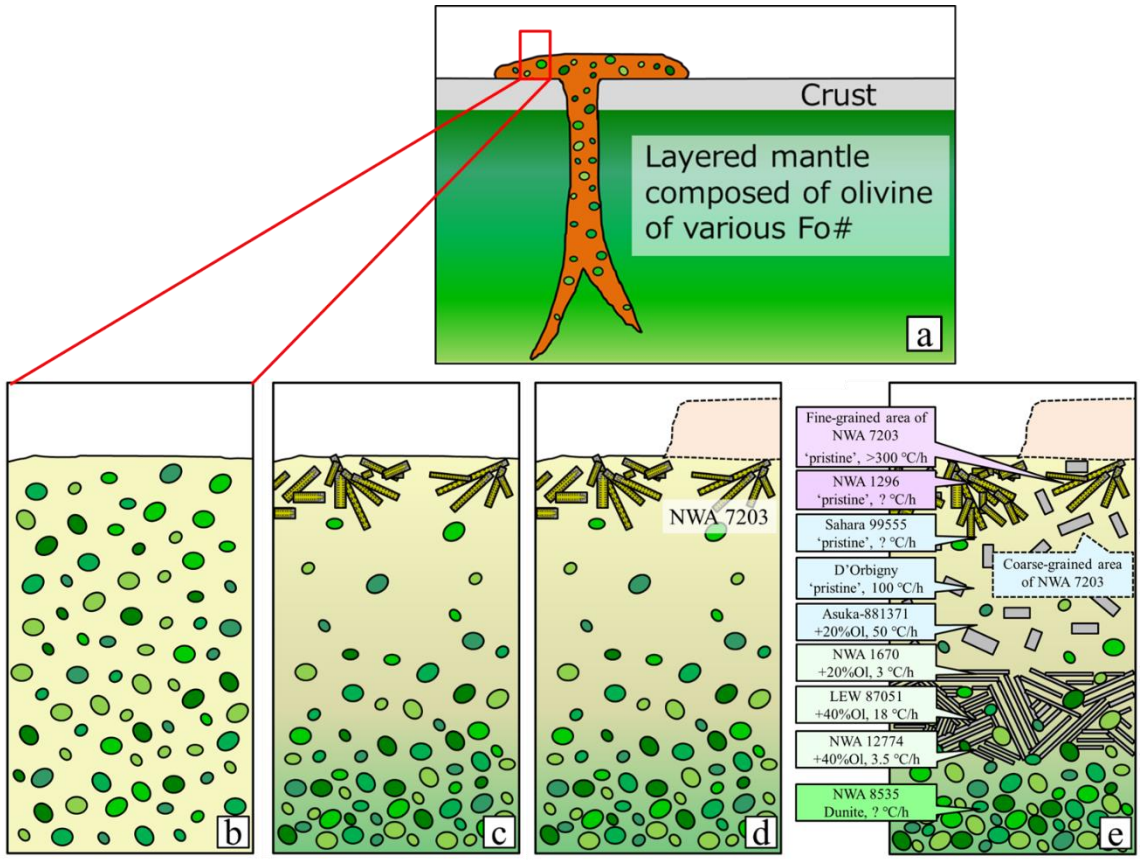

Fig. 89. Schematic illustration for the formation process of the igneous body of quenched angrites. (a) The parent melt was produced by the partial melting of the quenched angrite source. (b) A lava flow with Mg-rich olivine xenocrysts was erupted onto the surface of APB. (c) Rapid cooling of the lava flow and sinking and melting of olivine xenocrysts started. (d) Subsequent lava flow came and overlay on NWA 7203 in the middle of the crystallization. (e) Cooling rates were faster near the surface and slower at a lower part, producing textural varieties. Cooling rate change produced both fine-grained and coarse-grained areas of NWA 7203.

4.8. Comparison between quenched angrites and komatiites

The stratigraphy of the igneous body of quenched angrites suggested in this study is similar to that of terrestrial komatiites (Fig. 90, stratigraphy of komatiite after Pyke et al., 1973 is also shown). Most komatiites formed in Archean age on the surface of the earth, where high temperature (around 1600 ℃) komatiite magmas crystallized at rapid cooling rates (Arndt et al., 2008). Both quenched angrites and komatiites are Mg-rich rocks. In terms of bulk chemical compositions, quenched angrite is more Al-, Fe- and Ca-rich, and komatiite is more Mg-rich. Stratigraphy of the komatiite igneous body is suggested by Pyke et al. (1973) (Fig. 90). Textures vary according to the burial depth, classified into chilled flow top ("A1"), random spinifex ("A2"), plate spinifex ("A3"), foliated skeletal olivines ("B1") and cumulate olivine ("B2"). Stratigraphy of the igneous body of quenched angrites could be similarly divided into four types by igneous textures, and I will accordingly call them "QA1", "QA2", "QA3" and "QB" in the order from the top to bottom (Fig. 90).

The burial depth of LEW 87051 is estimated around 2 m (Mikouchi et al., 1995), and the layer thickness of komatiites is around 4 m (Munro Township, Ontario, Pyke et al., 1973), and thus layer thickness is generally similar. Layer thickness depends on the part of flow of komatiite. A thin pounded flow is ~2-10 m, a thick pounded flow is ~10-100 m, and a dynamic pathway is ~ 50-500 m (Arndt et al., 2008). The dynamic pathway is a rare part and extremely thick. The thick pounded flow crystallizes pyroxenite at the B zone and finally crystallizes eutectic gabbroic melt. Quenched angrites are most similar to a thin pounded flow in terms of its lithology. Quenched angrites often contain Mg-rich olivine xenocrysts. Renner et al. (1994) considered that Mg-rich olivine grains in Zimbabwe komatiites are xenocrysts, but olivine xenocrysts are not reported in other komatiites.

Cooling rates of komatiite are estimated by Faure et al. (2006) from experimental study (Fig. 91). They found that thermal gradient is important in relatively slow cooling rates and neglisible in fast cooling rates like upper parts of komatiite flows. They considered that the cooling rates of A1 is

>150 ºC/hr, A2 is >10 ºC/hr, and A3 is 2~5 ºC/hr, respectively. These cooling rates are comparable to those of quenched angrites.

In order to evaluate the validity to compare igneous bodies of quenched angrites and komatiites, I checked their physical conditions. The important factors to determine the characteristics of lava flow are chemical compositions, liquidus temperature, cooling rates and viscosity of the flow, and the gravity of the planetary body.

The chemical compositions and cooling rates of lava flows will decide the crystallization of mineral phases. Cooling rates of quenched angrites and komatiites are comparable as discussed above. However, chemical compositions of lava flows are different. Bulk chemical composition of quenched angrites is SiO_2 = ~40 wt%, Al_2O_3 = ~10 wt%, FeO = ~20 wt%, MgO = ~10 wt%, and CaO = ~15 wt%. On the other hand, bulk chemical composition of komatiites is SiO_2 = 40~50 wt% and MgO = 20~35 wt%, and Mg- and Si-rich compared from that of quenched angrites'. Such a bulk chemical composition of komatiites crystallizes only olivine in a wide range of temperature (Arndt et al., 2008). The bulk chemical composition of quenched angrites' firstly crystallizes olivine, but it will co-crystallize olivine and anorthite as crystallization proceeds. Thus, the same process of olivine crystallization and sinking of olivine occurs in the high temperature phase of lava flows of quenched angrite and komatiite, although the crystallized mineral phases are different in their low temperature phases.

Both liquidus temperatures of quenched angrites and komatiites are high, but komatiites' is higher (~1600 ºC, Arndt et al., 2008) compared to quenched angrites' (~1400 ºC, Mikouchi et al., 1994). Under the temperature near liquidus, both quenched angrites and komatiites have viscosity of several Pa・s (e.g., Williams et al., 2002). This similarity of viscosity between quenched angrites and komatiites produce the similarity of physical conditions. However, the gravity of the parent body is very different. The gravity of quenched angrites is estimated to be ~0.11 m/s^2 (see 4.7) and that of

terrestrial komatiites is 9.8 m/s^2. This difference could produce the eruption scale and olivine sinking. In the next paragraph, I will compare the sample of quenched angrites and komatiites and discuss the similarities and differences between quenched angrites and komatiites.

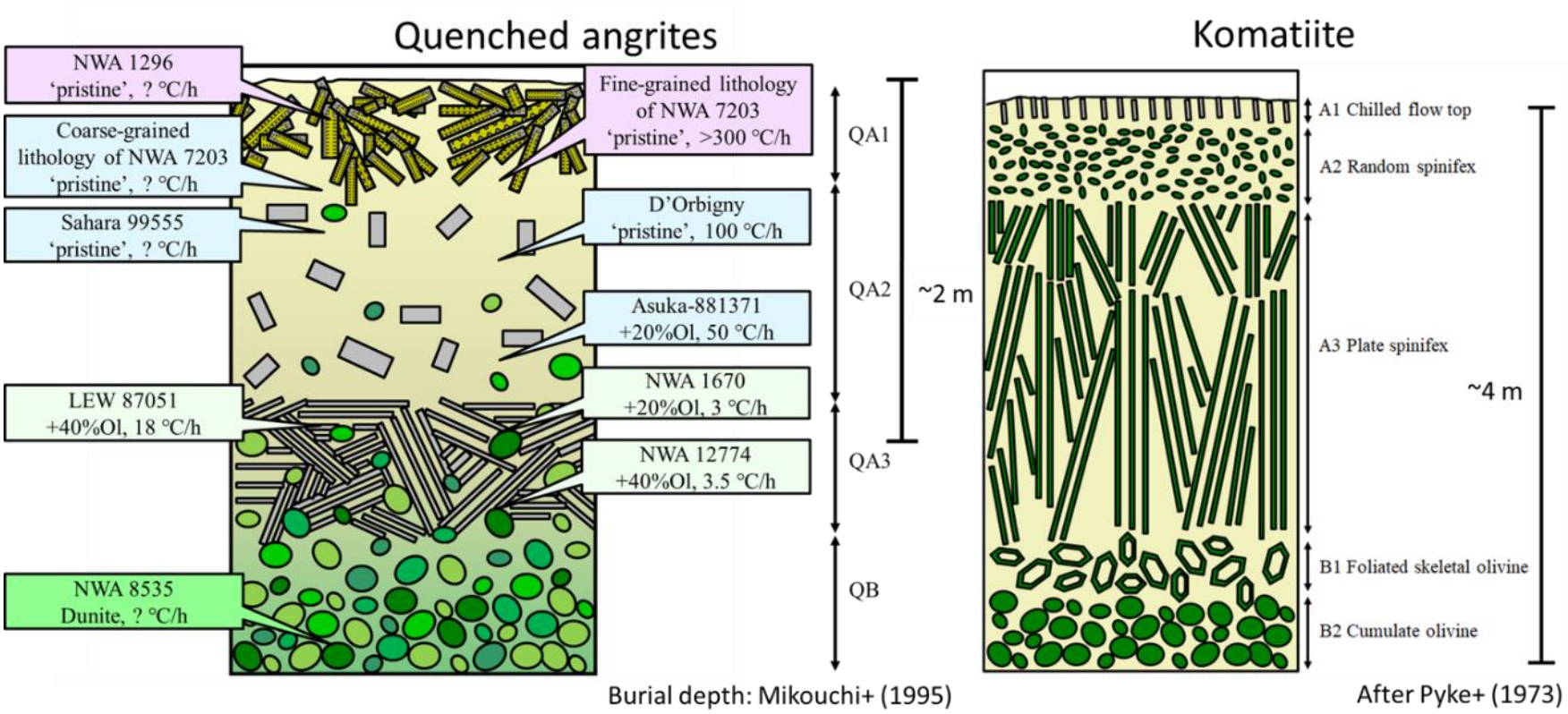

Fig. 90. Stratigraphic comparison between igneous bodies of quenched angrites and komatiites (after Pyke et al., 1973).

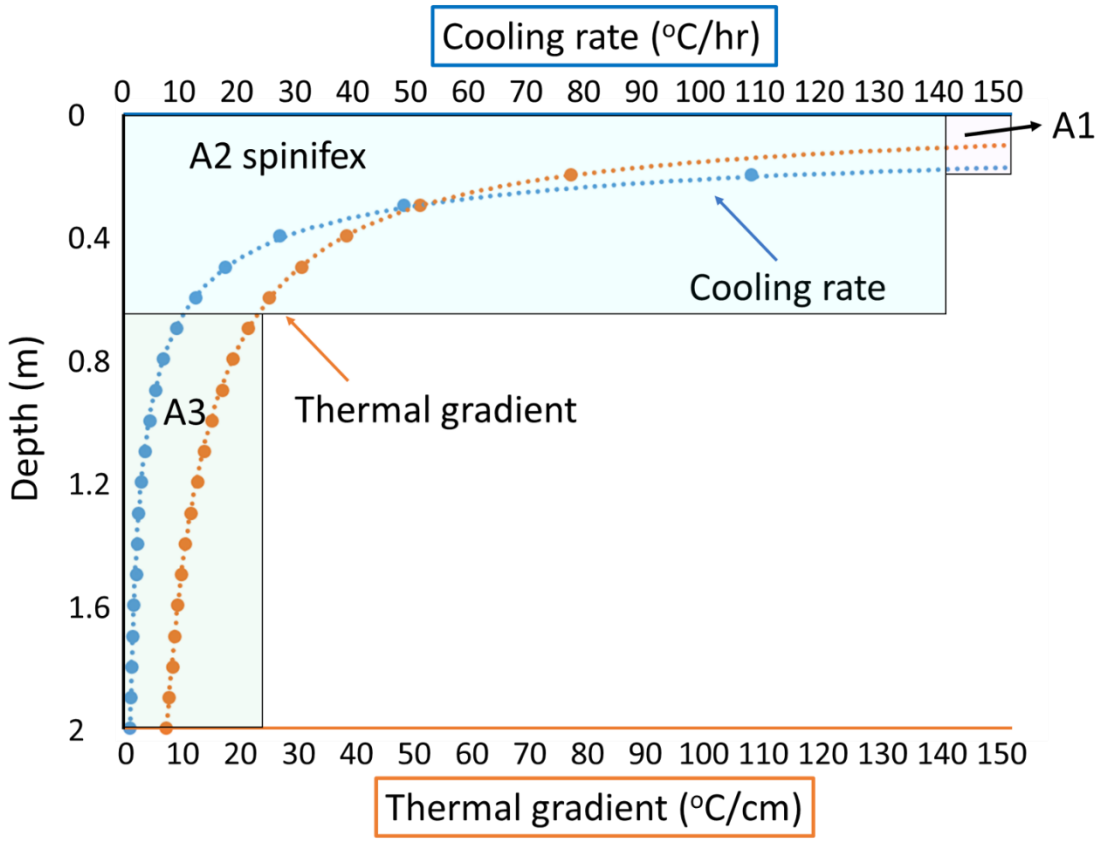

Fig. 91. Diagram illustrating changes in cooling rate and thermal gradient during the crystallization of the upper part of a komatiite flow (after Faure et al., 2006).

4.8.1. Comparison between QA1 of quenched angrites and A1 of komatiites

The QA1 samples of quenched angrites are NWA 1296 and NWA 7203. The cooling rate of the fine-grained lithology of NWA 7203 is estimated to be over 300 ^{o}C/hr, and it is considered to have the fastest cooling rates. Grain sizes of QA1 samples are several to a few hundreds μm for fine-grained lithology of NWA 7203 and 10 μm ~ for NWA 1296 (Jambon et al., 2005). Both QA1 samples show a dendritic texture consisting of olivine and anorthite intergrowth (Fig. 92). QA1 samples could be derived from the flow top of the igneous body of quenched angrites (Fig. 90).

A1 of komatiite is at chilled margins of the uppermost part of the komatiite igneous body (Fig. 90). A1 of komatiite shows the finest-grained texture among komatiites. The thickness of A1 is 5~150 cm (average 15 cm) (Arndt et al. 2008). A1 contains randomly oriented, elongate skeletal olivines and a variable amount of polyhedral olivine phenocrysts, set in a very fine-grained or glassy groundmass (Arndt et al. 2008). The cooling rate of A1 is over 150 ^{o}C/hr as estimated from crystallization experiment (Fig. 91, Faure et al., 2006).

When I compared QA1 of quenched angrites and A1 of komatiite, the finest grain size in each igneous body and very fast cooling rates are similar. In addition, both of them are considered to be an upper chilled margin. On the other hand, the different point is mineral assemblage. QA1 angrite show a dendritic intergrowth of olivine and anorthite, and pyroxene fills the gap of dendrites. A1 komatiite contains fine-grained olivine phenocrysts. This difference might be due to their different magma compositions. The bulk chemical compositions of QA1 of quenched angrites are more Ca- and Fe-rich and Mg-poor compared from A1 of komatiite. According to the phase equilibrium relationship of the angrite petrogenesis suggested by Longhi (1999), parent magma of quenched angrites first tends to crystallize olivine and anorthite, although the QA1 samples did not crystallize under equilibrium condition.

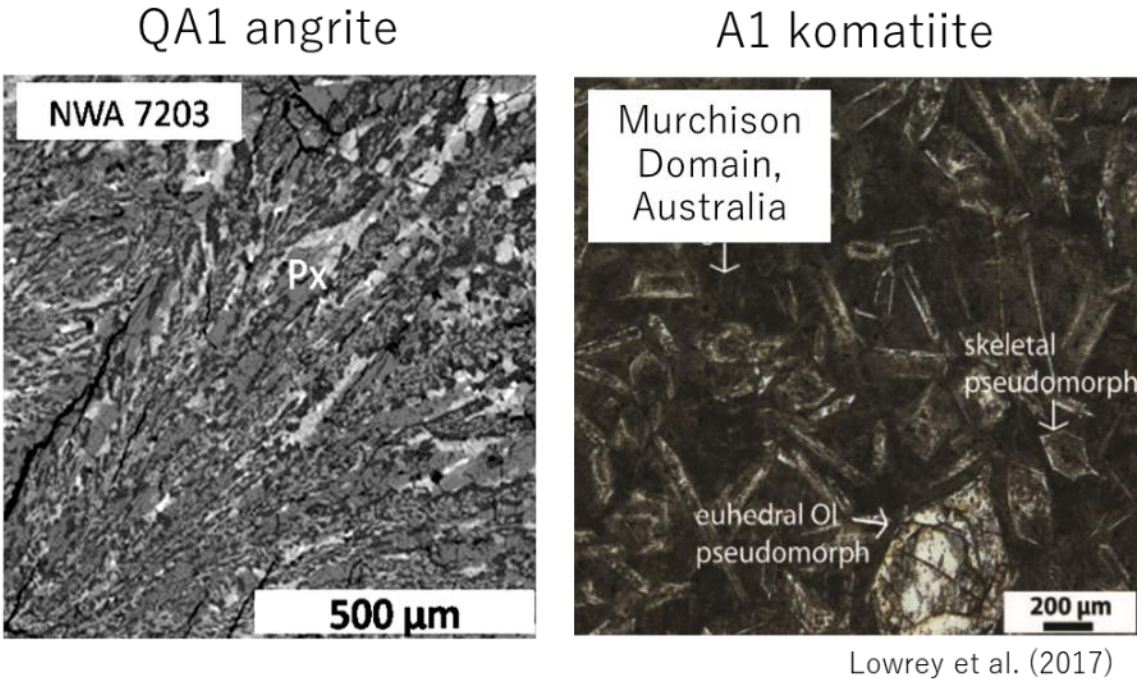

Fig. 92. Igneous textures of QA1 quenched angrite (left, NWA 7203) and A1 komatiite (right, Murchison Domain, Lowrey et al., 2017). The optical photomicrograph of A1 komatiite taken from Lowrey et al. (2017).

4.8.2. Comparison between QA2 of quenched angrites and A2 of komatiites

The QA2 samples of quenched angrites are coarse-grained lithology of NWA 7203, Sahara 99555, D'Orbigny and Asuka-881371. The cooling rate of the D'Orbigny is estimated to be 100 ^{o}C/hr and that of Asuka-881371 is estimated to be 50 ^{o}C/hr. Grain sizes of QA2 samples are ~2 mm for coarse-grained lithology of NWA 7203, ~1 mm for Sahara 99555, ~3 mm for D'Orbigny and ~1 mm for Asuka-881371. These QA2 quenched angrites show a relatively coarse-grained ophitic texture. The observations suggest that QA2 samples are derived from the layer below the flow top (Fig. 90).

A2 of komatiite is a random spinifex layer below the flow top (Fig. 90). A2 of komatiite contains minerals with random orientation. Skeletal olivine grains become visible, and these grains are a few mm long and about 0.5 mm thick (Arndt et al., 2008). Grain sizes are larger compared with A1 of komatiite. The matrix between olivine grains is composed of clinopyroxene, glass (always devitrified and commonly altered to secondary hydrous phases) and minor oxides (Arndt et al. 2008). The cooling rate of A2 is over 10 ^{o}C/hr from the crystallization experiment (Fig. 91, Faure et al., 2006).

When I compare QA2 of quenched angrites and A2 of komatiite, the random mineral orientation and cooling rates are similar (Fig. 93). On the other hand, mineral assemblage and mineral shapes are different. Mineral shapes are elongated in A2 of komatiite and relatively thick in QA2 of quenched angrites.

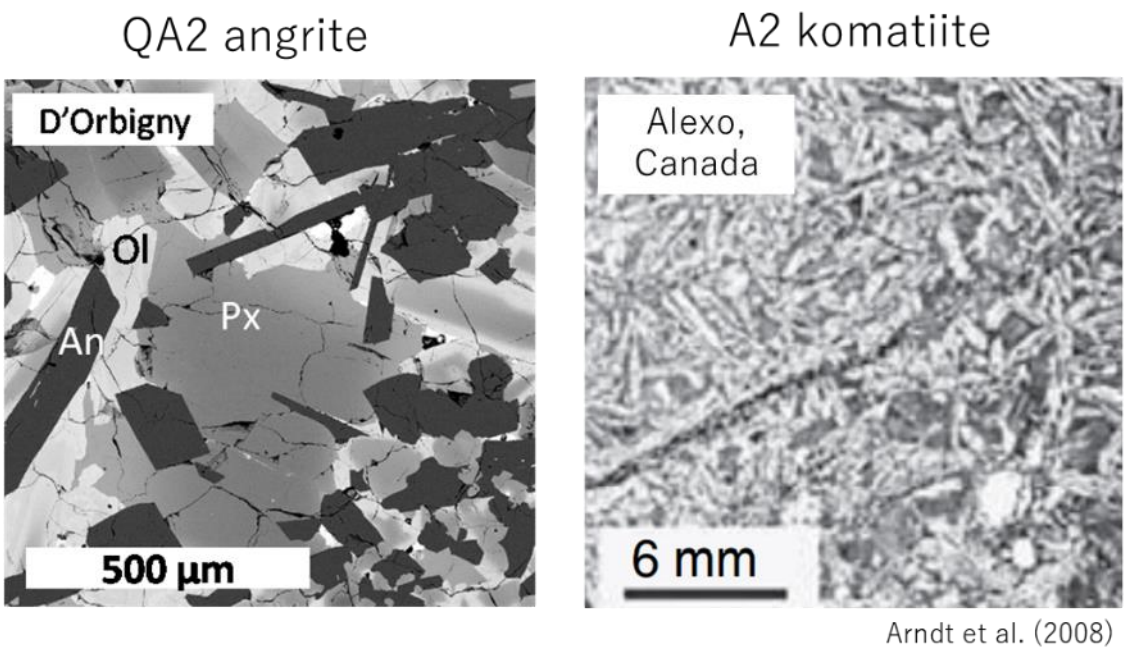

Fig. 93. Igneous textures of QA2 quenched angrite (left, D'Orbigny) and A2 komatiite (right, Alexo, Arndt et al., 2008). The optical photomicrograph of A2 komatiite taken from Arndt et al. (2008).

4.8.3. Comparison between QA3 of quenched angrites and A3 of komatiites

The QA3 samples of quenched angrites are LEW 87051, NWA 1670 and NWA 12774. The cooling rate of NWA 1670 is estimated to be 3 ^{o}C/hr and that of NWA 12774 is estimated to be 3.5 ^{o}C/hr. Grain sizes of QA3 anorthite are ~1 mm in length and ~10 μm (NWA 1670 and NWA 12774) or ~300 μm (LEW 87051) in width. These QA3 quenched angrites show an anorthite spinifex texture (Fig. 94). QA3 samples are possibly derived from a layer below the random spinifex layer (Fig. 90).

A3 of komatiite is a plate spinifex layer below the random spinifex layer (Fig. 90). In parallel with the increase in grain size, the orientation of the plate spinifex olivine changes from random to roughly perpendicular to the flow top. Deeper in the flow, the olivine grains become progressively larger and towards the base of some layers they form spectacular composite blades up to 1 m long (Arndt et al., 2008). The cooling rate of A3 is 2~5 ^{o}C/hr from crystallization experiments (Fig. 91, Faure et al., 2006).

Plate spinifex texture of olivine or pyroxene megacryst tends to be oriented perpendicular to the cooling front and crystallized at slow cooling of ultramafic magma in a thermal gradient (7–35 ^{o}C/cm) (Faure et al., 2006). This geometry arises because only vertically oriented crystals can grow downward into nutrient-rich liquid (Fig. 95, Arndt et al., 2008; Faure et al., 2006). Crystallization of such olivine megacryst is caused by unique property of komatiites of having such a very wide temperature interval (up to 460 ^{o}C) between liquidus and solidus, for a large part of which olivine (with minor chromite) is the only liquidus phase (Arndt et al., 2008). This potential is enhanced by the highly low viscosity, which facilitates rapid settling of any suspended olivine crystals. This has two effects: (1) it clears the melt in the upper part of the flow of nuclei, helping to delay crystallization and promote supercooling; and (2) it forms a blanket of olivine cumulates on the floor of the flow, which insulates the flowing lava from the cooler footwall rock (Arndt et al., 2008).

When I compared QA3 of quenched angrites and A3 of komatiite, the oriented minerals and cooling rates are similar (Fig. 94). On the other hand, mineral combinations and mineral sizes of spinifex textures are different. The oriented mineral in QA3 quenched angrites is anorthite, and that in A3 of komatiite is olivine. Anorthite spinifex in QA3 of quenched angrites is ~1 mm long and A3 of olivine spinifex in komatiite is ~1 m long. The biggest difference between angrite and komatiite is the bulk composition. This difference causes the difference of crystallization phase and temperature interval between liquidus and solidus. Vertically oriented olivine crystals grow exclusively in komatiite because of its large temperature interval of the only olivine liquidus phase. Compared with komatiite, the quenched angrite system does not crystallize only olivine liquidus phase over a wide range of temperature, and temperature interval of liquidus and solidus is not as large as that of komatiite. This might be a reason that anorthite spinifex in QA3 of quenched angrites cannot grow greater than ~1 mm in length. Alternatively, there is a possibility that QA3 of quenched angrites found until now is biased in sampling and just happened that these samples did not contain any large crystals. QA3 of quenched angrites are 0.6 g for LEW 87051, 29 g for NWA 1670 and 454 g for NWA 12774 (Meteoritical Bulletin), and large QA3 samples of quenched angrite have not been found until now.

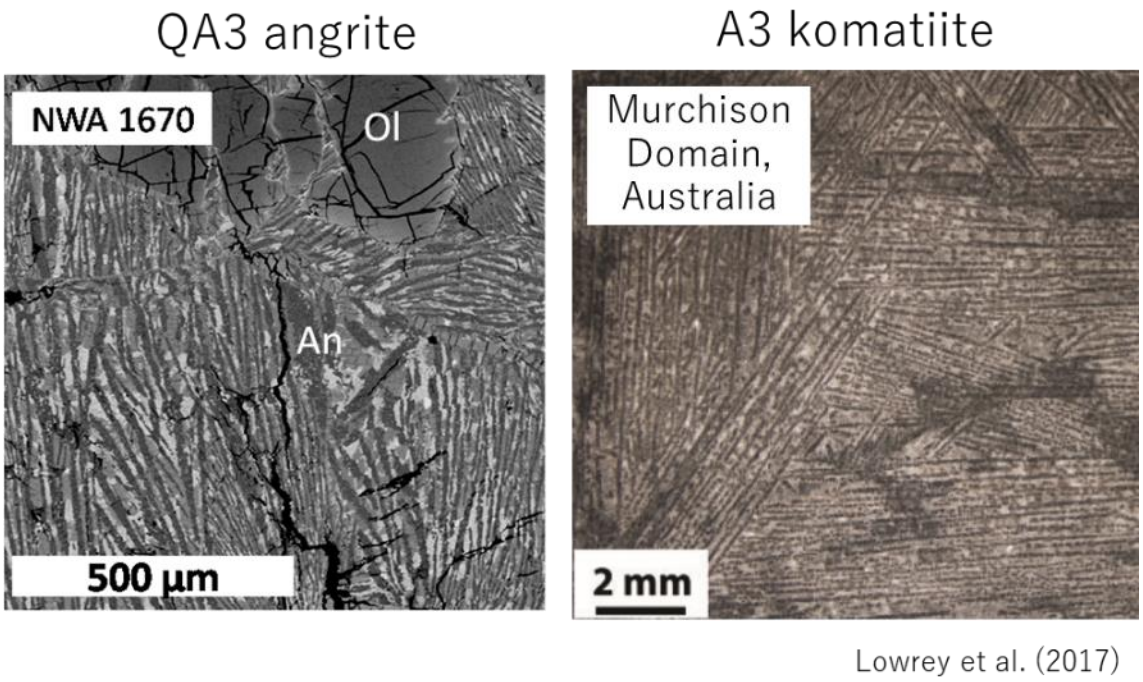

Fig. 94. Igneous textures of QA3 quenched angrite (left, NWA 1670) and A3 komatiite (right, Murchison Domain, Lowrey et al., 2017). The optical photomicrograph of A3 komatiite taken from Lowrey et al. (2017).

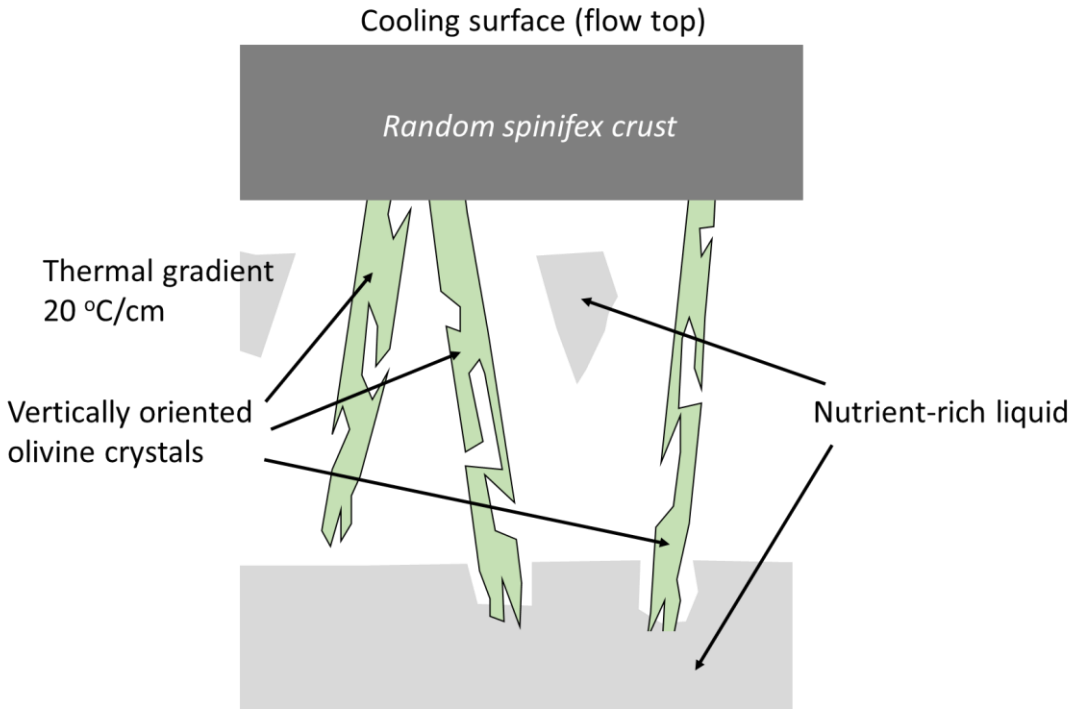

Fig. 95. Cartoon showing the various processes which have been postulated to operate during the development of spinifex textures (after Faure et al., 2008).

4.8.4. Comparison between QB of quenched angrites and B (B1 and B2) of komatiites

NWA 8535 is distinctive from the other quenched angrites. NWA 8535 might be a cumulate (Santos et al., 2016a), and this might correspond to QB samples of quenched angrites. NWA 8535 contains spinel between olivine grains which is ~several hundreds μm in size, and Cr# (Cr/Cr + Al) of the spinel has a large range (Santos et al., 2016b). This characteristic of spinel is similar to that in NWA 12774 (see 3.1.6.). In 4.4., I consider that these Cr-rich spinel crystallized at the end of the crystallization process and sunk with olivine xenocrysts. This is consistent with the view that NWA 8535 is a cumulate. Thus, the QB quenched angrite NWA 8535 could be derived from the bottom of the igneous body (Fig. 90).

B (B1 and B2) of komatiite is a cumulate layer below the A (A2 and A3) spinifex layers (Fig. 90). The B1 layer is made up of elongate hopper olivine phenocrysts, typically 1–3 mm long (Arndt et al., 2008). B1 layers in Archean komatiites are only 2–5 cm thick and they are absent from many layered komatiite flows and appear restricted to those exhibiting the most pronounced differentiation into spinifex and cumulate layers (Arndt et al., 2008). B2 layer is made up to weak to moderately foliated, fine- to medium-grained, medium gray weathering peridotite (Pyke et al., 1973). In some flow units a knobby weathering layer (B3) occurs within the lower part of the B zone (Pyke et al., 1973).

When I compared QB of quenched angrites and B of komatiite, both of them are peridotite with cumulate textures. Although the cooling rate of QB is unclear, there is a possibility that NWA 8535 corresponds to the B cumulate zone of komatiite. I consider the existence of NWA 8535 strengthens the hypothesis that quenched angrite experienced a crystallization process similar to komatiite. Analyzing this angrite is necessary to conclude this hypothesis, which was not possible in this study because the sample was not available.

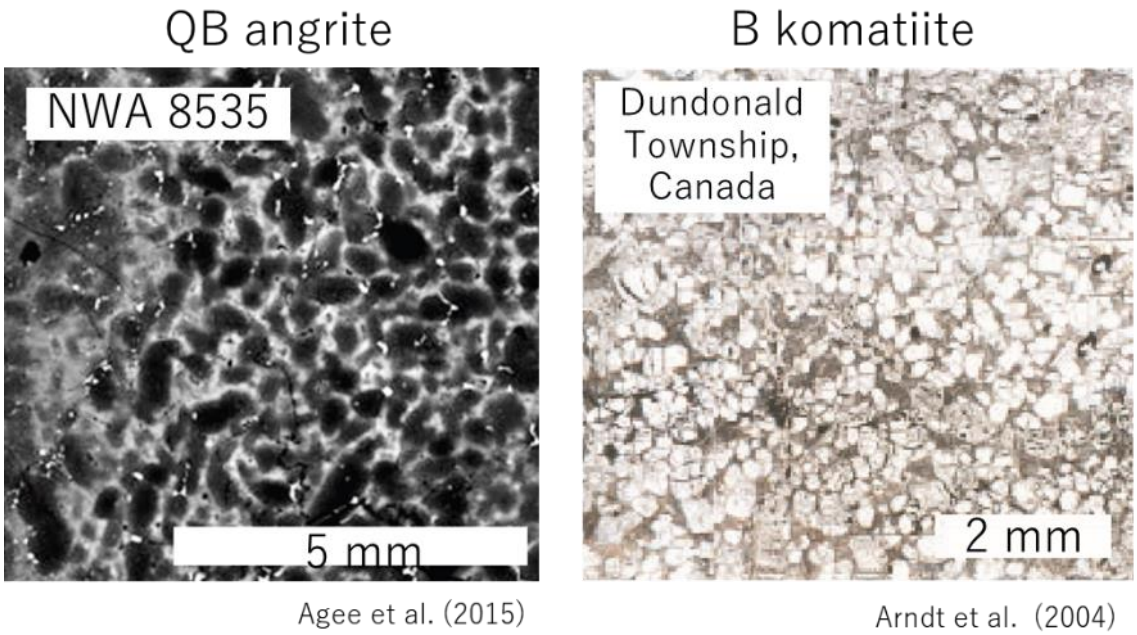

Fig. 96. Igneous textures of QB angrite (left, NWA 8535, Agee et al., 2015) and B komatiite (right, Dundonald Township, Arndt et al., 2004). The BSE image of NWA 8535 and the optical photomicrograph of B komatiite taken from Agee et al. (2015) and Arndt et al. (2004), respectively.

4.9. Geological settings of komatiite and quenched angrites

As I discussed above, I found some stratigraphic similarities between quenched angrites and komatiites for their igneous bodies (see 4.8.). This might indicate that the formation process of quenched angrites is similar to that of komatiites, although the chemical compositions of the magmas and presence of Mg-rich olivine xenocrysts are different. Hill et al. (1995) suggested the geological settings of komatiites as continuous eruption from fissure (Fig. 97, after Hill et al., 1995). Lava flow is continuous closer to the eruption site and episodic far from the eruption site. Sheet flow is continuous near the eruption site representing the maximum effusion rates, and distal lava-plain facies formed by episodic channel switching. The overall scale and relative proportions of sheet flow, channelized flow and lava-plain facies strongly depend upon the volume and rate of eruption (Hill et al., 1995). Schematic cross sections showing the lateral distribution of rock types of komatiites far from the eruption site are shown in Fig. 98 (Hill et al., 1995).

At the surface of APB, a similar eruption event might have occurred. The NWA 7203 quenched angrite contains a fine-grained dendritic area and a coarse-grained texture containing anorthites with random orientations (Fig. 36), which was caused by cooling rate change during crystallization (see 4.1.). Taking NWA 7203 into consideration, quenched angrites known until now might originate from an igneous body far from the eruption site. This is because textural difference of NWA 7203 could be produced by cooling rate change, and such cooling rate change occurs when a new breakout of lava flow overlay the earlier surface in a single eruption cycle. This event often occurs far from the eruption site.

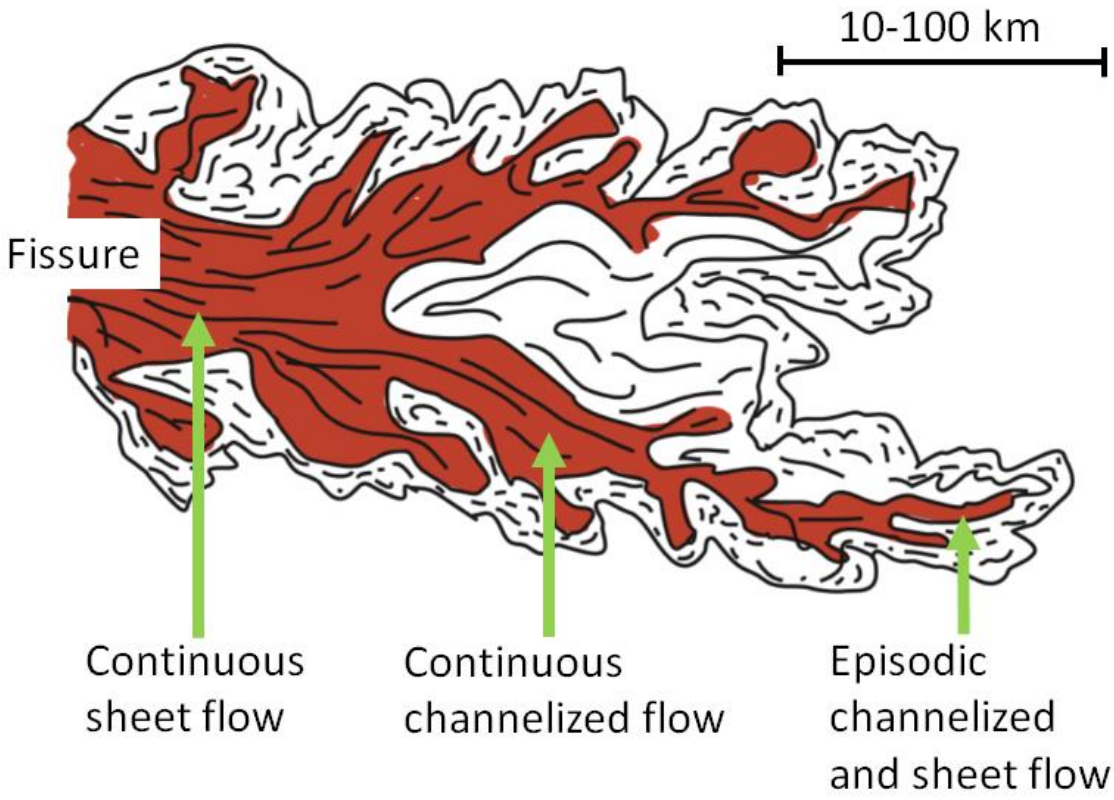

Fig. 97. Schematic illustration of geological settings of komatiites (continuous eruption from fissure) after Hill et al. (1995). Lava flow is continuous closer to the eruption site and episodic far from the eruption site.

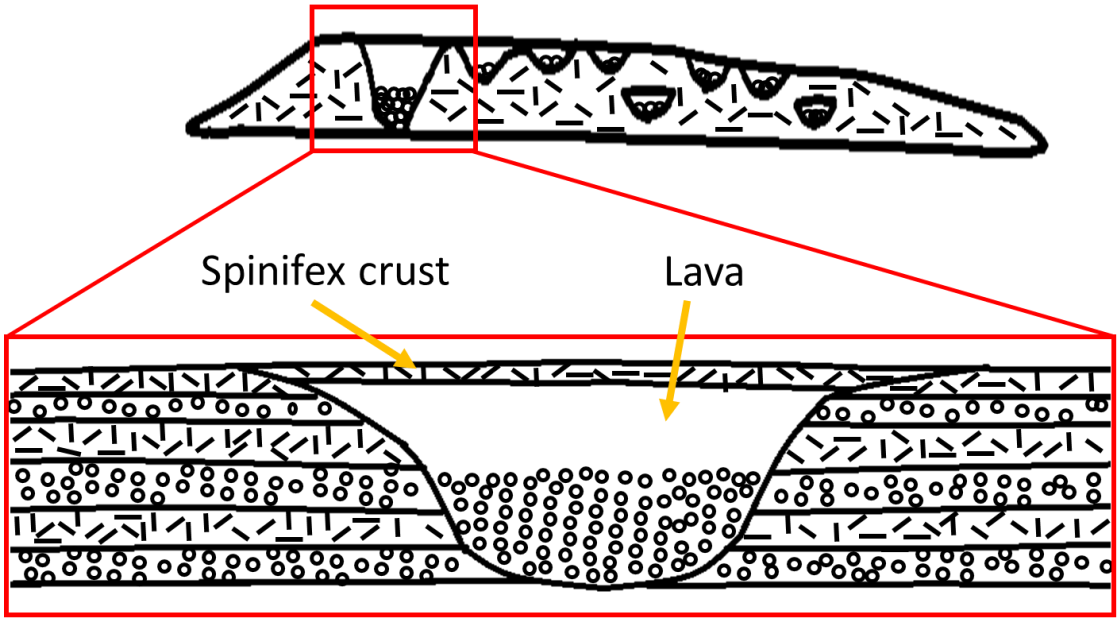

Fig. 98. Schematic cross sections showing the lateral distribution of rock type of komatiite far from the eruption site (after Hill et al., 1995).

4.10. Impacts and evolutional history of the APB

In the 1.3., I Introduced several studies estimating the size of APB. When combined the previous studies, the current best size estimate of APB is 150-1600 km in diameter.

Bogard (1995) suggested the proportion of impacted or heated samples in meteorites increases with the size of parent body. Scott and Bottke (2011) provided two reasons for this: (1) a small body can lose materials more easily than a large body because of the small escape velocity, and (2) the larger the size of a parent body, the more energy is needed to destroy the parent body (Asphaug 2009), and the probability of such a collision is lower. Thus, Scott and Bottke (2011) argued that the angrite parent asteroids should have become small (less than 10 km in diameter) before the timing of the LHB and escaped shock metamorphism during the LHB, in agreement with the observation that the majority of angrites have no shock textures. They proposed that the original APB was large (at least 100 km in diameter) and a major impact on it occurred ~4.5 Gyr ago, producing angritic daughter asteroids (Fig. 99). They argued that breccia formation and shock occurred predominantly after the destruction of their parent asteroids in family forming impacts, and thus most angrites lack shock textures caused by the destruction.

However, twenty-one angrites are found to date and NWA 1670 and NWA 7203 show clear evidence for shock metamorphism as I found in this study. Two out of twenty-one is a substantial proportion, which implies that shock metamorphism was more important in angrite asteroids than previously thought (Scott and Bottke, 2011). Some angrites might remain as one or more large asteroid(s) (>10 km in diameter) during LHB (Fig. 99). 3800 ± 440 Ma of Ar-Ar age of NWA 7203 suggested by Takenouchi et al. (2019) might correspond to the shock event during LHB. Alternatively, there is a possibility that shocked angrites are indeed suffered from local shock metamorphism.

Burbine et al. (2001) and Burbine et al. (2006) reported that the reflectance spectra of 289

Nenetta (37.6 km in diameter: Masiero et al. 2012) and 3819 Robinson (10.3 km in diameter: Masiero et al. 2012) showed relatively good agreement with that of D'Orbigny, suggesting that these asteroids can be one of the angrite asteroids, in agreement with the hypothesis of large angrite asteroids.

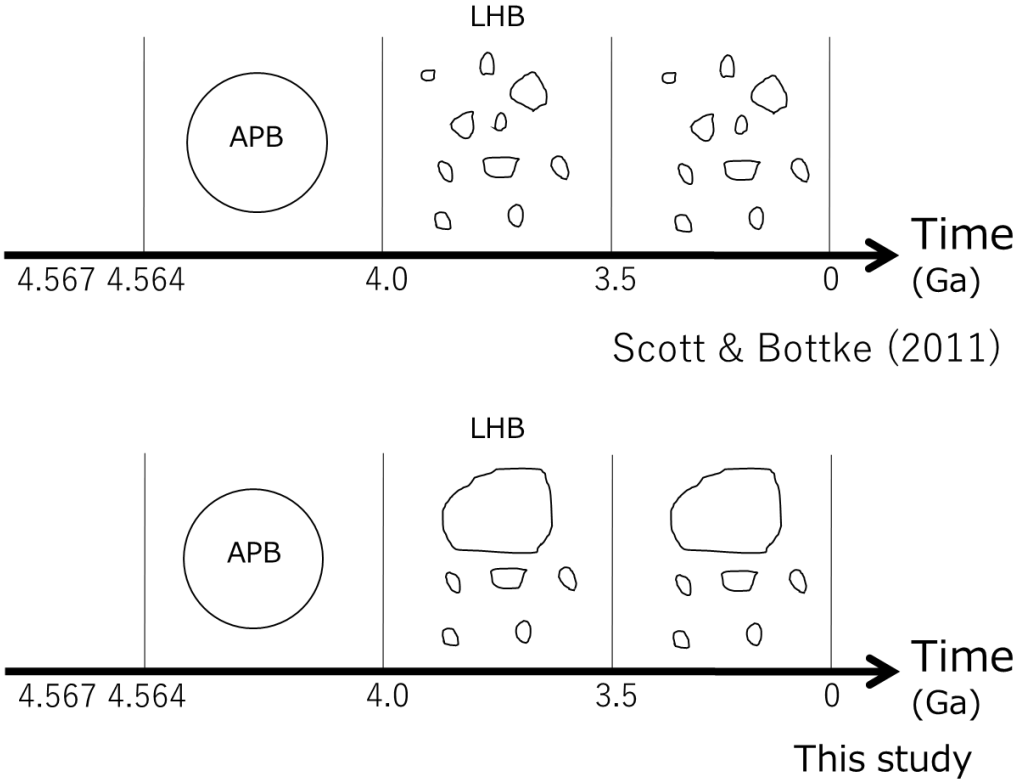

Fig. 99. Schematic illustrations of impacts and evolutional history of the APB suggested by Scott and Bottke (upper figure) and this study (lower figure). Scott and Bottke (2011) proposed that the original APB was large (at least 100 km in diameter) and a major impact on it occurred ~4.5 Gyr ago, producing angritic daughter asteroids. It is considered in this study that some angrites might remain as one or more large asteroid(s) (>10 km in diameter) during LHB.

4.11. Crystallization process and shock history of ancient igneous rocks in the solar system

Quenched angrites have older crystallization ages compared from other achondrite groups (see 1.2.). However, a new ungrouped achondrite, Erg Chech (EC) 002 was found in 2020 whose crystallization age is slightly older than quenched angrites' (Barrat et al., 2021). Although the small number of such old achondrites found until now, I try to generalize the crystallization process and shock history of ancient igneous rocks in the early solar system. If more numbers of old achondrites are found in the future, crystallization process and shock history of ancient igneous rocks in the solar system will become more apparent. Aubrites, ureilites and HEDs have old crystallization ages comparable to that of angrite (see 1.2.). However, these achondrites show high proportion of shocked samples, and thus it is not the best sample in order to consider the primary crystallization process of planetesimals in the early solar system.

EC 002 is an andesitic achondrite whose ^{26}Al-^{26}Mg age is 4565.0 Ma (i.e., 2.255 ± 0.013 Myr after formation of CAIs) (Barrat et al., 2021). Optical photomicrograph of EC 002 is shown in (Fig. 100). EC 002 contains angular to rounded orthopyroxene xenocrysts with chemically homogeneous cores (Mikouchi and Zolensky, 2021). Cooling rates can be estimated from atomic diffusion profiles recorded in clinopyroxene xenocrysts and reported as 1 ^{o}C/yr (from 1200 ^{o}C to 800 ^{o}C, Mikouchi and Zolensky, 2021) or 5 ^{o}C/yr (from 1200 ^{o}C to 1000 ^{o}C, Barrat et al., 2021). Barrat et al (2021) considered that remnants of primordial andesitic crust are rare in the meteorites although it is easy to generate andesite melts by partial melting of ordinary H or LL chondrites (Fig. 101, after Lunning et al., 2017). Such andesitic bodies are also rare today in the asteroid belt, suggesting that the earliest differentiated planetesimals that populated the solar system, as well as most of their debris, were certainly destroyed or subsequently accreted to the later growing rocky planets, making the discovery of meteorites originating from primordial crusts an exceptional occurrence.

EC 002 has an old crystallization age, relatively fast cooling rate and large xenocrysts with

chemically homogeneous cores, whose characteristics are similar to the cases of quenched angrites, although bulk chemical compositions are quite different. I agree that there are few samples to generalize the evolutional history of planetesimals in the early solar system, but it is possible that the characteristics of fast cooling rates and existence of xenocrysts with homogeneous cores such as quenched angrites and EC 002 might be common phenomena often seen in crusts of planetesimals in the early solar system. In addition, planetesimals in the early solar system might often undergo the evolutional process that they were either destroyed or incorporated into other bodies, as considered in quenched angrites and EC 002.

The results of this study suggest that similar mineralogical and petrological approaches will be possible to analyze slowly-cooled angrites, which will further allow to clarify the relationship between these two angrite subgroups. The large difference of crystallization ages (~6 Ma) between quenched and slowly-cooled angrites might be the key of evolutional history of APB, which suggests long continuing igneous activity. Clarification of the petrogenetic and mineralogical relationship between quenched and slowly-cooled angrites will then brighten the image of APB and differentiated planetesimals in general in the early solar system.

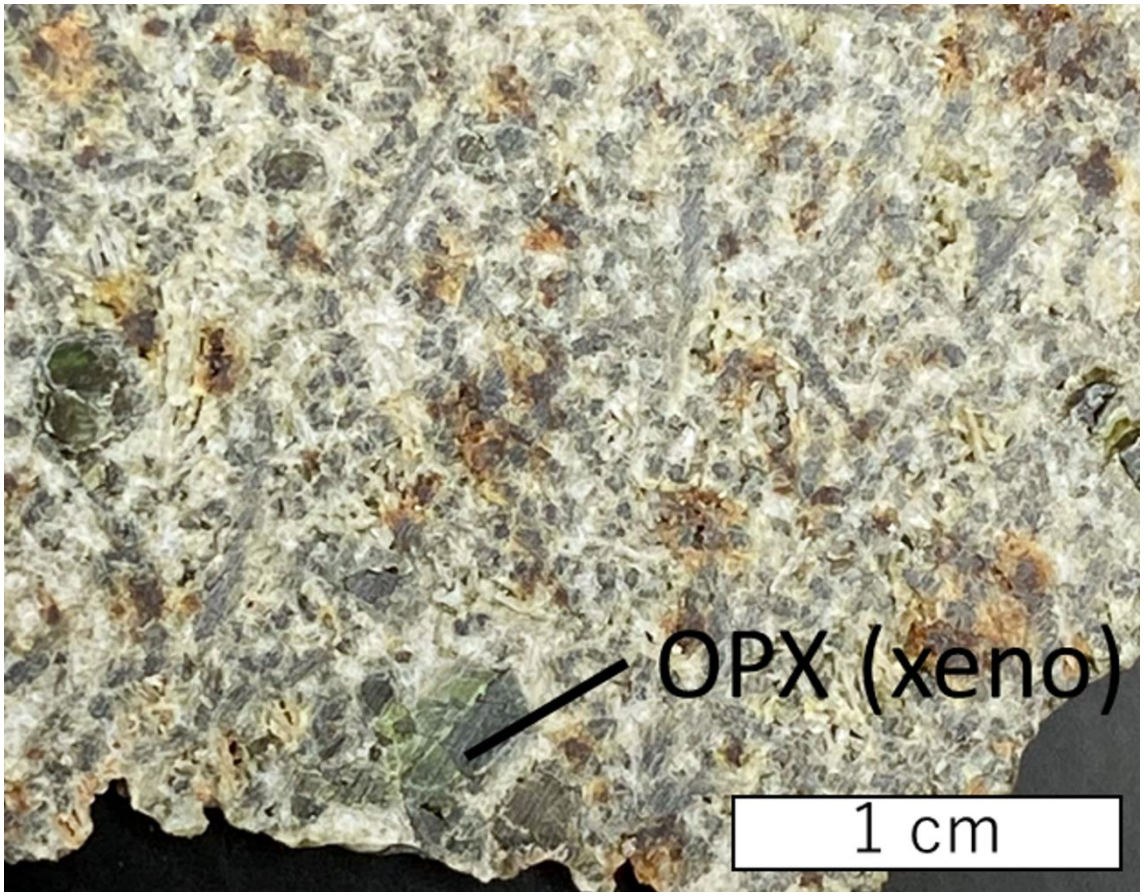

Fig. 100. Optical photomicrograph of a slice of EC 002. EC 002 contains angular to rounded orthopyroxene xenocrysts with chemically homogeneous cores (Mikouchi and Zolensky, 2021).

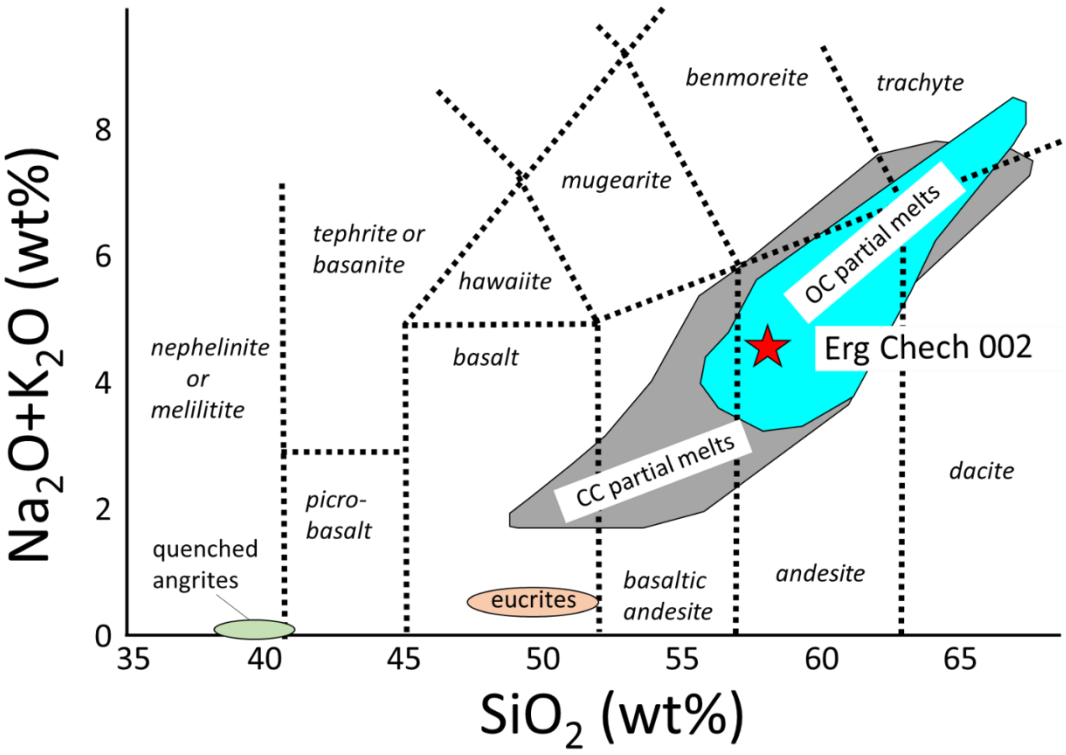

Fig. 101. Na_2O+K_2O *vs.* SiO_2 content of bulk chemical compositions for EC 002, eucrites and quenched angrites, and partial melt of carbonaceous chondrite (CC) and ordinary chondrite (OC) (after Barrat et al., 2021; Lunning et al., 2017).

5. Summary

1. NWA 7203 exhibits two distinct textures whose grain sizes vary from fine (~10 μm) to coarse grained (~3 mm) in contrast to other quenched angrites that show single textures. The cooling rate of NWA 7203 is estimated to be >300 ^{o}C/hr in the fine-grained lithologies and on the order of 1 or 10 ^{o}C/hr ^{o}C/hr in the coarse-grained lithologies. One of the possible scenarios to explain the change of cooling rate from fast to slow, is that NWA 7203 records cooling variations of a single eruption cycle in which a lobe of quenching basalt is overridden by a new breakout of lava from the main flow.
2. Unlike most angrites, NWA 7203 shows clear evidence for shock metamorphism. Anorthite close to shock veins becomes amorphous as indicated by broad Raman peaks, and in most parts, anorthites are still crystalline. From this observation, I infer that the shock pressure of NWA 7203 was under 20 GPa in spite of the presence of clear shock textures. The finding of clear shock metamorphism of NWA 7203 as well as NWA 1670 suggests that some angrites might have remained as one or more large asteroids (> 10 km in diameter) during late heavy bombardment.
3. Bulk chemical compositions of quenched angrites have clear correlations for certain major elements (e.g., Mg, Fe, Ca, Al), and the trends can be explained by incorporation of Mg-rich olivine xenocrysts. The amounts of incorporated olivine xenocrysts are estimated about 0 % for NWA 1296, Sahara 99555, NWA 7203 and D'Orbigny (considered as 'pristine angrite magma'), 20 % for Asuka-881371 and NWA 1670, and 40 % for LEW 87051 and NWA 12774.
4. Quenched angrites except NWA 8535 show three kinds of textures: dendritic, relatively coarse-grained, and anorthite spinifex. NWA 8535 might be a cumulate. These textural varieties are considered to be caused by the difference of cooling rates in a common igneous body,

corresponding to the different burial depth of each sample.

5. Oxygen isotopic ratios of olivine xenocrysts in NWA 12774 are identical to AFL, indicating that olivine xenocryst in NWA 12774 crystallized in APB, not in other asteroidal sources. Olivine xenocrysts in quenched angrites show large crystals (~ mm), have homogeneous cores with various Fo# and Ca and Cr contents, which are most likely to come from the APB mantle.
6. I propose that quenched angrites came from a single igneous body where bulk chemical compositions and cooling rates change depending on burial depth. The scenario is as follows; The parent melt was produced by partial melting of the quenched angrite source. Then, a lava flow with Mg-rich olivine xenocrysts was erupted onto the surface of the APB. Rapid cooling of the lava flow and sinking and melting of olivine xenocrysts started. Subsequent lava flow came and overlay on NWA 7203 in the middle of the crystallization. Finally, crystallization completed with faster cooling rates near the surface and slower cooling rates at a lower part.
7. Stratigraphy of the igneous body of quenched angrites suggested in this study is similar to that of komatiites in textural varieties and cooling rates. Geological settings of komatiite are considered as continuous eruption from fissure. Similar eruption event might have occurred at the surface of the APB. Taking NWA 7203 into consideration, quenched angrites known until now might originate from an igneous body far from the eruption site because its textural difference could be produced by cooling rate change when subsequent lava flow overlay the earlier surface, and such event often occurs far from the eruption site.
8. EC 002 is a new achondrite which is slightly older than quenched angrites. EC 002 shows a relatively fast cooling rate and has pyroxene xenocrysts with homogeneous cores. The parent body of EC 002 was certainly destroyed or subsequently accreted to the growing rocky planets. The characteristic similarities of fast cooling rates and existence of xenocrysts with homogeneous cores might be commonly seen in crusts of planetesimals in the early solar system,

implying that differentiated planetesimals in the early solar system might often undergo the evolutional process (destroyed or incorporated into other bodies) as found in quenched angrites and EC 002.

Acknowledgement

I would like to express my sincere gratitude to Prof. T. Mikouchi for discussing the data and writing this thesis. Technical advice from Mr. H. Yoshida and Mr. K. Ichimura for using EPMA was helpful. Discussion with Dr. T. Iizuka was highly beneficial. I thank NIPR members for helping Raman works and other observations of angrites as co-research fellows. My research would not have been complete without the help by collaborators. I thank Dr. P. Changkun and Mr. K. Nak Kyu for their help for analysis of oxygen isotopic ratios, and Prof. Y. Sano and Dr. N. Takahata for their help for analysis of Pb isotopic ratios, and Prof. H. Kagi for his help for analysis using micro-Raman. Thankfulness also goes to Drs. A. Yamaguchi, A. Takenouchi, and Prof. M. Bizzarro by stimulating discussions. My research would not have been possible without their help.

References

Amelin Y. 2008a. U–Pb ages of angrites. *Geochimica et Cosmochimica Acta* 72:221-32.

Amelin Y. 2008b. The U–Pb systematics of angrite Sahara 99555. *Geochimica et Cosmochimica Acta* 72:4874-4885.

Amelin Y., Iizuka T., and Huyskens M. 2011. Mineral chemistry of angrite NWA 4590, and its potential use for intercalibration of isotopic chronometers (abstract #2542). 42nd Lunar and Planetary Science Conference (CD-ROM).

Arndt N. T., Lesher C. M., Houlé M. G., Lewin E., and Lacaze Y. 2004. Intrusion and crystallization of a spinifex-textured komatiite sill in Dundonald Township, Ontario. *Journal of Petrology*, 45, 2555–2571

Arndt N. T., Lesher C. M., and Barnes S. J. 2008. *Komatiite*. Cambridge, UK: Cambridge University Press.

Asphaug E. 2009. Growth and evolution of asteroids. *Annual Review of Earth and Planetary Science* 37:413-448.

Barrat J. A., Chaussidon M., Yamaguchi A., Beck P., Villeneuve J., Byrne D. J., Broadley M W., and Marty B. 2021. A 4,565-My-old andesite from an extinct chondritic protoplanet. *Proceedings of the National Academy of Science* 118:1-7.

Bischoff A., Clayton R. N., Markl G., Mayeda T. K., Palme H., Schultz L., Srinivasan G., Weber W. H., Weckwerth G., and Wolf D. 2000. Mineralogy, chemistry, noble gases, and oxygen-and

magnesium-isotopic compositions of the angrite sahara 99555. *Meteoritics & Planetary Science* 35 (Supplement):A27.

Bogard D. D. 1995. Impact ages of meteorites: A synthesis. *Meteoritics* 30:244-268.

Brennecka G. A., and Wadhwa M. 2012. Uranium isotope compositions of the basaltic angrite meteorites and the chronological implications for the early Solar System. *Proceedings of the National Academy of Science* 109:9299-9303.

Burbine T. H., McCoy T. J., and Binzel R. P. 2001. Spectra of angrites and possible parent bodies (abstract #1857). 32nd Lunar and Planetary Science Conference (CD-ROM).

Burbine T. H., McCoy T. J., Hinrichs J. L., and Binzel R. P. 2006. Spectral properties of angrites. *Meteoritics & Planetary Science* 41:1139–1145.

Carter P. J., Leinhardt Z. M., Elliott T., Walter M. J., and Stewart S. T. 2015. Compositional evolution during rocky protoplanet accretion. *The Astrophysical Journal*, 813:72-88.

Chakraborty S. 2010. Diffusion Coefficients in Olivine, Wadsleyite and Ringwoodite. *Reviews in Mineralogy and Geochemistry* 72: 603-639.

Clayton R. N., and Kieffer S. W. 1991. Oxygen isotopic thermometer calibrations. In Taylor Jr. H. P., O'Neil J. R., and Kaplan I. R. (Eds.) *Stable isotope geochemistry: A tribute to samuel Epstein*. Washington DC, USA: The Geochemical Society, 3-10.

Clayton R. N., and Mayeda T. K. 1996. Oxygen isotope studies of achondrites. *Geochimica et Cosmochimica Acta* 60:1999-2017.

Davidson P. M. and Mukhopadhyay D. K. 1984. Ca- Fe- Mg olivines: phase relations and a solution model. *Contribution to Mineralogy and Petrology* 86:256-263.

Deligny C., Füri E., and Deloule E. 2021. Origin and timing of volatile delivery (N, H) to the angrite parent body: Constraints from in situ analyses of melt inclusions. *Geochimica et Cosmochimica Acta 313*:243-256.

Faure F., Arndt N. T., and Libourel G. 2006. Formation of spinifex texture in komatiites: an experimental study. *Journal of Petrology* 47: 1591–1610.

Filiberto J., and Dasgupta R. 2011. Fe^{2+}-Mg partitioning between olivine and basaltic melts: Applications to genesis of olivine-phyric shergottites and conditions of melting in the Martian interior. *Earth and Planetary Science Letters* 304: 527-537.

Fritz J., Wünnemann K., Greshake A., and Fernandes V. A. 2011. Shock pressure calibration for lunar plagioclase (abstract #1196). 42nd Lunar and Planetary Science Conference.

Gellissen M., Palme H., Korotev R. L., and Irving A. J. 2007. NWA 2999: a unique angrite with a large chondritic component (abstract # 1612). 38th Lunar and Planetary Science Conference (CD-ROM).

Gilmour J. D., Crowther S. A., Busfield A., Hollan G., and Whitby J. A. 2009. An early I-Xe age for CB chondrite chondrule formation, and a re-evaluation of the closure age of Shallowater enstatite. *Meteoritics and Planetary Science* 44:573-579.

Goldreich P., and Ward W. R. 1973. The formation of planetesimals. *The Astrophysical Journal* 183: 1051-1061.

Goodrich C. A., Scott E. R. D., and Fioretti A. M. 2004. Ureilitic breccias: clues to the petrologic structure and impact disruption of the ureilite parent asteroid. *Chemie der Erde-Geochemistry* 64:283-327.

Greenwood R. C., Franchi I. A., Jambon A., and Buchanan P. C. 2005. Widespread magma oceans on asteroidal bodies in the early solar system. *Nature* 435:916-918.

Hayashi H., Takenouchi A., Mikouchi T., and Bizzarro M. 2018. Shock metamorphism of the Northwest Africa 7203 angrite (abstract #1932). 49th Lunar and Planetary Science Conference.

Hayashi H., Mikouchi T., Sano Y., and Bizzarro M. 2019. Pb-Pb dating of the NWA 7203 angrite and relationship to its shock metamorphism. Japan Geoscience Union Meeting 2019: PCG22-P10.

Hayashi H., Mikouchi T., Kim N. K., Park C., Sano Y., Takenouchi T., Yamaguchi A., Kagi H., and Bizzarro M. 2022. Unique igneous textures and shock metamorphism of the Northwest Africa 7203 angrite: Implications for crystallization processes and the evolutionary history of the angrite parent body. *Meoetritics and Planetary Science* 57:105-121.

Hill R. E. T., Barnes S. J., Gole M. J., and Dowling S. E. 1995. The volcanology of komatiites as deduced from field relationships in the Norseman-Wiluna greenstone belt, Western Australia. *Lithos* 34: 159-188.

Irving A. J., Carpenter P. K., Tepper J. H., Righter M., Lapen T. J., and Busemann H. Petrology and chemical composition of olivine-pyroxene-phyric quenched angrite Northwest Africa NWA 12774 (abstract #2399). 51st Lunar and Planetary Science Conference.

Jambon A., Barrat J. A., Boudouma O., Fonteilles M., Badia D., Göpel C., and Bohn M. 2005. Mineralogy and petrology of the angrite Northwest Africa 1296. *Meoetritics and Planetary Science* 40:361-375.

Jambon A., Omar B., Michel F., Guillou L. E., Badia D., and Barrat J. A. 2008. Petrology and mineralogy of the angrite Northwest Africa 1670. *Meteoritics and Planetary Science* 43:1783-1795.

Jurewicz A. J. G., Mittlefehldt D. W., and Jones J. H. 1993. Experimental partial melting of the Allende (CV) and Murchison (CM) chondrites and the origine of asteroidal basalts. *Geochimica et Cosmochimica Acta* 57:2123–2139.

Keil K., Stöffler D., Love S. G., and Scott E. R. D. 1997. Constraints on the role of impact heating and melting in asteroids. *Meteoritics and Planetary Science* 32: 349-363.

Keil K. 2012. Angrites, a small but diverse suite of ancient, silica-undersaturated volcanic-plutonic mafic meteorites, and the history of their parent asteroid. *Chemie der Erde-Geochemistry* 72:191-218.

Kleine T., Hans U., Irving A. J., and Bourdon B. 2012. Chronology of the angrite parent body and implications for core formation in protoplanets. *Geochimica et Cosmochimica Acta* 84:186-203.

Kim N. K., Kusakabe M., Park C., Lee J. I., Nagao K., Enokido Y., Yamashita S., and Park S. Y. 2019. An automated laser fluorination technique for high-precision analysis of three oxygen isotopes in silicates. *Rapid Communications in Mass Spectrometry* 33:641-649.

Kim N. K., Park C., and Kusakabe M. (2020) Two-point normalization for reducing inter-laboratory discrepancies in $\delta^{17}O$, $\delta^{18}O$, and $\Delta'^{17}O$ of reference silicates. *Journal of Analytical Science and Technology* 11:51.

Kruijer T. S., Touboul M., Fischer-Gödde M., Bermingham K. R., Walker R. J., and Kleine T. 2014. Protracted core formation and rapid accretion of protoplanets. *Science* 344: 1150-1154.

Kruijer T. S., Kleine T., and Borg L. E. 2020. The great isotopic dichotomy of the early Solar System. *Nature Astronomy* 4: 32-40.

Larsen K. K., Schiller M., and Bizzarro M. 2016. Accretion timescales and style of asteroidal differentiation in an ^{26}Al-poor protoplanetary disk. *Geochimica et Cosmochimica Acta 176*: 295-315.

Lange R. L. 1994. The effect of H_2O, CO_2 and F on the density and viscosity of silicate liquids. *In Mineralogical Society of America Reviews in Mineralogy* 30: 331-369.

Lodders K. 2003. Solar system abundances and condensation temperatures of the elements. *The Astrophysical Journal* 591:1220-1247.

Longhi J. 1999. Phase equilibrium constraints on angrite petrogenesis. *Geochimica et Cosmochimica Acta* 63:573–585.

Lowrey J. R., Ivanic T. J., Wyman D. A., and Roberts M. P. 2017. Platy pyroxene: New insights into spinifex texture. *Journal of Petrology* 58: 1671-1700.

Lunning N. G., Gardner-Vandy K. G., Sosa E. S., McCoy T. J., Bullock E. S., and Corrigan C. M. 2017. Partial melting of oxidized planetesimals: An experimental study to test the formation of

oligoclase-rich achondrites Graves Nunataks 06128 and 06129. *Geochimica et Cosmochimica Acta* 214:73-85.

Ma C. and Beckett J. R. 2017. A new type of Tissintite, $(Ca,Mg,Na,\square_{0.14})(Al,Fe,Mg)Si_2O_6$, in the Zagami Martian meteorite: A high-pressure clinopyroxene formed by shock (abstract #1639). 48th Lunar and Planetary Science Conference.

Masiero J. H., Mainzer A. K., Grav T., Bauer J. M., Cutri R. M., Nugent C., and Cabrera M. S. 2012. Preliminary analysis of *WISE*/NEOEISE 3-Band cryogenic and post-cryogenic observations of main belt asteroids. *The Astrophysical Journal Letters* 759:L8

McCoy T. J., Wilson L., Benedix G. K., Ketcham R. A. 2003. Vesicles in meteorites: the angle on angrites (abstract). *Meteoritics and Planetary Science* 38 (Supplement):A65.

McKay G., Crozaz G., Wagstaff I., Yang S. R., and Lundberg L. 1990. A petrographic, electron microprobe, study of mini-angrite Lewis Cliff 87051. 21st Lunar and Planetary Science Conference: 771-772.

McKay G., Miyamoto M., Mikouchi T., and Ogawa T. 1998. The cooling history of the LEW 86010 angrite as inferred from kirschsteinite lamellae in olivine. *Meteoritics and Planetary Science* 33: 977-983.

McKeegan K. D. and Davis A. M. 2003. Early Solar System Chronology. *Treatise on Geochemistry* 1:431-460.

Meteoritical Bulletin Database, https://www.lpi.usra.edu/meteor/metbull.php.

Michel P., Jutzi M., Richardson D. C., Goodrich A., Hartmann W. K., and O'Brien D. P. 2015. Selective sampling during catastrophic disruption: Mapping the location of reaccumulated fragments in the original parent body. *Planetary and Space Science* 107: 24-28.

Mikouchi T., McKay G., and Le L. 1994. Cr, Mn and Ca distributions for olivine in angritic systems: Constraints on the origins of Cr-rich and Ca-poor core olivine in angrite LEW87051. 25th Lunar and Planetary Science Conference: 907-908.

Mikouchi T., and Miyamoto M. 1995. Porphyritic olivine in angrite LEW87051: Cooling rate and evidence for complex crystallization history from relict cores and zoning profiles. 26th Lunar and Planetary Science Conference: 973-974.

Mikouchi T., Miyamoto M. and McKay G. 1996. Mineralogical study of angrite Asuka-881371: Its possible relation to angrite LEW 87051. *Proceedings of NIPR Symposium on Antarctic Meteorites* 9:174-188.

Mikouchi M., McKay G., and Le L. 2000a. A new angrite Sahara 99555: Mineralogical comparison with Angra dos Reis, Lewis Cliff 86010, Lewis Cliff 87051, and Asuka-881371 angrites. *Antarctic meteorites* 25: 74-76.

Mikouchi T., McKay G., and Le L. 2000b. Experimental crystallization of the Asuka-881371 (angrite) groundmass composition: Implication for crystallization histories of Sahara 99555. *Meteoritics & Planetary Science* 35 (Supplement):A110-A111.

Mikouchi T., McKay G., Le L., and Mittlefehldt D. W. 2000c. Preliminary examination of Sahara 99555: Mineralogy and experimental study of a new angrite (abstract #1970). 31st Lunar and Planetary Science Conference (CD-ROM).

Mikouchi T., and McKay G. 2001. Mineralogical investigation of D'Orbigny: a new angrite showing close affinities to Asuka 881371, Sahara 99555, and Lewis Cliff 87051. (abstract #1876) 32nd Lunar and Planetary Science Conference (CD-ROM).

Mikouchi T., McKay G., Koizumi E., Monkawa A., and Miyamoto M. 2003. Northwest Africa 1670: A new quenched angrite. *Meteoritics & Planetary Science* 38 (supplement): A115.

Mikouchi T., McKay G., and Jones J. H. 2004. Sahara 99555 and D'Orbigny: Possible pristine parent magma of quenched angrites (abstract #1504) 35th Lunar and Planetary Science Conference (CD-ROM).

Mikouchi T., McKay G., and Jones J. 2008. Petrogenesis and crystallization history of quenched angrites. *Meteoritics & Planetary Science* 43 (Supplement):A98.

Mikouchi T. and Bizzarro M. 2012. Mineralogy and Petrology of NWA 7203: A new quenched angrite Similar to NWA 1296 and NWA 1670. *Meteoritics & Planetary Science* 47 (Supplement):5120.

Mikouchi T. and Zolensky M. E. 2021. Mineralogy and cooling history of ungrouped achondrite Erg Check 002 (abstract #2548) 52nd Lunar and Planetary Science Conference.

Misener D. J. 1974. Cationic diffusion in olivine to 1400 ºC and 35 kbar. *Geochemical Transport and Kinetics* 634:117-129.

Mittlefehldt D. W., and Lindstrom M. M. 1990. Geochemistry and genesis of the angrites. *Geochimica et Cosmochimica Acta* 54:3209-3218.

Mittlefehldt D. W., McCoy T. J., Goodrich C. A., and Kracher A. 1998. Non-chondritic meteorites from asteroidal bodies. *Planetary Materials Revies in Mineralogy* 36: 1-195.

Mittlefehldt D. W., Killgore M., and Lee M. T. 2002. Petrology and geochemistry of D'Orbigny, geochemistry of Sahara 99555, and the origin of angrites. *Meteoritics & Planetary Science* 37:345-369.

Miyamoto M., Mikouchi T., and Arai T. 2002. Comparison of Fe-Mg interdiffusion coefficients in olivine. *Antarctic Meteorite Research 15*:143-151.

Nemchin A., Timms N., Pidgeon R., Geisler T., Reddy S. and Meyer C. 2009. Timing of crystallization of the lunar magma ocean constrained by the oldest zircon. *Nature Geoscience* 2: 133-136.

Nittler L. R., McCoy T. J., Clark P. E., Murphy M. E. Trombka J. I., and Jaroseewich E. 2004. Bulk element compositions of meteorites: A guide for interpreting remote-sensing geochemical measurements of planets and asteroids. *Antarctic Meteorite Research 17*:231-251.

O'Neill B. H. S., and Palme H. 2008. Collisional erosion and the non-chondritic composition of the terrestrial planets. *Philosophical Transactions of The Royal Society A* 366: 4205-4238.

Palme H., and Jones A. 2003. Solar system abundances of the elements. Treatise on geochemistry 003: 41-61.

Petit J. M., and Morbidelli A. 2001. The Primordial Excitation and Clearing of the Asteroid Belt. *Icarus* 153: 338-347.

Pyke D. R., Naldrett A. J., Eckstrand O. R. 1973. Archean ultramafic flows in Munro Township, Ontario. *Bulletin of the Geological Society of America* 84: 955-978.

Renner R., Nisbet E. G., Cheadle M. J., Arndt N. T., Bickle M. J., and Cameron W. E. 1994. Komatiite flows from the Reliance Formation, Belingwe Belt, Zimbabwe: I. Petrography and mineralogy. *Journal of Petrology* 35: 361-400.

Riches A. J. V., Day J. M. D., Walker R. J., Simonetti A., Liu Y., Neal C. R., and Taylor L. A. 2012. Rhenium-osmium isotope and highly-siderophile-element abundance systematics of angrite meteorites. *Earth and Planetary Science Letters* 353-354: 208-218.

Roeder P. L. and Emslie R. F. 1970. Olivine-liquid equilibrium. *Contribution to Mineralogy and Petrology* 29:275-289.

Russell C. T., Raymond C. A., Coradini A., McSween H. Y., Zuber M. T., Nathues A., De Sanctis M. C., Jaumann R., Konopliv A. S., Preusker F., Asmar S. W., Park R. S., Gaskell R., Keller H. U., Mottola S., Roatsch T., Scully J. E. C., Smith D. E., Tricarico P., Toplis M. J., Christensen U. R., Feldman W. C., Lawrence D. J., McCoy T. J., Prettyman T. H., Reedy R. C., Sykes M. E., and Titus T. N. 2012. Dawn at Vesta: Testing the protoplanetary paradigm. *Science* 336: 684-686.

Sanborn M. E., and Wadhwa M. 2010. Rare earth element geochemistry of quenched angrites Northwest Africa 1296 and Northwest Africa 1670 (abstract #1490). 41st Lunar and Planetary Science Conference.

Sanborn M. E., and Wadhwa M. 2021. Trace element geochemistry of coarse-grained angrites from Northwest Africa: Implications for their petrogenesis on the angrite parent body. *Meteoritics and Planetary Science* 56:482-499.

Santos A. R., Agee C. B., Shearer C. K., Bell A. S., and McCubbin F. M. 2016a. Northwest Africa 8535 and Northwest Africa 10463: New insights into the angrite parent body (abstract #2590). 47th Lunar and Planetary Science Conference.

Santos A. R., Agee C. B., Shearer C. K., Bell A. S., Burger P. V., and McCubbin F. M. 2016b. *Dunitic angrite Northwest Africa 8535: Description and initial interpretations.* NM, USA. UNM Digital Repository.

Satake W., Mikouchi T., and Miyamoto M. 2014. Redox states of thirteen shergottites as inferred from iron micro X-ray absorption near edge structure of maskelynite. *Geochemical Journal* 48, 85-98.

Scott E. R. D. and Bottke W. F. 2011. Impact histories of angrites, eucrites, and their parent bodies. *Meteoritics & Planetary Science* 46:1878-87.

Schiller M., Connelly J. N., Glad A. C., Mikouchi T., and Bizzarro M. 2015. Early accretion of protoplanets inferred from a reduced inner solar system ^{26}Al inventory. *Earth and Planetary Science Letters* 420: 45-54.

Seidelmann P. K., Archinal B. A., A'hearn M. F., Conrad A., Consolmagno G. J., Hestroffer D., Hilton J. L., Krasinsky G. A., Neumann G., Oberst J., Stooke P., Tedesco E. F., Tholen D. J., Thomas P. C., and Williams I. P. 2007. Report of the IAU/IAG Working Group on cartographic

coordinates and rotational elements: 2006. *Celestial Mechanics and Dynamical Astronomy* 98: 155-180.

Shaw H. R. 1972. Viscosities of magmatic silicate liquids; an empirical method of prediction. *American Journal of Science* 272: 870-893.

Shirai N., Humayun M., and Irving A. J. 2009. The bulk composition of coarse-grained meteorites from laser ablation analysis of their fusion crusts (abstract #2170). 40th Lunar and Planetary Science Conference (CD-ROM).

Srinivasan G., Whitehouse M. J., Weber I., and Yamaguchi A. 2007. The crystallization age of eucrite zircon. *Science* 317: 345-347.

Stöffler D., Ostertag R., Jammes C., Pfannschmidt G., Sen Gupta P. R., Simon S. B., Papike J. J., and Beauchamp R.H. 1986. Shock metamorphism and petrography of the Shergotty achondrite. *Geochimica et Cosmochimica Acta* 50:889-903.

Suzuki H., Ozawa K., Nagahara H., and Mikouchi T. 2014. Estimate of radius size of the angrite parent body (in Japanese). 2014 Annual meeting of Japan Geoscience Union. PPS22-04.

Takenouchi A., Sumino H., Hayashi H., Mikouchi T., and Bizzarro M. 2019. Noble gas analyses of uniquely shocked angrite Northwest Africa 7203 (LPI Contrib. No. 2132). 50th Lunar and Planetary Science Conference.

Tissot F. L. H. and Dauphas N. 2012. $^{238}U/^{235}U$ ratios of anagrams: Angrites and granites (abstract #1981). 43rd Lunar and Planetary Science Conference.

Tissot F. L. H., Dauphas N., and Grove T. L. 2017. Distinct $^{238}U/^{235}U$ ratios and REE patterns in plutonic and volcanic angrites: Geochronologic implications and evidence for U isotope fractionation during magmatic processes. *Geochimica et Cosmochimica Acta* 213:593-617.

Torigoye-Kita N., Tatsumoto M., Meeker G. P., and Yanai K. 1995. The 4.56 Ga U-Pb age of the MET 780058 ureilite. *Geochimica et Cosmochimica Acta* 59:2319-2329.

Walsh K. J., Morbidelli A., Raymond S. N., O'Brien D. P., and Mandell A. M. 2011. A low mass for Mars from Jupiters early gas-driven migration. *Nature* 475: 206-209.

Warren P. H. 2011. Stable-isotopic anomalies and the accretionary assemblage of the Earth and Mars: a subordinate role for carbonaceous chondrites. *Earth and Planetary Science Letters* 311: 93-100.

Warren P. H. 2012. Parent body depth–pressure–temperature relationships and the style of the ureilite anatexis. *Meteoritics & Planetary Science* 47:209-227.

Weiss B. P., Berdahl J. S., Ekins-Tanton L., Stanley S., Lima E. A., and Carporzen L. 2008. Magnetism on the angrite parent body and the early differentiation of planetesimals. *Science* 31:713-16.

Wetherill G. W., and Williams J. G. 1979. Origin of differentiated meteorites. *Physics and Chemistry of the Earth* 11: 19-31.

Wilke M., Farges F., Petit P. E., Brown Jr. G. E., and Martin F. 2001. Oxidation state and coordination of Fe in minerals: An Fe K-XANES spectroscopic study. *American Mineralogist* 86: 714-730.

Williams D. A., Kerr R. C., Lesher C. M., and Barnes S. J. 2002. Analytical/numerical modeling of komatiite lava emplacement and thermal erosion at Perseverance, Western Australia. *Journal of Volcanology and Geothermal Research* 110: 27–55.

Wilson L., and Keil K. 1991. Consequences of explosive eruptions on small Solar System bodies: the case of the missing basalts on the aubrite parent body. *Earth and Planetary Science Letters* 104: 505-512.

Yanai K. 1994. Angrite Asuka-881371: Preliminary examination of a unique meteorite in the Japanese collection of Antarctic meteorites. *Proceedings of NIPR Symposium on Antarctic Meteorites* 7:30-41.

Yin Q. Z., McCubbin F M., Zhou Q., Santos A. R., Targese R., Li X., Li Q. L., Tang G., Boyce L., Yang W., Zhang J., Hao J., Elardo S. M., Shearer C. K., Rowland D. J., Lerche M., and Agee C. 2014. An Earth-like beginning for ancient Mars indicated by alkali-rich volcanism at 4.4 Ga (abstract #1320). 45th Lunar and Planetary Science Conference (CD-ROM).

Zartman R. E., Jagoutz E. and Bowring S. A. 2006. Pb-Pb dating of the D'Orbigny and Asuka 881371 angrites and a second absolute time calibration of the Mn-Cr chronometer (abstract #1580). 37th Lunar and Planetary Science Conference (CD-ROM).

Zuber M. T., McSween H. Y., Binzel R. P., Elkins-Tanton L. T., Konopliv A. S., Pieters C. M., and Smith D. E. 2011. *Space Science Reviews* 163: 77-93.